COMPARISON OF SLIDING-MODE CONTROL AND MODEL-PREDICTIVE CONTROL ALGORITHMS FOR PNEUMATIC ACTUATORS

COMPARISON OF SLIDING-MODE CONTROL AND MODEL-PREDICTIVE CONTROL ALGORITHMS FOR PNEUMATIC ACTUATORS

BY

YILE ZHANG, B. A.

A Thesis

Submitted to the School of Graduate Studies

in Partial Fulfilment of the Requirements

for the Degree

Master of Applied Science

McMaster University

MASTER OF APPLIED SCIENCE (2015)	McMaster University
(Mechanical Engineering)	Hamilton, Ontario, Canada

TITLE: Comparison of Sliding-Mode Control and Model-Predictive Control Algorithms for Pneumatic Actuators

AUTHOR: Yile Zhang

B.ENG., (AUTOMATION)

Beihang University, Beijing, China

SUPERVISOR: Dr. Gary M. Bone, Professor

NUMBER OF PAGES: xxiv, 141

LAY ABSTRACT

Actuators produce forces and motions in machines. Pneumatic actuators are low-cost, clean, safe and provide a high power to weight ratio. In this thesis, the modeling and position control of pneumatic actuators is presented. The actuator's main components consist of a pneumatic cylinder and four electronic valves. The dynamics of the actuator components are mathematically modelled. A novel friction model is presented. Each valve is switched either on (to allow airflow) or off (to prevent airflow) every few milliseconds using a computer-based control system. Three novel nonlinear control algorithms are designed and compared with two existing state-of-the-art algorithms. Simulation and experiments demonstrate that the three proposed control algorithms reduced the position tracking errors and valve switching frequency (leading to longer valve life) when applied to a pneumatic cylinder with high friction seals. The designed controllers are also simulated and compared on a lower friction cylinder to demonstrate their generality.

ABSTRACT

Pneumatic actuators are low-cost, clean, safe and provide a high power to weight ratio. In this thesis, the modeling and position control of pneumatic actuators is presented. Sliding-mode control and model-predictive control algorithms are compared.

The actuator's main components consist of a double acting pneumatic cylinder and four two-way on/off valves. A nonlinear system model was developed. Its parameters were estimated from experiments. A novel friction model was presented and shown to be superior to the classical friction model. The system model was validated by comparing simulation and experiment results.

Three novel nonlinear control algorithms are designed and compared with two existing state-of-the-art sliding-mode control (SMC) algorithms. Two of the novel algorithms are modified versions of the existing SMC algorithms. The third is a discrete-valued model predictive control (DVMPC) algorithm. The designs and performance of the five control algorithms were compared.

Simulations and experiments demonstrated that the two modified SMC algorithms reduced both the position tracking errors and the valve switching frequency. Reducing a valve's switching frequency has the benefit of prolonging its life. In the experiments on a cylinder with high friction seals, the steady state errors reduced 42% to ±0.3 mm. The valve switching frequency was also reduced by 34%. The switching frequency was further reduced by 32%, without significantly affecting the tracking performance, by incorporating a 5 ms zero-order hold. The five algorithms were simulated and compared on a high friction cylinder and a low friction cylinder to demonstrate their generality. In the simulations, the position tracking performance with DVMPC was similar to the best SMC algorithm, and the valve switching frequency with DVMPC was 34% lower. The three novel controllers were shown to be robust to increased and decreased payload mass. The DVMPC calculation times demonstrated that future experimental implementation of DVMPC is possible.

ACKNOWLEDGEMENTS

I would like to express my sincere gratitude to my research supervisor, Dr. Gary M. Bone, for his valuable guidance and support. He has walked me through all of the stages of this research. Without him, this thesis could never have been finished.

I would also like to thank the technicians: Mr. Michael Lee, Mr. Ron Lodewyks, Mr. John Colenbrander and Mr. Mark Mackenzie for their support and suggestions with the test setup. I also thank my colleagues: Graham Ashby and Yifei Feng for their advice and encouragement. And I like to express my thanks to all my friends for their support and encouragement.

Finally I would like to specially show appreciation to my family for their encouragement and support.

TABLE OF CONTENTS

LIST OF TABLES

LIST OF FIGURES

NOMENCLATURE

A_a , A_b	Cross-sectional areas of Chambers A and B
$c_{choked,fill}$	Filling choked mass flow rate coefficient
c_{fill} , c_{dis}	Chamber filling and discharging coefficient
c_p	Specific heat for a constant pressure
c_v	Specific heat for a constant volume
$C_{v,p}$, $C_{v,n}$	Viscous friction coefficients for positive and negative directions
$\frac{dQ}{dt}$	Rate of heat transfer
e , $\dot{e}$, $\ddot{e}$	Position, velocity and acceleration error
e_{limit}	Threshold used to limit the integral action
$F_{c,p}$, $F_{c,n}$	Coulomb friction forces for the positive and negative directions
F_f	Friction force
$F_{s,p}$, $F_{s,n}$	Static friction forces for the positive and negative directions
$F_{s0,p}$, $F_{s0,n}$	Static friction force when $\Delta P = 0$ for the positive and negative directions
F_p	Applied pneumatic force
$\hat{F}_p$	Predicted pneumatic force
J	Cost function
K	Gas heat ratio
L	Stroke length

M	Mass of the payload
$\dot{m}_1, \dot{m}_2, \dot{m}_3, \dot{m}_4$	Mass flow rates through the Valves 1-4
$\dot{m}_a, \ \dot{m}_b$	Mass flow rates into Chambers A and B
N_p	Prediction horizon used in DVMPC
ΔP	Pressure difference between the cylinder chambers
P_0	Atmospheric pressure
P_a, P_b	Pressure in Chamber A
P_s	Supply pressure
R	Gas constant
$s_1, \ s_2, \ s_3, \ s_4$	Internal states of the four valves
T	System temperature
T_s	Sampling period
$u_1, \ u_2, \ u_3, \ u_4$	Valves 1-4 control inputs
$\hat{u}_1, \ \hat{u}_2, \ \hat{u}_3, \ \hat{u}_4$	Predicted valves 1-4 control signals
$\mathbf{U}_{opt}$	Optimized control sequence in DVMPC
V_a, V_b	Volumes of Chambers A and B
$V_{a0}, \ V_{b0}$	Dead volumes of Chambers A and B
V	Lyapunov-like function used in DVMPC
$V_{threshold}$	Threshold of Lyapunov-like function for DVMPC stability
$v_{s,n}, v_{s,p}$	Stribeck velocity for the negative and positive directions
$w_v, w_{du}, w_p, \ w_{ps}$	Cost function weighting coefficients used in DVMPC

y_{a0}	Minimum payload displacement
y_{b0}	Maximum payload displacement
y , $\dot{y}$, $\ddot{y}$	Position, velocity and acceleration of payload
$\hat{y}$, $\hat{\dot{y}}$, $\hat{\ddot{y}}$	Predicted position, velocity and acceleration
$\alpha_{p,p}$, $\alpha_{p,n}$	Static friction parameters for the positive and negative directions
$\beta_{p,p}$, $\beta_{p,n}$	Dynamic friction parameters for positive and negative directions
β , ε	Deadbands used in sliding-mode control
ζ , ω	Sliding-mode controller parameters
ζ_{choked}	Value used to determine when the mass flow is choked
$\tau_{d,open}$	Valve energizing delay time
$\tau_{d,close}$	Valve de-energizing delay time

ABBREVIATIONS

ARX	Auto regressive with external input
BEE	Bounded-error estimation
BIBO	Bounded-input, bounded-output
DVMPC	Discrete-valued model predictive control
HFC	High friction cylinder
LFC	Low friction cylinder
LVQNN	Learning vector quantization neural network
MPC	Model predictive control
MPWM	Modified pulse-width modulation
MSMCL	Model-based SMC law
NMPC	Nonlinear model predictive controllers
NOMAD	Nonlinear optimization by mesh adaptive direct search
OS	Overshoot
PID	Proportional plus integral plus derivative
PRBS	Pseudo random binary signal

PVA	Proportional plus velocity plus acceleration
PWM	Pulse width modulation
RMSE	Root Mean Square Error
SMC	Sliding mode controller
SMC3	Three-mode sliding mode controller
SMC7	Seven-mode sliding mode controller
SMCI3	Three-mode sliding mode control with integral action law
SMCI7	Seven-mode sliding mode control with integral action law
SPS	Switches per second
SSE	Steady state error
ZOH	Zero-order hold

CHAPTER 1 INTRODUCTION

1.1 Motivation of the research

A pneumatic actuator refers to a mechanical device that converts air pressure to physical motion. Pneumatic actuators are widely used in industrial automation due to their inherent advantages. They are low cost, clean and provide a high power to weight ratio. They are also inherently safe due to their natural compliance.

Due to the unique advantages above, more sophisticated applications of pneumatic actuators have been attracting the attentions of researchers. Their closed-loop position control remains an active field. The biggest challenge of achieving the fast and accurate position control of a pneumatic actuator is dealing with its nonlinearity. A pneumatic actuator is highly nonlinear due to the compressibility of the air, the nonlinearity of the mass flow rate and the variation of the friction.

The pneumatic position control system usually includes a double acting pneumatic cylinder; one or more control valves; sensors; and the controller hardware and software algorithms. There are two main classes of control valves. Valves that can only be either open or closed are known as on/off valves. They are typically activated using solenoids. The other class are proportional/servo valves, whose orifice area is continuously adjustable. Proportional/servo valves are much larger and more expensive than on/off valves, so on/off valves have more potential applications in robotics and automation. That is why the research presented in this thesis focuses on on/off valves.

Research on on/off (solenoid) valve controlled pneumatic actuators has been ongoing for more than 30 years. The discontinuity of on/off valves makes it more difficult to produce fast and accurate position control with them than with proportional valves. In the previous studies using on/off valves, some researchers applied pulse-width modulation (PWM) technology to approximate a proportional valve. Controllers based on driving the valves with PWM may give acceptable performance, but the valves are switched frequently which may greatly reduce the valves' lifespan. The rapid development of high-speed computers has made it possible to implement more sophisticated control algorithms, such as backstepping control and sliding model control.

1.2 Objective and organization of the thesis

The objective of this thesis is to study advanced control algorithms for pneumatic actuators using on/off solenoid valves. The system model is derived in detail, including the models of friction and the valves. Sliding mode controllers and model predictive controller will be designed and compared on a high friction cylinder and a low friction cylinder. The robustness of the controllers is also tested.

The organization of the thesis is as follows. In chapter 2, the literature related to the modeling of pneumatic systems and control algorithms for their position control is reviewed. The system architecture and modeling of the high friction cylinder are described in chapter 3. The system model includes the system dynamics model, friction model and mass flow rate model. The system model is validated by experiments. In chapter 4, five controllers are designed. Two are applications of existing control algorithms to our system. The remaining three are novel contributions. Two types of sliding mode controller with integral action and a discrete-valued model predictive controller are proposed. In chapter 5, the proposed controllers are simulated and compared with previous sliding mode controllers using both the high friction cylinder and a low friction cylinder. The robustness of the controllers to payload mismatch is also tested. Experimental results are reported and discussed in chapter 6. Conclusions are drawn in chapter 7. The achievements and limitations of this research are summarized. Finally, recommendations for future works are presented.

CHAPTER 2 LITERAURE REVIEW

2.1 Introduction

Due to the advantages of pneumatic actuators, researchers have been studying their closed-loop position control for more than 50 years. In this chapter, the state of the art in the following areas will be reviewed: modeling of pneumatic systems, and control algorithms for their position control and motion tracking.

2.2 System modeling

The three common configurations for position controlled pneumatic actuators are shown in Figure 2.1. All use a double acting pneumatic cylinder, typically with a single rod. The most common configuration shown in Figure 2.2.1(a) uses two three-way on/off valves. Replacing those two valves with four two-way on/off valves offers the potential for higher performance while moderately increasing cost (see Figure 2.2.1(b). The third configuration uses a four-way or five-way proportional/servo valve, shown in Figure 2.2.1(c). Since proportional/servo valves are much more expensive than on/off this configuration is the most costly. It is also the easiest to control. In this thesis, the pneumatic system will consist of a double acting pneumatic cylinder, four two-way on/off valves, a sensor to measure the piston's position and three sensors to measure the supply pressure and the pressures of the two chambers of the cylinder. Various approaches have been used to model the dynamic behaviour of these types of pneumatic systems.

Only a few publications model the entire system as a black box and use system identification methods to obtain a process model. For example, van Varseveld and Bone

(1997) used system identification to obtain a linear model of a pneumatic cylinder driven by two three-way on/off valves. A novel valve pulse width modulation (PWM) scheme acted to linearize the system dynamics, justifying the use of a linear model. Specifically, an auto regressive with external input (ARX) model was used with six parameters. The data was obtained by open-loop tests with a pseudo random binary signal (PRBS) input at different piston positions. Model validation results were not presented.

The more common approach is to treat the system as interconnected components and then to model each of them separately. The components are the mass flow rate characteristics of the control valves, the dynamic behaviour of the air in the cylinder chamber, and the relationship between pressure difference and piston movement. The piston and/or the payload it drives may be subject to large friction forces. Valve modeling and friction modeling are the most difficult aspects of this modelling approach. Some researchers also identify a leakage model including the leakage between chambers and the leakage across the rod seal, since the effects of leakage are significant in their cylinders.

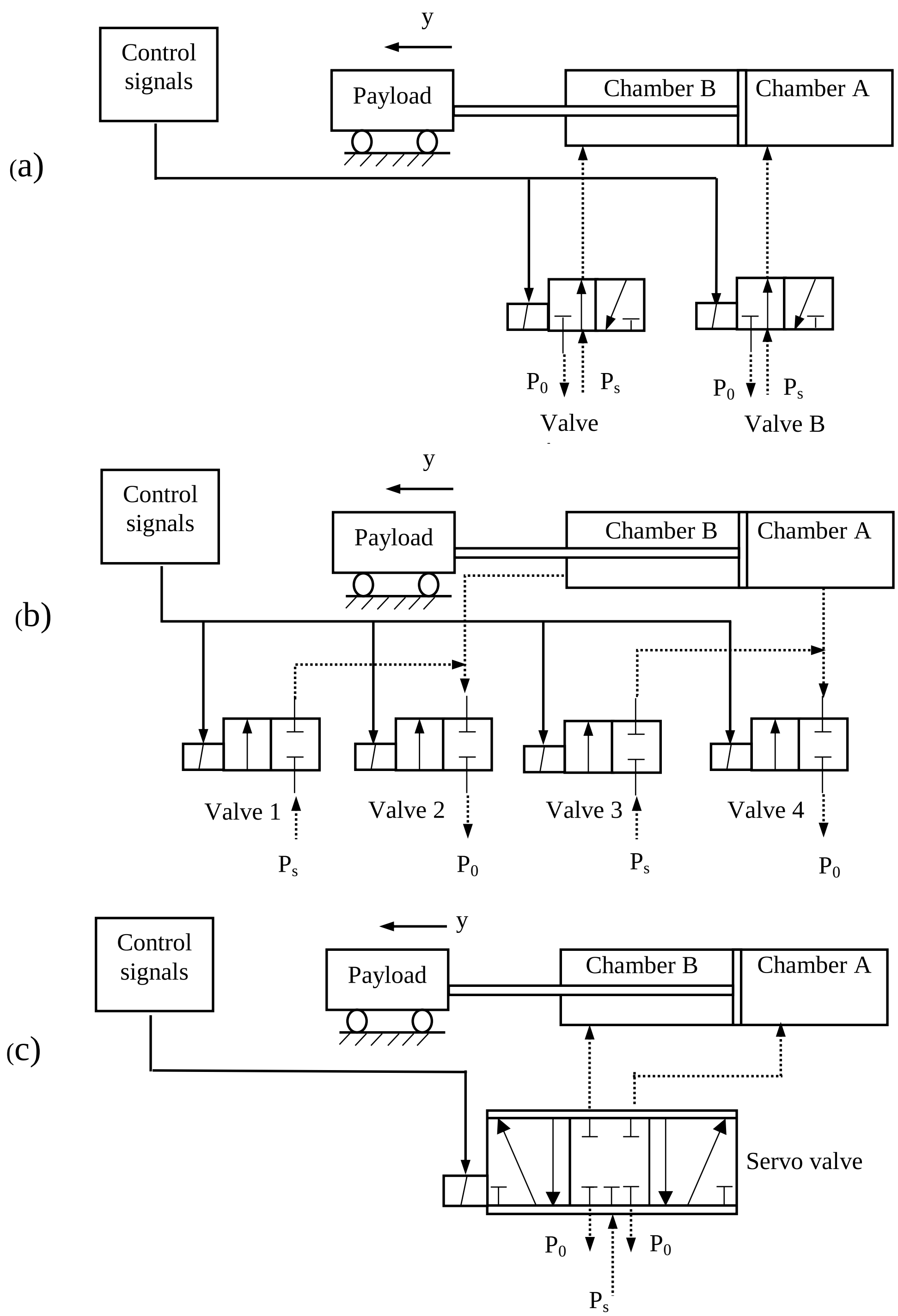

Figure 2.2.1 (a) Configuration using two three-way on/off valves. (b) Configuration using four two-way on/off valves. (c) Configuration using one five-way proportional/servo valve.

Shearer (1956) presented a fundamental analysis of the dynamics of pneumatic systems for control purposes. This was the first published scientific analysis of pneumatic systems and most of the subsequent works on pneumatic system modeling are based on his work. The system includes a four-way control valve and a double acting cylinder. The relationship between mass flow rate and pressure was derived by analyzing the dynamic behaviour of the fluid in the chambers based on the ideal-gas equation, mass continuity equation and energy conservation equation. The relationship between control signal and mass flow rate was derived by applying the spray nozzle formula to the orifice of the valve. The equation of chamber pressure difference and piston motion was obtained by using Newton's 2^{nd} law of motion. Finally, the highly nonlinear system equation was simplified to a linear 3^{rd} order system model.

Ye, Scavarda, Betemps, and Jutard (1992) presented two models of a PWM solenoid valve. The first one shows the nonlinearity and discontinuity of mass flow rate, but involves relatively complex calculations. Next they investigated static characteristics of the PWM solenoid valve, developed a model of the average mass flow. This second model involves simpler calculations and is better suited for use in control algorithms.

Wang, Mo, and Chen (1998) presented a simple model of the switching characteristics for on/off valves. Their model is similar to the model of Ye et al. (1992). They used a multi-variate least squares estimation method to obtain the nine unknown parameters that minimized the squared pressure error between model simulation results and experimental results.

Although they did not model an on/off valve, the work of Bobrow and McDonell (1998) is relevant since they proposed an empirical mass flow rate model that is distinct from the mass flow rate model used by Shearer (1956); Ye, Scavarda, Betemps, and Jutard (1992); Wang, Mo, and Chen (1998); and many other researchers. They measured the internal energy of the mass flowing into the system rather than mass flow rate for the purposes of developing their control law. Least squares surface fitting was used with two surfaces—one that represents cylinder filling from the supply and the other that represents cylinder exhausting to atmosphere. The internal energy model for filling was a function of square root of difference between supply pressure and chamber pressure and for exhausting it was a function of difference of chamber pressure and atmosphere pressure. The curve fitting with their new functions was shown to be much more accurate than the previous flow rate model.

Messina, Giannoccaro, and Gentile (2005) proposed a mathematical model describing the dynamics of pneumatic systems controlled by two three-way on/off valves using PWM. In the experimental set-up, they added a laser sensor to measure the displacement of the valve's spool versus time and evaluate the kinematics of the opening and closing of the valve. They identified 46 model parameters using measurements and curve fitting. They validated their model using experiments at two different initial conditions with five different duty cycles. The simulation vs. experimental comparisons showed that the mean error of the predicted actuator position was less than 2 mm for all ten experiments. However, their model may be too complex to be used in a practical control system.

Shen, Zhang, Barth, and Goldfarb (2006) proposed a model of a pneumatic system similar to the one studied by Messina, Giannoccaro, and Gentile (2005). Rather than model the discontinuous flow rate caused by the PWM, they derived a continuous nonlinear averaged model. Their model was also affine in terms of a continuous control input making it well suited for use in a position control system. They did not present a parameter identification method or validate the model.

Corteville, Van Brussel, Al-Bender, and Nuttin (2005) developed a new model for a pneumatic actuator controlled using a five-way proportional valve. They modeled both filling process and exhausting process using complex nonlinear function rather than using the formula describing an ideal nozzle. Sixteen parameters must be identified for each of the filling and exhausting processes. Their disadvantage of their approach is that reliably identifying a large set of unknown parameters is very difficult.

Rao and Bone (2008) proposed a new empirical model for two-way proportional valves. They modelled the mass flow rate as a 2nd order bipolynomial function of the input voltage and downstream pressure. The fitting results showed that their model produced 43% smaller fitting errors than the model of Bobrow and McDonell (1998).

Carneiro and Almeida (2006) derived a more accurate thermodynamic model defining the evolution of temperature and pressure inside a pneumatic cylinder chamber from thermodynamic first principles. Due to the difficulty of using the full model, they also presented several reduced-order thermodynamic models. Based on this thermodynamic model, Carneiro and Almeida (2012) presented a complete system model of single rod pneumatic cylinder driven by two three-way proportional valves. They used artificial neural networks to model the cylinder friction force and valve mass flow rates. Experimental results demonstrated that their model can predict the friction with an error less than %14 and the piston position with an error less than %8.

Hodgson, Tavakoli, Pham, and Leleve (2015) presented an averaged continuous-input model of a system consisting of four PWM controlled two-way solenoid valves and a pneumatic cylinder. They extended the nonlinear averaging model for three operating modes presented by Shen et al. (2006) to a seven-mode pneumatic system.

There is very little existing literature on the modeling of leakage for pneumatic actuators. Richard and Scavarda (1996) considered a leakage mass flow across the piston seal. They modelled it as a function of the ratio of two chamber pressures. They did not consider the leakage across the rod seal. Geleževičius and Grigaitis (2006) also considered the leakage between the cylinder chambers. They modelled it as a function of the difference of the chamber pressures.

Friction is a complex phenomenon in most mechanical systems. A detailed analysis and description of friction models can be found in the survey paper Armstrong-Hélouvry, Dupont, and De Wit (1994). In pneumatic systems, the friction force mainly comes from the contact between the piston seals and the cylinder wall. The other sources are the rod and its seal; the linear slide supporting the payload mass; and the position feedback device. Researchers continue searching for friction models that are accurate while still being suitable for practical implementation.

Most friction models for pneumatic actuators include static, Coulomb and viscous components (Shearer (1956), Ning and Bone (2005), Rao and Bone (2008)). Wang, Wang, Moore and Pu (2001) measured friction forces on different positions along the cylinder. Their experimental results demonstrated that the static friction force distribution depended on piston position and the direction of its movement. This makes friction modeling of pneumatic actuator very difficult. Rao and Bone (2008) used a classical friction model that consists of static friction, Coulomb friction, viscous friction and the Stribeck effect. The Stribeck effect causes the friction force to reach a minimum at a low velocity, before it becomes dominated by the viscous component.

De Wit, Olsson, Astrom, and Lischinsky (1995) proposed a novel friction model suitable for use in control systems, known as the LuGre model. This model incorporates Stribeck effect, stick - slip motion, Coulomb and viscous friction. The LuGre model addresses more phenomena than previously developed models. On the other hand, the LuGre model is difficult to identify due to it having more unknown parameters. Madi, Khayati and Bigras (2004) identified LuGre model parameters using a bounded-error estimation (BEE) approach based on interval analysis and set inversion. Compared with the classical least square approach, the BEE method allows the modeling errors and uncertainties to be considered. This parameter estimation approach was performed and validated on a rodless pneumatic cylinder. Mehmood, Laghrouche, and El Bagdouri (2011) compared the suitability of the LuGre and Dahl (1968) friction models for a spring-return pneumatic actuator. They found that two the models predicted the experimental results with similar accuracy. Probably due to its difficulty and lack of obvious benefit, most papers on pneumatic actuators do not use the LuGre model.

Ballard (1974) included the pressure difference between the cylinder chambers in his modelling of the friction forces of pneumatic systems. With the same piston velocity, he observed that the friction force is larger with a larger pressure difference. Schoroeder and Singh (1993) gave a list of friction models that include the pressure difference between the chambers and their coefficients of determination as a measure of the modelling accuracy. The accuracy was higher for the models that included the pressure difference.

2.3 Position control

Since on/off valves are used in the thesis, this section focuses on position control of pneumatic actuators using on/off solenoid valves.

One of the first studies on the position control of pneumatic actuators using on/off valves was conducted by Paul, Mishra, and Radke (1994). Their pneumatic system included a double acting cylinder and four two-way on/off solenoid valves. To avoid measuring the piston acceleration and chamber pressures, a reduced order sliding mode control (SMC) algorithm was designed. A first-order sliding surface requiring only position and velocity signals was used. Only a potentiometer was used for the feedback device and no pressure sensors were employed. Experimental results show that the position error is about 5 mm and the settling time for a 120 mm step is about 2 s. No payload mass was used. No robustness tests were done in the paper.

The discontinuity of on/off valves makes it more difficult to produce fast and accurate position control than with proportional valves. Most of early papers on position control using on/off valves are based on pulse-width modulation (PWM) method to approximate a proportional valve.

van Varseveld and Bone (1997) presented a fast and accurate PWM-based position controller based on proportional plus integral plus derivative (PID) control. The system included two three-way on/off valves and a single rod cylinder. A novel PWM valve pulsing scheme was presented to completely remove the dead-band. Friction compensation was added to the PID controller to reduce the steady-state error (SSE) by 40% from 0.19 mm to 0.11mm. Step tests show that the rise time for a 62 mm step was approximately 180 ms, which was much faster compared to previous works (800 ms in Linnett and Smith (1989) and 350 ms in Noritsugu (1987)). The controller's robustness was shown by the closed-loop system maintaining stability for payload masses ranging from 0.94 kg to 5.63 kg. Aziz and Bone (2000) continued this work and developed a novel automatic tuning methodology for this enhanced version of PID control. The user inputs were the desired rise time and percent overshoot specifications. All controller parameters were auto-tuned by combining off-line model-based analysis with on-line iterative techniques. The tuning order was PD gains, integral gain, friction compensation, and the velocity and acceleration feedforward gains. The auto-tuner was tested with the following three actuators with distinct open-loop dynamics: (A) 27 mm diameter bore, 75 mm stroke, 0.3 kg inertia, (B) 27 mm diameter bore, 150 mm stroke, 2.2 kg inertia, and (C) 27 mm diameter bore, 150 mm stroke, 2.2 kg inertia and high damping (created by setting the flow controls near fully closed). The desired overshoot specification with all three actuators was satisfied, while the desired rise time specification with actuator C (with high inertia and damping) was exceeded by 23%. The SSE with an S-curve trajectory was 0.2 mm.

Shih and Ma (1998) developed a PWM-based fuzzy control method for a pneumatic cylinder. The pneumatic system includes a double acting cylinder and two three-way on/off valves. They proposed a modified differential PWM control to avoid the nonlinear characteristics of the switching time of the on/off valves. Experimental results show that the settling time was 0.46 s and SSE was 0.075 mm for 150 mm step input. Also the loading effect was tested by adding a sudden load pressure of 0.5 bar resulting in an SSE of 0.1 mm.

A variable gain proportional plus velocity plus acceleration (PVA) control algorithm was presented by Ahn and Yokota (2005). The pneumatic system included a pneumatic rodless cylinder and eight two-way on/off valves. Pairs of valves were connected in parallel to increase the mass flow rate. The gains of the PVA controller were adjusted using a learning vector quantization neural network (LVQNN) to deal with different payloads. A modified pulse-width modulation (MPWM) scheme similar to the scheme from Shih and Ma (1998) was proposed to compensate for the dead time of the valves. Experiments were performed to verify the effectiveness of the LVQNN by using four different payloads (0, 10 kg, 20 kg and 30 kg). The system response with fixed controller gains became oscillatory for the larger payload while the response with LVQNN remained well damped. The SSE with LVQNN was within 0.4 mm in all of their tests.

Shen et al. (2006) proposed a PWM-based nonlinear model-based SMC law. The system employed two three-way on/off valves. An integral sliding surface was selected for the controller. Experiments were conducted to verify the proposed control law by tracking 20 mm amplitude sinusoidal trajectories at frequencies of 0.25 Hz, 0.5 Hz, and 1

Hz with a 10.8 kg payload mass. The corresponding maximum tracking errors were 1.5 mm, 2 mm and 4 mm, respectively. No robustness test results were included in the paper.

Controllers based on driving the valves with PWM may give acceptable performance, but the valves are switched up to 200 times per second, which may greatly reduce the valve's lifespan. Thus, researchers have studied advanced control algorithms that switch the valves less often than with PWM method. Most of papers used some form of SMC.

Nguyen, Leavitt, Jabbari, and Bobrow (2007) proposed a SMC law for directly switching the valves. Their pneumatic system included a double acting cylinder and four two-way on/off valves. A three-mode SMC controller was designed by defining a second-order sliding surface. The three modes are defined as "push and pull", "pull and push", and "closed and closed". The conditions that guarantee system stability were derived. Experimental results show that the errors are within 2 mm for a 20 mm amplitude 0.5 Hz sine wave. The robustness was verified by varying the mass from 50 % to 400 % of its nominal value. The experiments by square wave tracking also demonstrated that tighter position accuracy requires more valve switching. The proposed SMC method tended to reduce the valve switching frequency and prolong the valve life compared with PWM-based methods.

Moreau, Pham, Tavakoli and Redarce (2012) presented a control design scheme for pneumatic master-slave teleoperation systems using on/off valves. They extended the three-mode control law (SMC3) of Nguyen et al. (2007) to a five-mode control law (5MCL) with the goal of reducing valve switching frequency without losing control precision. They used the same valve configuration as Nguyen et al. (2007). They added two modes termed "push and closed" and "closed and push". The discrete fast Fourier transform was used to analyze frequency responses in the experiments. The magnitude of the spectra of the control signal was lower in the 5MCL case than in the SMC3 case over all frequencies. It was clear that the 5MCL reduced the valve switching frequency.

Hodgson et al. (2012) proposed a new SMC law for position control of pneumatic actuators using on/off valves. The pneumatic system includes a double acting cylinder and four on/off valves. They extended the SMC3 of Nguyen et al. (2007) to a seven-mode control law (SMC7). The four additional modes are "push and close", "pull and close", "close and push" and "close and pull". The stability of the closed-loop system was analyzed. In their experiments, the SMC3 had an 18% overshoot while the SMC7 had only a 1.9% overshoot in square-wave tests. Experiments were also performed to track a multi-sine wave and there was a 48 % reduction in the number of valve switches per second from the SMC3 to the SMC7. Recently, Hodgson et al. (2015) presented an improved version of their SMC7. They proposed a model-based SMC law (MSMCL) that employs PWM. Their model was described earlier in this chapter. In 40 mm step experiments, the root mean square error (RMSE) with the MSMCL was comparable to that obtained with SMC7, while the valve's switches per second (SPS) with MSMCL was only half the value with SMC7. However, in 15 mm square wave tests, the SSE of MSMCL was 0.5 mm whereas with SMC7MBC it was only 0.2 mm. The performances of the position control were similar for $\pm 35\%$ mass differences, demonstrating the robustness of the proposed MSMCL.

Jouppila et al. (2014) proposed a robust nonlinear SMC algorithm for a pneumatic muscle actuator system. The SMC approach was applied to three different valve configurations: one PWM-driven three-way on/off valve, two PWM-driven two-way on/off valves and a servo valve. Their experimental results showed that the RMSE of the dual valve configuration was similar to that of the servo valve, whereas the RMSE of the single valve configuration was 30% larger than that of dual valve one with sinusoidal tracking and a 2kg nominal payload. To test robustness, the payload mass was decreased to 0.5 kg and increased to 4 kg. The on/off valve configurations were extremely robust to the decreased payload mass since their RMSE was smaller than the nominal case. Conversely, the RMSE was increased by 79 % with the dual valve configuration, 46 % with the single valve configuration and only 16% for the servo valve configuration when the payload was increased to 4 kg.

The backstepping design method has also been used in the position control of pneumatic actuators. Rao and Bone (2008) presented a backstepping controller for a pneumatic actuator driven by four two-way proportional valves. Langjord and Johansen (2010) presented a dual-mode switched controller based on backstepping for a spring-return electropneumatic clutch actuator using two two-way on/off valves. The proposed controller combined local and global controllers. They prove the asymptotic stability using Lyapunov functions. Experimental results show that the local controller is used close to the equilibrium point while the global one is used elsewhere. The proposed controller made the system reach the reference point within 0.1 s and produced a steady-state error within 0.2 mm. The combined controller is more accurate, and achieves fewer oscillations and valve switches than using only the local controller or the global controller.

Model predictive control (MPC) refers to an optimization-based control method that uses a dynamic plant model to predict future response of the states based on projected plant inputs. The control signal is the plant input which minimizes a given cost function subject to given constraints. The main advantages of MPC are its ability to deal with the plant's constraints and dead time. Its main disadvantages are its computational complexity and its dependency on a plant model. Due to its computational burdens, MPC was first applied in chemical process control. Recently, researchers have begun to apply MPC to control of pneumatic systems using on/off valves.

Grancharova and Johansen (2011) designed explicit nonlinear model predictive controllers (NMPC) for position control of the same system as Langjord and Johansen (2010). They had to simplify the system model from fifth-order to third-order to reduce the computational time. Two types of explicit NMPC controllers based on the multiparametric nonlinear programming were proposed. One controller applied PWM method (explicit NMPC with PWM), and the other only allows the valves to be fully open or fully closed (explicit quantized NMPC) during each sampling period. Their cost function was:

$$\begin{aligned} J = {} & w_y \bullet \left(\hat{y}\left(t_k + N_P \cdot T_s\right) - y_d\left(t_k\right) \right)^2 \\ & + \sum_{i=0}^{N_p-1} \left[w_Q \bullet \left(\hat{y}\left(t_k + i \cdot T_s\right) - y_d\left(t_k\right) \right)^2 + w_{du} \bullet \Delta \hat{u}\left(t_k + i \cdot T_s\right)^2 \right] \end{aligned} \tag{2.3.1}$$

where t_k is the time of the current sampling instant, T_s is the sampling period, $\hat{y}$ is the predicted position; y_d is the desired position, N_P is the prediction horizon; w_y, w_Q and w_{du} are weighting coefficients; and $\Delta\hat{u}$ is the predicted change in the commanded valve mode. $\Delta\hat{u}$ was defined as follows:

$$\Delta\hat{u}\left(t_k + i\cdot T_s\right) = \begin{cases} \hat{u}\left(t_k\right) - u\left(t_k - T_s\right) & i = 0 \\ \hat{u}\left(t_k + i\cdot T_s\right) - \hat{u}\left(t_k + \left(i-1\right)\cdot T_s\right) & 1 \le i \le N_p - 1 \end{cases} \tag{2.3.2}$$

where u is the actual commanded valve mode and $\hat{u}$ is a prediction of the commanded valve mode. The optimization was subject to the constraint:

$$\left|\hat{y}\left(t_k + N_P\cdot T_s\right) - y_d\left(t_k\right)\right| \le \delta \tag{2.3.3}$$

Choosing δ to satisfy stability and feasibility involves a trade-off. For stability, δ should be made as small as possible. However, δ should be sufficiently large to ensure feasibility since the equilibrium point of the closed-loop system may have an offset from the desired position. The input to each valve is obtained directly from $u\left(t_k\right)$. They used a sampling period of 10 ms in their experiments. Their experimental results show that the control input chattering of explicit NMPC with PWM is comparable to that of PID controller and is smaller than that of SMC controller, while that of explicit quantized NMPC is larger than that of SMC controller. The averaged tracking error using explicit NMPC with PWM of 0.25 mm was smaller than with SMC and PID, but the tracking performance of explicit quantized NMPC was worse. They also showed that the proposed control scheme has low enough computational complexity to be applicable to fast mechatronic systems. They did not study or test the robustness of the controllers.

Bone and Chen (2012) designed a novel discrete-valued model-predictive control (DVMPC) algorithm for position control of the pneumatic cylinder in a hybrid pneumatic-electric actuator. The pneumatic system includes a double acting cylinder and two three-way on/off valves. The cylinder rotated a single-link robot arm using a rack and pinion mechanism. The DVMPC algorithm directly switched the valves without applying the PWM method. An exhaustive search was used to determine the valve inputs that minimized the following cost function:

$$J = \sum_{i=0}^{N_p-1} \left(\hat{y}\left(t_k + i \cdot T_s\right) - y_d\left(t_k\right) \right)^2 \tag{2.3.4}$$

They also employed "move blocking" over the prediction horizon ($\hat{u}\left(t_k + i \cdot T_s\right) = u\left(t_k\right),\ \forall i = 1, 2, ..., N_p - 1$) to limit the search to four possible solutions to reduce the computational burden.

Their experimental results showed that the pneumatic cylinder achieved 2.5% mean absolute error (MAE) for the vertical cycloidal trajectory. The hybrid actuator achieved 0.37% MAE for the same vertical cycloidal trajectory and 1.1% MAE for a vertical sinusoidal trajectory. Their results also demonstrated that the valves switched less often than with the PWM method. Since their DVMPC does not include constraints its feasibility is guaranteed. They did not analyse the stability of the control system, and no robustness tests were performed. Bone, Xue, and Flett (2015) presented an improved version of the control algorithm and experimental results. A payload estimation algorithm was proposed, and shown to improve robustness to unknown payloads. Also, a stability analysis was presented that guarantees the hybrid pneumatic-electric system to be bounded-input, bounded-output stable. DVMPC's cost function and feasibility were unchanged, and the stability of DVMPC acting alone was not analyzed. Simulation results demonstrated that DVMPC outperforms the SMC from Shen et al. (2006) in terms of RMSE, SSE and switches per second (SPS). In their experiments, the pneumatic cylinder (acting alone) achieved 0.7% RMSE (equivalent to 0.34 mm of piston motion) and 0.25% SSE (equivalent to 0.12 mm of piston motion) for vertical rotary cycloidal trajectories. The RMSE was 0.12% and SSE was 0.04% for vertical rotary cycloidal trajectories using the hybrid actuator.

2.4 Summary

The state of the art literature on modeling and position control of pneumatic actuators, particularly by researchers using on/off solenoid valves, was reviewed in this chapter.

Most of the works on the modeling of pneumatic actuators are based on the work of Shearer (1956). Valve modeling and friction modeling are the most difficult aspects. The valve's mass flow rate model is usually obtained by fitting the coefficients of a theoretical nozzle formula to experimental data. Empirical flow rate models have also been proposed and shown to be more accurate. Although friction is a complex phenomenon, most researchers have used relatively simple friction models since they are well suited to model-based control and their parameters can be easily identified. Leakage is usually ignored in the modeling literature.

The poor quantization of on/off valves makes it difficult to achieve the same tracking performance as proportional/servo valves. Researchers have been paying attention to on/off valves in the recent 30 years since they are much smaller and cheaper than proportional valves. PID controller with PWM scheme was mainly used in the early years, but valves switches often to approximate a proportional valve. SMC is the most common nonlinear controller used to both improve tracking performance and reduce valve switching frequency. Recently, MPC has been studied in pneumatic systems with on/off valves due to its ability to deal with constraints and dead time. MPC has been successfully applied to pneumatic actuators thanks to recent improvements in computer speed and optimization algorithms. Under gravity loading, using MPC with on/off valves the best RMSE and SSE achieved to date were 0.34 mm and 0.12 mm, respectively.

CHAPTER 3 SYSTEM MODELING

3.1 Introduction

A pneumatic system is highly nonlinear due to the compressibility of the air, the nonlinearity of the mass flow rate and the variation of the friction. A plant model is necessary for computer simulations and for the development of model-based controllers.

In this chapter, we will derive the plant model for a double acting cylinder driven by four on/off valves. The system architecture is described first. Next, the system hardware is introduced; and the system model including the cylinder dynamics model, friction model and mass flow rate model is derived. Next, the parameters of the friction model and the mass flow rate model are identified. Finally, the developed system model is validated by comparing simulation data with experimental data.

3.2 System architecture

The system hardware is shown schematically in Figure 3.2.1. The pneumatic system consists of a double acting cylinder, a payload mass on a linear slide table and four two-way on/off valves, called V1-V4 in this thesis. Each chamber of the cylinder uses two on/off solenoid valves to control charging and discharging independently. For chamber A, V1 controls the charging from the supply and V2 controls the discharging to the atmosphere. For chamber B, V3 controls the charging from the supply and V4 controls the discharging to the atmosphere. A linear encoder and two pressure sensors are used to measure the piston position and chamber pressures. RC filters with a 95 Hz cutoff frequency are used with the pressure sensors to reduce high frequency noise. Flow control valves are added after the on/off valves to reduce the high frequency pressure fluctuations caused by the valve switching. A PC-based data acquisition and control system obtains sensor signals from and sends control signals to the four valves to track the desired trajectory.

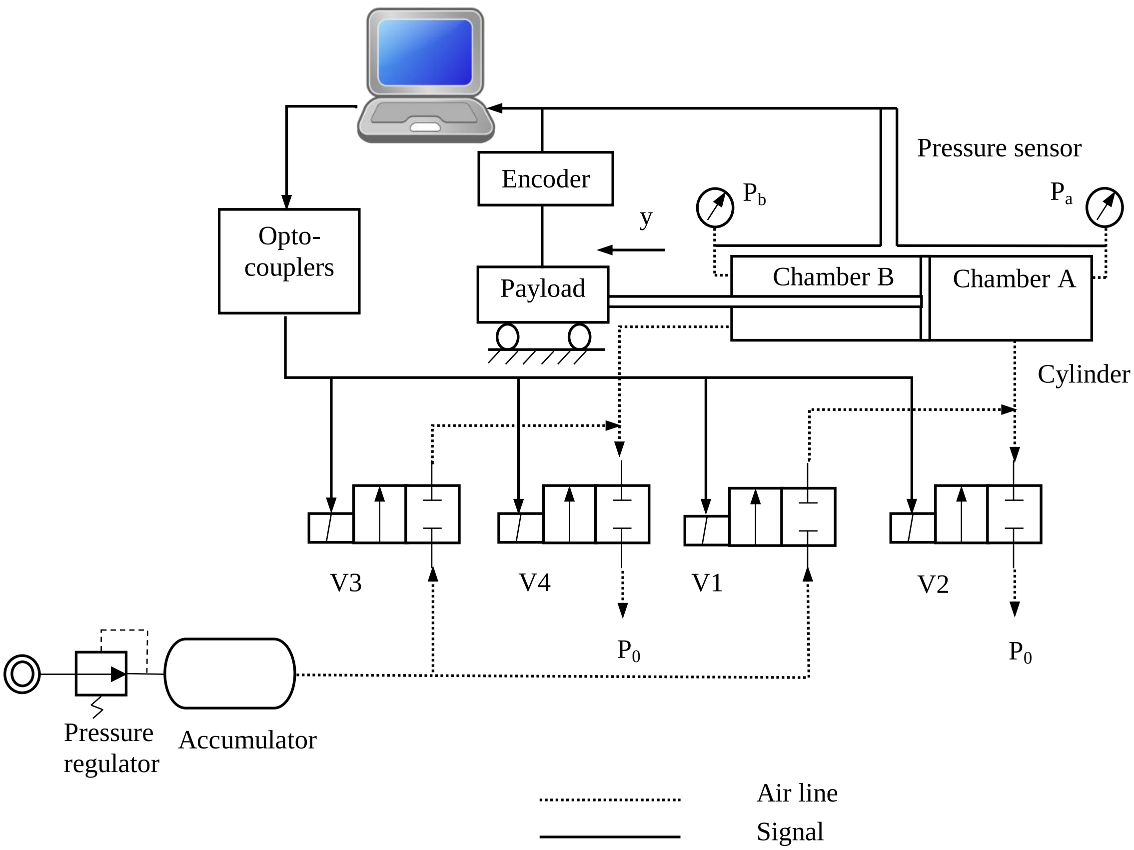

Figure 3.2.1 System schematic diagram

3.3 System hardware

The cylinder (Festo Corporation, model number DGPL-25-600) is rodless; and has a 600 mm stroke and 25 mm bore. It has high friction due to its seals, and will be referred to as the high friction cylinder (HFC) in the remainder of this thesis. The four on/off valves are made by MAC with model number 34B-AAA-GDFB-1BA. The flow control valves are made by SMC, model number SMC AS2200. The encoder has a resolution of 0.01 mm. The pressure sensors are made by SSI Technologies with model number P51-100-A-B-I36-5V-000-000. All of the sensor signals and control signals are interfaced with the PC through a National Instruments PCIe-6365 card. The PC is running 64-bit Windows 7 with a 3.10 GHz Intel i5-2400 processor and 8.00 GB RAM. This data acquisition and control system is programmed in C language and operates at a 1 kHz sampling frequency. The supply pressure for the HFC was set to 0.6 MPa. A photograph of the system is shown in Figure 3.3.1.

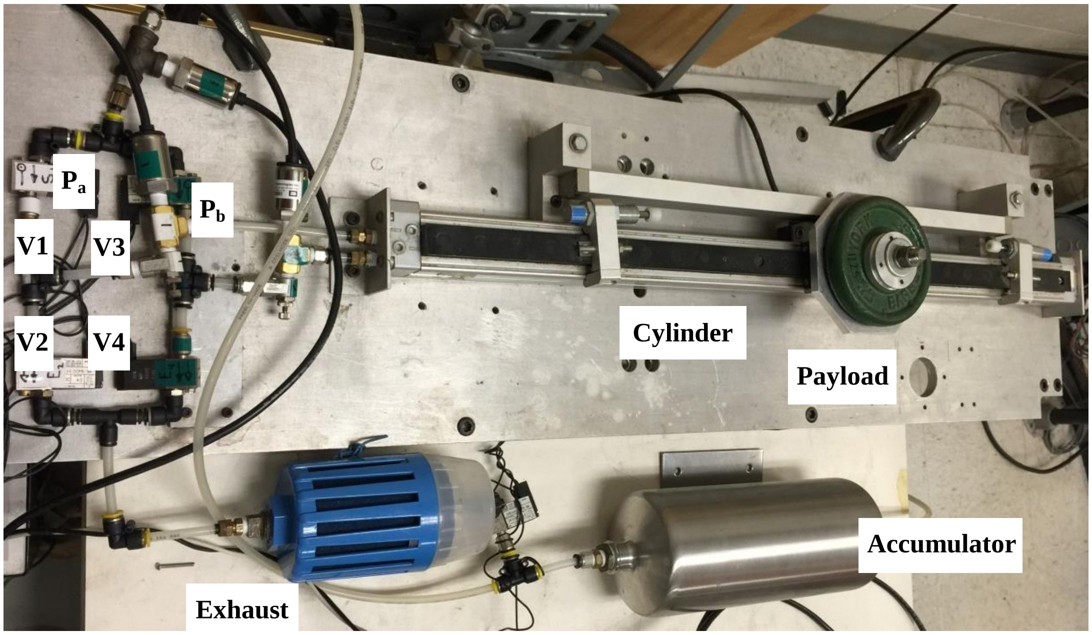

Figure 3.3.1 Photograph of the HFC system (the PC and optocouplers are not shown).

3.4 Cylinder dynamics model

The model of the dynamics of the pneumatic cylinder is primarily based on the work of Shearer (1956). The energy conservation equation is first applied to the chamber A:

$$\frac{d}{dt}\left(c_v \rho_a V_a T_a\right) = c_p T_a \frac{dm_a}{dt} + \frac{dQ}{dt} - P_a \frac{dV_a}{dt} \tag{3.4.1}$$

where $\frac{d}{dt}\left(c_v \rho_a V_a T_a\right)$ is the total rate of internal energy of the chamber A, m_a is the mass of air in chamber A, P_a is the pressure inside chamber A, T_a is the temperature inside chamber A, V_a is the volume of chamber A, $c_p T_a \frac{dm_a}{dt}$ is the rate of internal energy of the mass flow into the chamber A, $\frac{dQ}{dt}$ is the rate of heat transfer into the chamber A and

$P_a \frac{dV_a}{dt}$ is the work done by the piston. Assuming the air behaves as an ideal gas, its density is $\rho_a = \frac{P_a}{RT_a}$, where R is the gas constant. Since the process is assumed to be adiabatic, we have $\frac{dQ}{dt} = 0$. The change of the temperature is neglected, so we have $T_a = T_b = T$, where T is the ambient temperature. According to the analysis above, Equation (3.4.1) can be written as

$$\frac{c_v}{R}\frac{d}{dt}\left(P_a V_a\right) = c_p T \frac{dm_a}{dt} - P_a \frac{dV_a}{dt}. \tag{3.4.2}$$

Then we have

$$\frac{c_v}{R} P_a \frac{d}{dt}\left(V_a\right) + \frac{c_v}{R} V_a \frac{d}{dt}\left(P_a\right) = c_p T \frac{dm_a}{dt} - P_a \frac{dV_a}{dt} \tag{3.4.3}$$

This equation can be rearranged as

$$c_p T \frac{dm_a}{dt} = \frac{c_v + R}{R} P_a \frac{dV_a}{dt} + \frac{c_v}{R} V_a \frac{dP_a}{dt} \tag{3.4.4}$$

For an ideal gas, we have $K = \frac{c_p}{c_v}$ and $c_p = c_v + R$, where K is the specific heat ratio ($K = 1.4$ for air). Equation (3.4.4) can be written as

$$KRT \frac{dm_a}{dt} = KP_a \frac{dV_a}{dt} + V_a \frac{dP_a}{dt} \tag{3.4.5}$$

Similarly, the dynamic equation for the chamber B is

$$KRT \frac{dm_b}{dt} = KP_b \frac{dV_b}{dt} + V_b \frac{dP_b}{dt} \tag{3.4.6}$$

The volumes of the two chambers V_a and V_b can be expressed as

$$V_a = A_a y \text{ and} \tag{3.4.7}$$

$$V_b = A_b \left(L - y\right) \tag{3.4.8}$$

where y is the payload displacement; A_a and A_b are the cross-sectional area of the two chambers with $A_a = A_b$; and L is the stroke length. The range of y is

$$y_{a0} \le y \le y_{b0} \tag{3.4.9}$$

where y_{a0} is minimum payload displacement and y_{b0} is the maximum payload displacement. Note that $y_{a0} > 0$ and $y_{b0} < L$. $V_{a0} = A_a y_{a0}$ and $V_{b0} = A_b\left(L - y_{b0}\right)$ are the dead volumes of the two chambers. After differentiating both sides of Equations (3.4.7) and (3.4.8), we have

$$\dot{V}_a = A_a \dot{y} \text{ and} \tag{3.4.10}$$

$$\dot{V}_b = -A_b \dot{y} \tag{3.4.11}$$

Then Equations (3.4.5) and (3.4.6) can be rewritten as

$$KRT\dot{m}_a = KA_a \dot{y} P_a + A_a y \dot{P}_a \text{ and} \tag{3.4.12}$$

$$KRT\dot{m}_b = -KA_b \dot{y} P_b + A_b \left(L - y\right) \dot{P}_b \tag{3.4.13}$$

The mass flow rates $\dot{m}_a$ and $\dot{m}_b$ into the two chambers are

$$\dot{m}_a = \dot{m}_1 - \dot{m}_2 \tag{3.4.14}$$

$$\dot{m}_b = \dot{m}_3 - \dot{m}_4 \tag{3.4.15}$$

where $\dot{m}_1$, $\dot{m}_2$, $\dot{m}_3$, and $\dot{m}_4$ are the mass flow rates through the four valves. These are functions of the control signals and chamber pressures. The mass flow rate functions will be presented in the section 3.6 in detail. Based on the Newton's second law, the dynamic equation of the payload is

$$M\ddot{y} = P_a A_a - P_b A_b - F_f \tag{3.4.16}$$

where M is the mass of the payload and F_f is the friction force. F_f is a complex force related to the direction and the velocity of the movement. Its equations will be described in the section 3.5 in detail.

3.5 Friction model

The friction was estimated using

$$\hat{F}_f = P_a A_a - P_b A_b - M\hat{a} \tag{3.5.1}$$

where $\hat{F}_f$ is the estimated friction force and $\hat{a}$ is the estimated acceleration. With pneumatic cylinders, it is known that the magnitude of the friction force can be different in the positive and negative directions even when the speed is the same (Wang et al., 2001). Thus, we separately modeled the friction forces in the two movement directions.

Open-loop tests were performed on the system to obtain the raw data. Five experiments, each with 4 s duration, were performed using different random input signals for the valves. The random input signals were restricted to the three discrete modes:

Mode 1: both chambers' valves are closed ($u_1 = 0$, $u_2 = 0$, $u_3 = 0$ and $u_4 = 0$);

Mode 2: chamber A charges and chamber B discharges ($u_1 = 1$, $u_2 = 0$, $u_3 = 0$ and $u_4 = 1$);

Mode 3: chamber A discharges and chamber B charges ($u_1 = 0$, $u_2 = 1$, $u_3 = 1$ and $u_4 = 0$).

Mode 2 is used to move the piston to the positive direction and mode 3 is used to move it in the negative direction. In these experiments, the modes were randomly generated using a uniform probability distribution. The sampling period was 1 ms. The input signal to each valve was held using a zero-order hold (ZOH). The minimum duration of one mode is set equal to the ZOH period since there is a delay when opening and closing valves. The value of the ZOH period should be large enough to make the payload move and small enough to avoid it hitting the end of its travel. The measure pressure and position data are shown in Figure 3.5.1. The estimated velocity and acceleration are also shown. They were estimated from the position data by central differencing and digital low-pass filtering. As the plots demonstrate, there was a lot of noise when the filter was not used, especially in the acceleration estimates. A zero-phase finite impulse response low-pass filter was used to filter the raw data. The cutoff frequency and window width were manually tuned to smooth out the ripples.

After the data collection and pre-processing, the friction forces were estimated using (3.5.1). The velocity-friction map from the five experiments is shown in Figure 3.5.2. Dynamic friction is usually modeled as a nonlinear function of relative velocity of the sliding surfaces in pneumatic systems.

It was interesting to find that the friction forces were different with the same velocity of the payload. For example, the largest friction force is 69.6 N and the smallest one is only 35.5 N when the velocity of the piston is 0.162 m/s. Thus, the friction forces do not only depend on the velocity of the piston and the classical friction model is not applicable. According to Schroeder and Singh (1993), the gap is due to the pressure difference between the cylinder chambers. The classical model for pneumatic actuator friction is ((Armstrong-Hélouvry et al. (1994); and Rao and Bone (2008))

$$F_f(\dot{y}) = \begin{cases} \left[F_c + (F_s - F_c)e^{-(\dot{y}/v_{s,p})^2}\right]\text{sgn}(\dot{y}) + C_v\dot{y} & \dot{y} \neq 0 \\ F_p & \dot{y} = 0 \text{ and } |F_p| < F_s \\ F_s & \dot{y} = 0 \text{ and } |F_p| \geq F_s \end{cases} \tag{3.5.2}$$

where $\dot{y}$ is the velocity of the payload, sgn$(\cdot)$ is the signum function, F_p is the applied external force, F_c is the Coulomb friction force, C_v is the viscous friction coefficient, v_s is the Stribeck velocity, and F_s is the static friction force.

For our model, we extended the classical friction model to include direction dependent parameters and we also made the friction force dependent on the pressure difference to obtain

$$F_f(\dot{y}, \Delta P) = \begin{cases} \left[F_{c,p}(\Delta P) + \left(F_{s,p}(\Delta P) - F_{c,p}(\Delta P)\right)e^{-(\dot{y}/v_{s,p})^2}\right] + C_{v,p}\dot{y} & \dot{y} > 0 \\ -\left[F_{c,n}(\Delta P) + \left(F_{s,n}(\Delta P) - F_{c,n}(\Delta P)\right)e^{-(\dot{y}/v_{s,n})^2}\right] + C_{v,n}\dot{y} & \dot{y} < 0 \\ F_p & \dot{y} = 0 \text{ and } 0 < F_p < F_{s,p} \\ F_p & \dot{y} = 0 \text{ and } -F_{s,n} < F_p < 0 \\ F_{s,p}(\Delta P) & \dot{y} = 0 \text{ and } F_p > F_{s,p} \\ -F_{s,n}(\Delta P) & \dot{y} = 0 \text{ and } F_p < -F_{s,n} \end{cases} \tag{3.5.3}$$

where ΔP is the pressure difference between the cylinder chambers, defined as $\Delta P = P_a - P_b$; F_p is the applied external force ; $F_{c,p}$ and $F_{c,n}$ are the Coulomb friction force for the positive direction and for the negative direction, respectively; $C_{v,p}$ and $C_{v,n}$ are the viscous friction coefficient forces for the two directions; $v_{s,p}$ and $v_{s,n}$ are the Stribeck velocities for the two directions; and $F_{s,p}$ and $F_{s,n}$ are the static friction forces for the two directions. Examining (3.5.2), the friction force depends on the velocity of the payload and the pressure difference between the cylinder chambers. When the payload is static and the applied external force is less than the static friction force, friction force equals to the applied external force. When the applied external force is larger than the static friction, the payload begins to move. The dynamic friction force includes the Stribeck effect, Coulomb friction force, viscous friction force and the force due to the pressure difference between chambers.

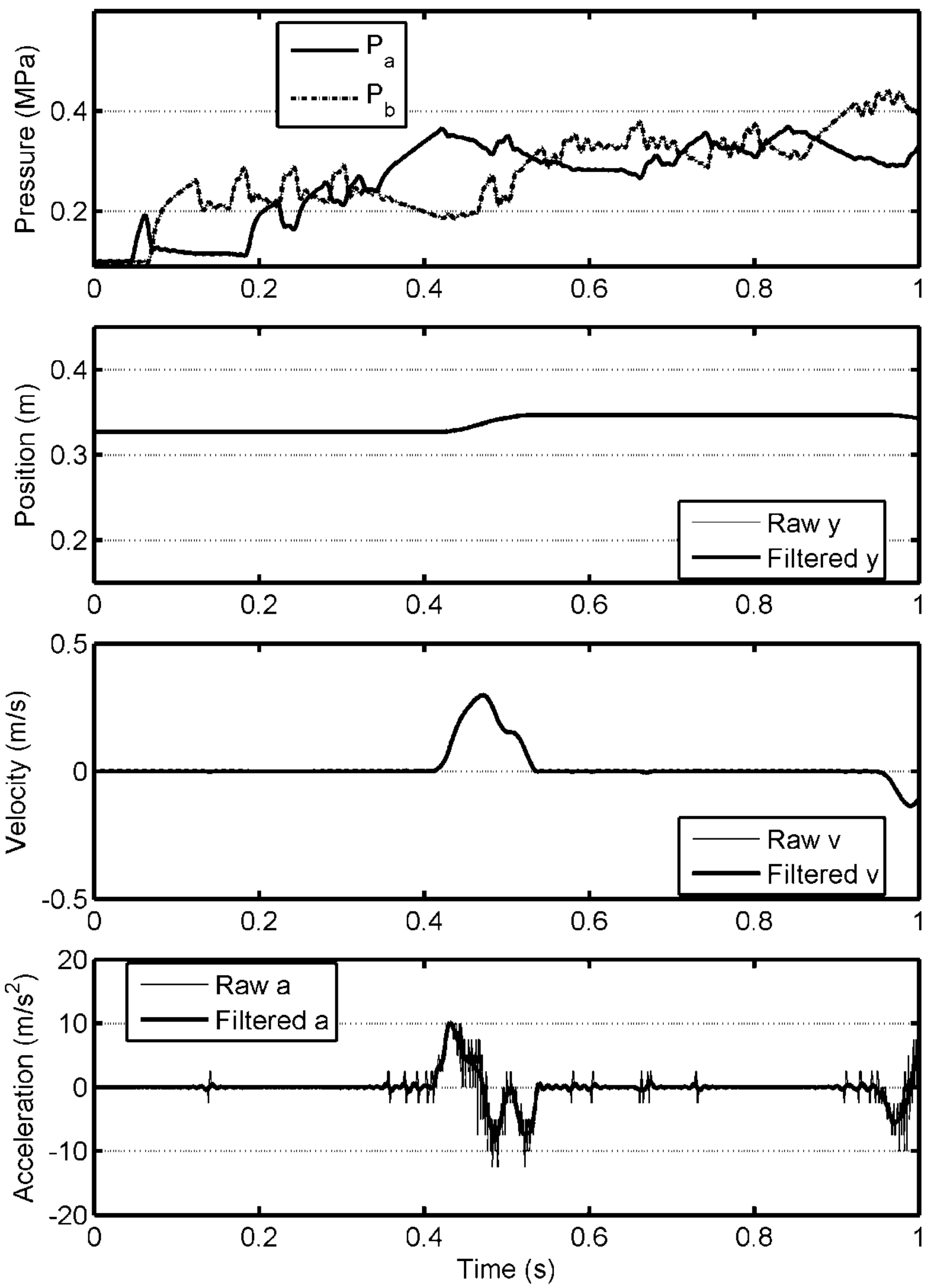

Figure 3.5.1 Raw and filtered pressure, position, velocity and acceleration data obtained from 1 s of a 4 s open-loop friction modeling experiment.

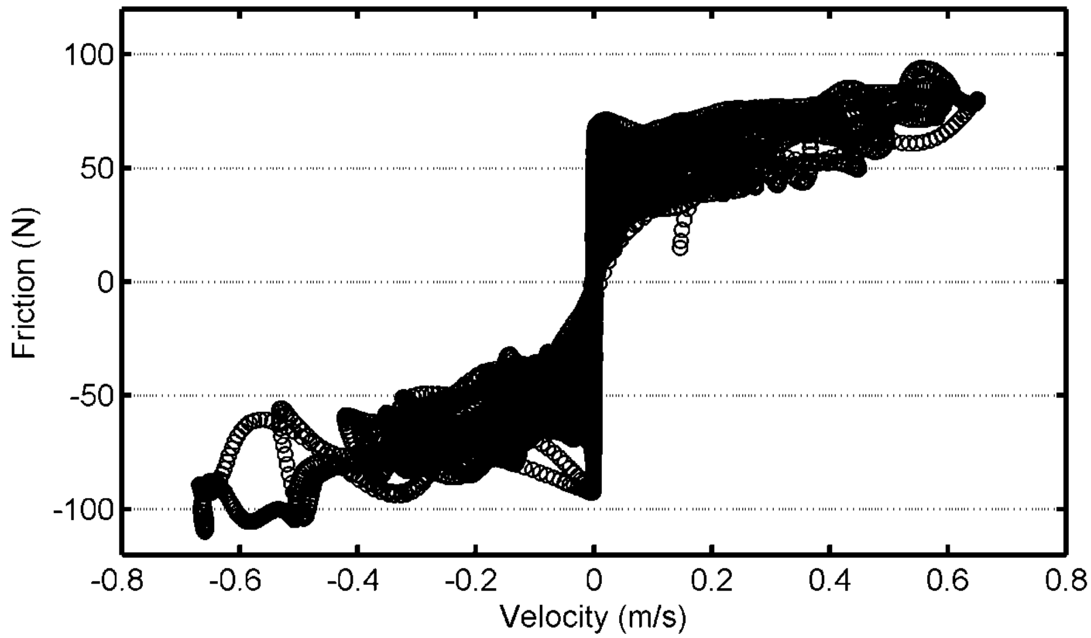

Figure 3.5.2 The velocity-friction map from five 4 s experiments.

The parameter identification will start with the static friction forces $F_{s,p}$ and $F_{s,n}$. They are modeled as linear functions of ΔP as follows

$$F_{s,p}\left(\Delta P\right) = F_{s0,p} + \alpha_{p,p}\Delta P \quad \text{and} \tag{3.5.4}$$

$$F_{s,n}\left(\Delta P\right) = -F_{s0,n} + \alpha_{p,n}\Delta P \tag{3.5.5}$$

where $F_{s0,p}$ is static friction force in the positive direction when $\Delta P = 0$; $F_{s0,n}$ is static friction force in the positive direction when $\Delta P = 0$; and $\alpha_{p,p}$ and $\alpha_{p,n}$ are parameters. Note that $F_{s0,p}$, $F_{s0,n}$, $\alpha_{p,p}$ and $\alpha_{p,n}$ are positive numbers. $F_{s0,p}$ and $F_{s0,n}$ were measured by a digital force gauge. We stopped the air supply to the pneumatic system and disconnected the chambers from the other components. By this method, the chamber pressures were both atmospheric, i.e. $\Delta P = 0$. A digital force gauge held parallel with the slide was used to push the piston until the piston moved. The static friction was assumed to be the largest force measured when the piston just started to move. Ten tests were done for each direction, and the results are listed in Table 3.5.1. The average values for two directions were used for $F_{s0,p}$ and $F_{s0,n}$. The results were $F_{s0,p} = 56.7\text{N}$ and $F_{s0,n} = 56.9\text{N}$. $\alpha_{p,p}$ and $\alpha_{p,n}$ were identified using $F_{s0,p}$ and data collected by open-loop tests. F_f and ΔP were recorded when the movement of piston was larger than the encoder resolution of 0.01 mm. The data are $F_f = 66.1\text{N}$ as $\Delta P = 0.14\text{MPa}$ and $F_f = -71.1\text{N}$ as $\Delta P = -0.14\text{MPa}$. Substituting these values into (3.5.3) and (3.5.4), and solving for $\alpha_{p,p}$ and $\alpha_{p,n}$, gives: $\alpha_{p,p} = 6.66\times10^{-5}\,\text{N/Pa}$ and $\alpha_{p,n} = 1.01\times10^{-4}\,\text{N/Pa}$.

Table 3.5.1 Measurement of static friction force (N) with ΔP = 0.

Direction / Test number	Positive	Negative
Test 1	57.33	57.13
Test 2	57.62	56.25
Test 3	57.13	58.31
Test 4	56.74	57.62
Test 5	56.64	55.76
Test 6	58.02	57.33
Test 7	55.76	55.86
Test 8	56.74	57.33
Test 9	54.88	57.13
Test 10	56.35	56.94
Average	56.72	56.94

The Coulomb friction forces were also modeled as linear functions of ΔP as follows

$$F_{c,p}\left(\Delta P\right) = F_{c0,p} + \beta_{p,p}\Delta P \quad \text{and} \tag{3.5.6}$$

$$F_{c,n}\left(\Delta P\right) = -F_{c0,n} + \beta_{p,n}\Delta P \tag{3.5.7}$$

where $F_{c0,p}$ is static friction force in the positive direction when $\Delta P = 0$; $F_{c0,n}$ is static friction force in the positive direction when $\Delta P = 0$; and $\beta_{p,p}$ and $\beta_{p,n}$ are parameters.

For the friction model in equation (3.5.2), we need to identify eight more parameters: $F_{c0,p}$, $F_{c0,n}$, $C_{v,p}$, $C_{v,n}$, $\beta_{p,p}$, $\beta_{p,n}$, $v_{s,p}$ and $v_{s,n}$. The Stribeck effect is only active when the velocity is small. The velocity data less than 0.02 m/s was used to identify the parameters $v_{s,p}$ and $v_{s,n}$. They were obtained via manual tuning. This left the six unknown parameters: $F_{c,p}$, $F_{c,n}$, $C_{v,p}$, $C_{v,n}$, $\beta_{p,p}$ and $\beta_{p,n}$. In each direction, the dynamic friction model (beyond the Stribeck effect) is a linear function of the variables $\dot{y}$ and ΔP as follows

$$F_f\left(\dot{y},\Delta P\right) = \begin{cases} F_{c0,p} + \beta_{p,p}\Delta P + C_{v,p}\dot{y} & \dot{y} > 0.02 \text{ m/s} \\ -F_{c0,n} + \beta_{p,n}\Delta P + C_{v,n}\dot{y} & \dot{y} < -0.02 \text{ m/s} \end{cases} \tag{3.5.5}$$

This equation was fit to the data shown in Figure 3.5.2 using the method of least squares (2397 data points for the positive direction and 2748 points for the negative direction). The results are shown in Table 3.5.2.

Table 3.5.2 HFC friction model parameters.

Direction	F_{s0} (N)	α_p (N/Pa)	F_{c0} (N)	C_v (N/m/s)	β (N/Pa)	v_s (m/s)
Positive	56.7	6.66×10^{-5}	26.3	35.40	1.99×10^{-4}	0.0189
Negative	56.9	1.01×10^{-4}	24.4	42.01	2.28×10^{-4}	0.0189

In statistics, the coefficient of determination, denoted R^2, is a number that indicates how well data fit a statistical model. R^2 is defined as follows:

$$R^2 = 1 - \frac{SS_{\text{res}}}{SS_{\text{tot}}} \tag{3.5.6}$$

where $SS_{\text{res}} = \sum_i \left(y_i - \hat{y}_i\right)^2$ is called residual sum of squares; $SS_{\text{tot}} = \sum_i \left(y_i - \bar{y}_i\right)^2$ is called total sum of squares; y_i, $\hat{y}_i$ and $\bar{y}_i$ are measured, predicted and mean value, respectively. If R^2 is more close to 1, it means the linear motor better fits the data. For the proposed friction model (3.5.3)-(3.5.7) the values of R^2 for the positive and negative directions are 0.87 and 0.88, respectively. For the classical friction model (3.5.2), the values of R^2 for positive direction and negative direction are 0.44 and 0.49, respectively using the same data. These values demonstrate that the proposed friction model is more accurate.

3.6 Mass flow rate model

The HFC is a rodless cylinder with a tight seal, so we can ignore leakage across the piston (between chamber A and chamber B) and across the rod seal. The models of the mass flow rates $\dot{m}_a$ and $\dot{m}_b$ constitute the valve model. The mass flow rate $\dot{m}_a$ is controlled by valves V1 and V2, that is, V1 controls the charging from the supply and V2 controls the discharging to the atmosphere. For simplicity, the combination of V1 and V2 is called valve A. Similarly, the V3 and V4 combination is called valve B. Due to manufacturing tolerances, valve A and valve B are not identical so we must model them separately.

It is difficult to measure the mass flow rate directly since it requires expensive and complicated instruments. The mass flow rate model required for control purposes should not be a function of the valve's internal structure (e.g. the spool's shape) since that would make it unnecessarily complicated. Instead, we used the pressure-time curves to obtain the mass flow rate models and only needed to measure the chamber pressures. The mass flow rates could have been calculated using (3.4.12), (3.4.13), the estimated rate of change of the pressures and the estimated velocity. However, numerical differentiation always amplifies high frequency noise so an approach not requiring the velocity estimation was used. The piston was first held stationary at the far end of the stroke to maximize the chamber volume. Then the following simplified versions of (3.6.1) and (3.6.2) could be used to estimate the mass flow rates

$$\hat{\dot{m}}_a = \frac{A_a y \hat{\dot{P}}_a}{KRT} \text{ and} \tag{3.6.1}$$

$$\hat{\dot{m}}_b = \frac{A_b \left(L - y\right) \hat{\dot{P}}_b}{KRT} \tag{3.6.2}$$

where the "^" symbol indicates an estimated quantity.

We will use the modeling of valve A as an example. The piston was fixed at the end of chamber B to maximum the chamber A volume. The initial pressures in chambers A and B were atmospheric pressure. V3 was off and V4 was on during the whole test to keep chamber B at atmospheric pressure. V1 was turned on and V2 was turned off at 1 s to charge chamber A up to the supply pressure. V1 was turned off at 3 s. Next, V2 was turned on at 3.1 s to discharge chamber A back down to atmospheric pressure. Figure 3.6.1 shows the chamber A pressure vs. time for this experiment. $\dot{P}_a$ was estimated using central differencing. Then the mass flow rate $\dot{m}_a$ was estimated using (3.6.1).

The valves need time to energize and de-energize when they receive control signals thus they need time to fully open or fully close. The switch on delay of the MAC valve is about 4 ms and switch off delay is about 2 ms. The sampling period T_s of 1 ms is less than switch on/off delay time. We therefore need to model dynamics of the valve switching.

To simplify the calculation, we model valve energizing and de-energizing as an integrator that saturates at 0 and 1. The mass flow only occurs when the valve is fully opened according to the model of its internal state. Thus, the mass flow rates into chamber A and B are given by

$$\dot{m}_1(t_k) = \lambda_{fill}\left(P_a(t_k)\right), \quad \text{if } s_1(t_k) = 1, \tag{3.6.3}$$

$$\dot{m}_2(t_k) = \lambda_{dis}\left(P_a(t_k)\right), \quad \text{if } s_2(t_k) = 1, \tag{3.6.4}$$

$$\dot{m}_3(t_k) = \lambda_{fill}\left(P_b(t_k)\right), \quad \text{if } s_3(t_k) = 1, \tag{3.6.5}$$

$$\dot{m}_4(t_k) = \lambda_{dis}\left(P_b(t_k)\right), \quad \text{if } s_4(t_k) = 1, \tag{3.6.6}$$

$$s_i(t_k) = \begin{cases} \min\left(1, s_i(t_k - T_s) + 1/\tau_{d,open}\right), & u_i(t_k) = 1, \forall i \in \{1,2,3,4\} \\ \max\left(0, s_i(t_k - T_s) - 1/\tau_{d,close}\right), & u_i(t_k) = 0, \forall i \in \{1,2,3,4\} \end{cases}, \tag{3.6.7}$$

$$\lambda_{fill}\left(P\right)=\begin{cases} c_{choked,fill}P_s & \text{if } P_s>\dfrac{P}{\zeta_{choked}} \\ c_{fill}\sqrt{P_s-P} & \text{if } P_s\le\dfrac{P}{\zeta_{choked}} \end{cases} \quad \text{and} \tag{3.6.8}$$

$$\lambda_{dis}\left(P\right)=c_{dis}\left(P_0-P\right) \tag{3.6.9}$$

where t_k is the time of the current sampling instant; u_1-u_4 are the command signals for the four valves; s_1 - s_4 are the internal states of the four valves; $\tau_{d,open}$ is the valve energizing delay time; $\tau_{d,close}$ is the valve de-energizing delay time; P_a and P_b are the pressures in chambers A and B, respectively; P_s is the supply pressure; P_0 is the atmospheric pressure; $c_{choked,fill}$ is the filling choked mass flow rate coefficient; c_{fill} is the chamber filling coefficient; c_{dis} is the chamber discharging coefficient; and ζ_{choked} is the pressure ratio used to determine when the mass flow is choked or unchoked.

Note that (3.6.8) and (3.6.9) are similar to the mass flow rate equations of Bone, Xue and Flett (2015). The difference is that they assumed $\zeta_{choked}=0.54$ (for both charging and discharging) which is the theoretical value used by many researchers. In this thesis the ζ_{choked} value for charging was estimated as $\zeta_{choked}=0.29$ by studying the experimental pressure vs. time curve. For discharging, no choked region was observed so ζ_{choked} does not appear in (3.6.11). Valve A coefficients $c_{choked,fill}$, c_{fill}, and c_{dis} were identified by curve fitting using the method of least squares. Note that to obtain c_{fill} it was necessary to first square the equation to eliminate the square root. Similar experiments and curve fitting were used to identify the valve B coefficients. The data used for modeling valve B are shown in Figure 3.6.4. The valve A and valve B coefficients are listed in Table 3.3.2. Filling and discharging simulation results and experiment data are compared in Figures 3.6.4-3.6.7. The results demonstrate that the models fit both the transient and steady-state pressure well.

Table 3.6.1 Fitted valve filling and discharging coefficients

	$C_{fill}\left(\sqrt{m\cdot kg}\right)$	$C_{dis}\left(m\cdot s\right)$	$C_{choked,fill}\left(m\cdot s\right)$
Valve A	3.74×10^{-6}	4.65×10^{-9}	1.97×10^{-8}
Valve B	4.33×10^{-6}	4.89×10^{-9}	2.30×10^{-8}

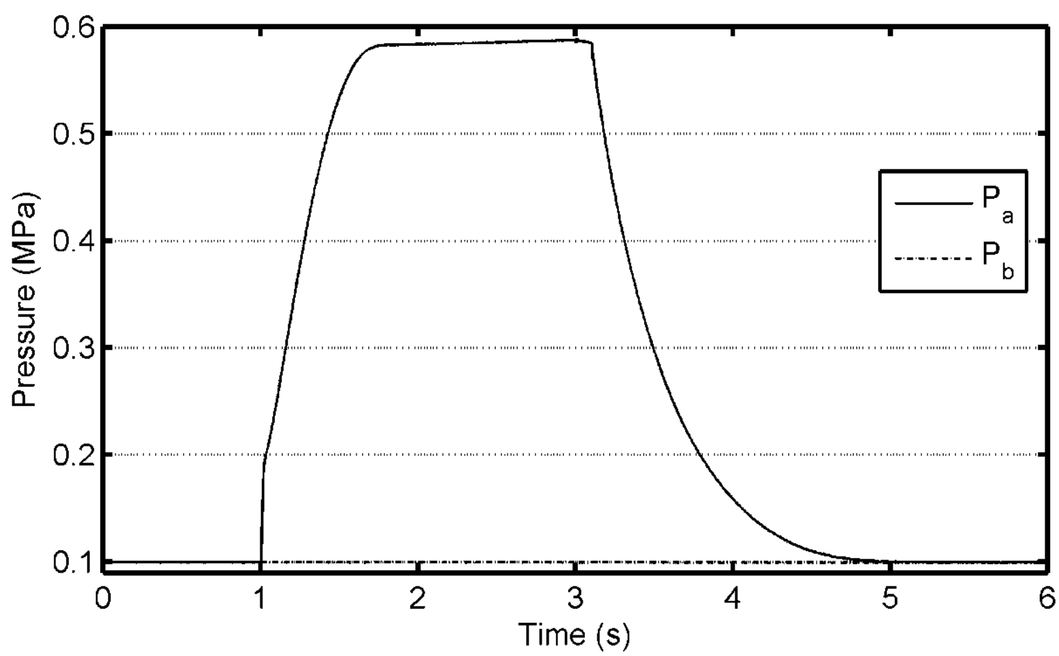

Figure 3.6.1 Pressure vs. time data used for valve A modeling

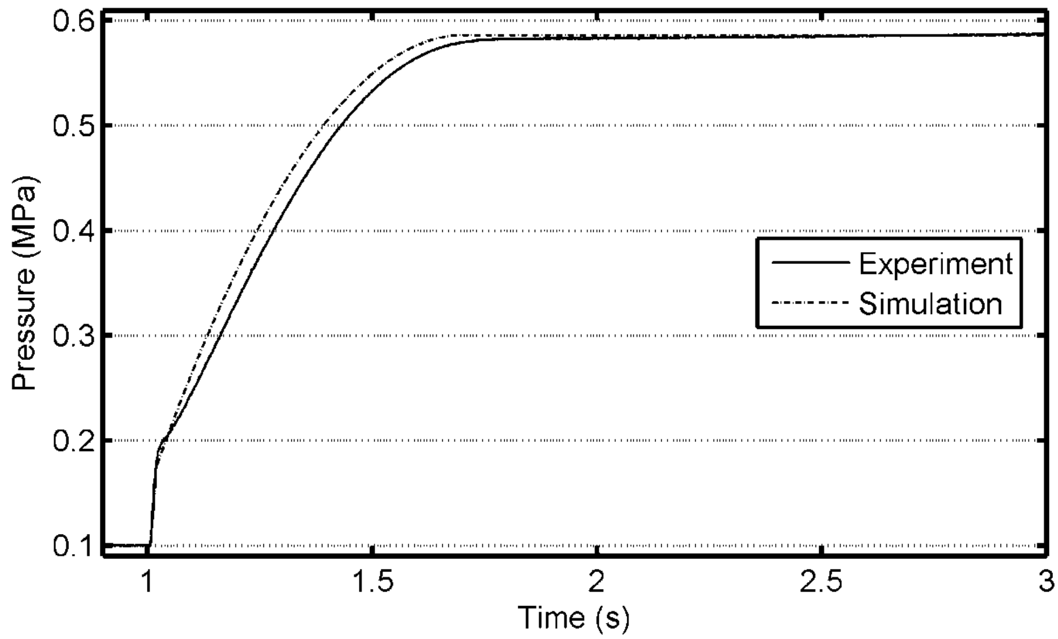

Figure 3.6.2 Comparison of valve A filling results from simulation and experiment.

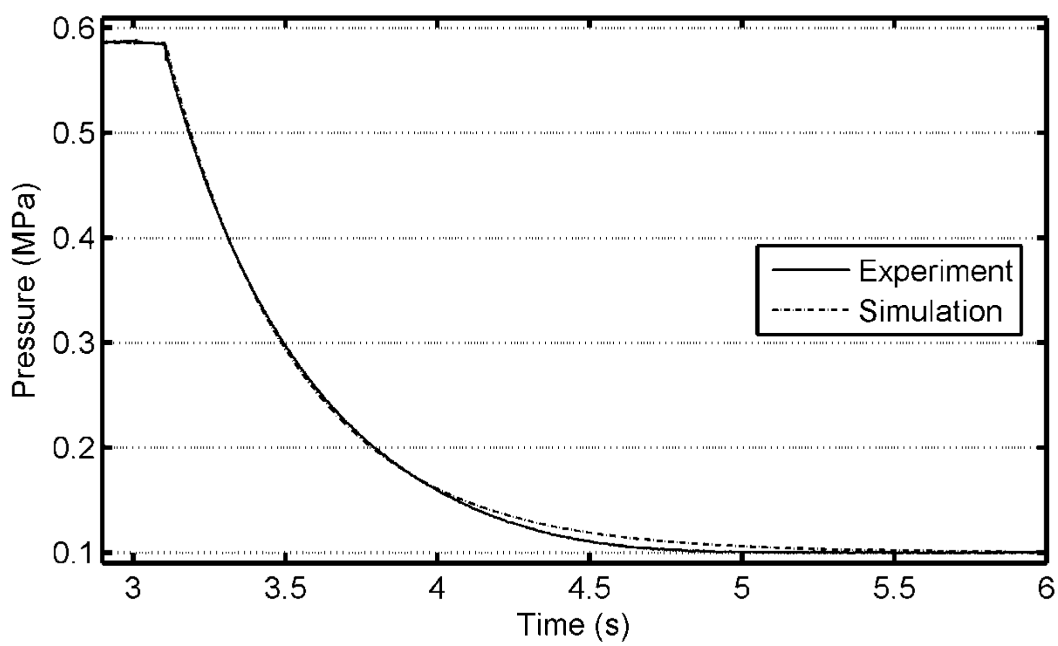

Figure 3.6.3 Comparison of valve A discharging results from simulation and experiment.

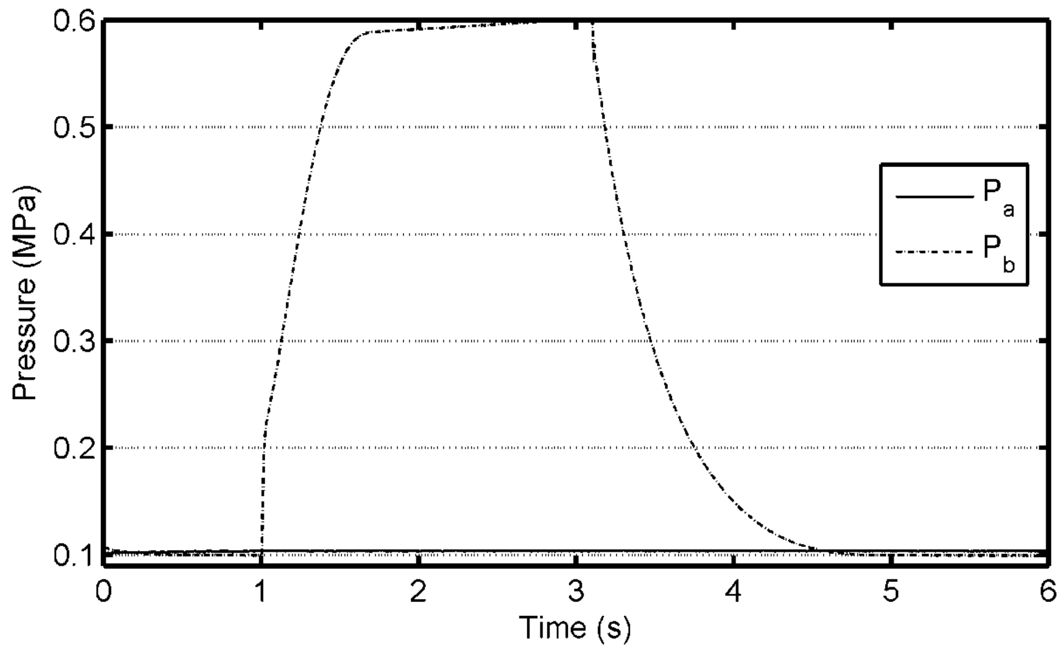

Figure 3.6.4 Pressure vs. time data used for valve B modeling

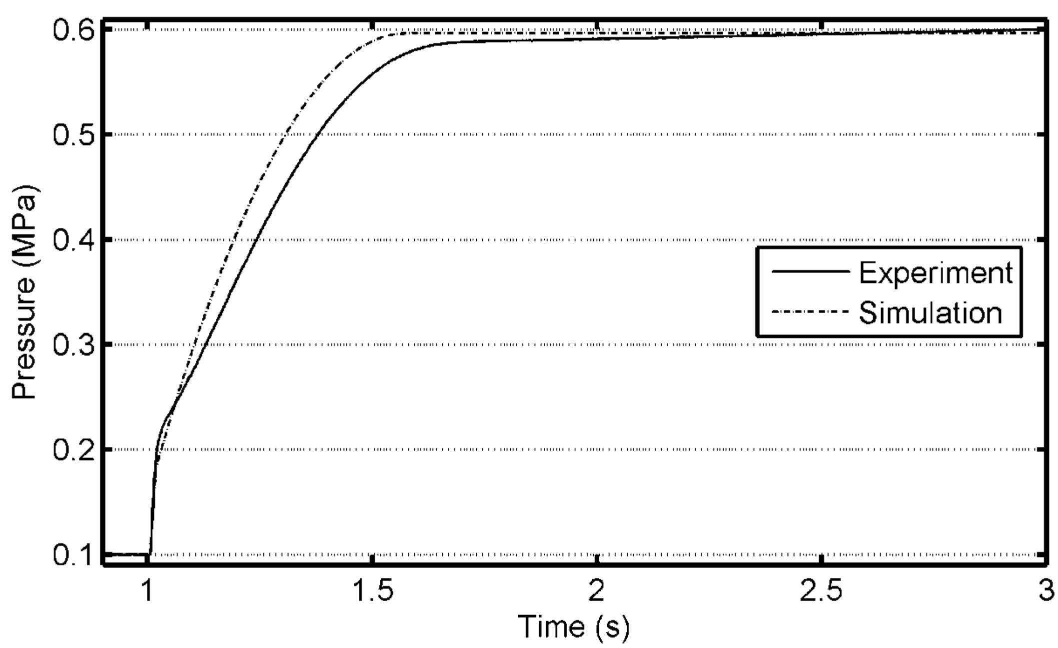

Figure 3.6.5 Comparison of valve B filling results from simulation and experiment.

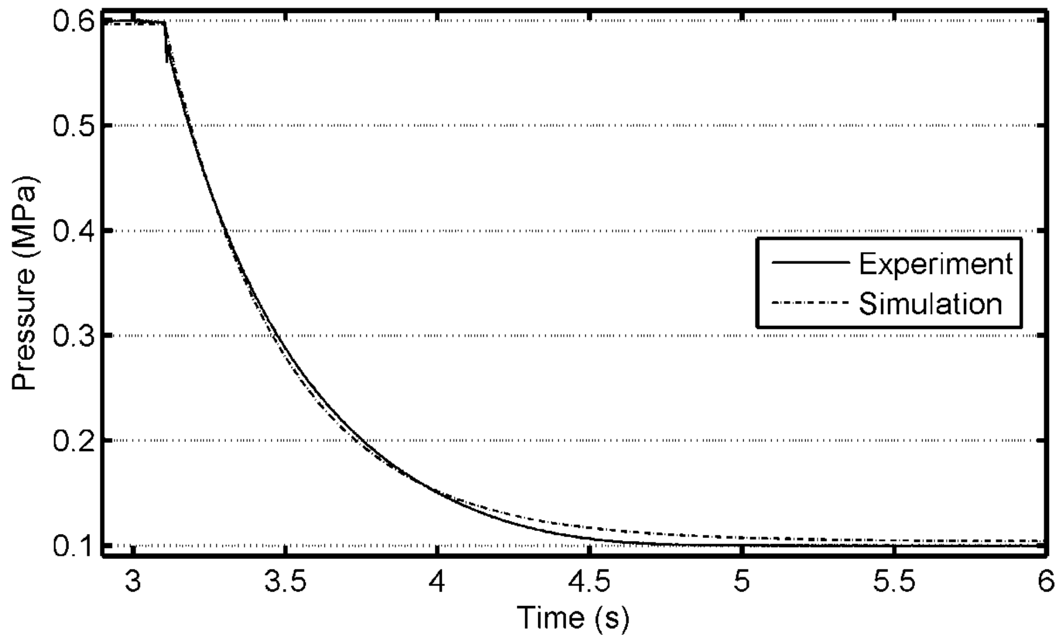

Figure 3.6.6 Comparison of valve B discharging results from simulation and experiment.

3.7 Validation of the model

In the previous sections, the system model of HFC has been derived and the model parameters have been identified. This section compares the results from the simulated system model with experimental results. The mode definitions are the same as those described in section 3.5.

Since the friction and valve parameters are independent, we will first show the simulation results for the position and pressure separately to demonstrate the individual predictive capabilities of the cylinder dynamics model and valve models. Then we will show the predictions obtained using the system model combining those models.

First, we demonstrate the friction model. We use the measured pressure data P_a and P_b to predict the acceleration $\hat{a}$ with the equation

$$\hat{a} = \left(P_a A_a - P_b A_b - \hat{F}_f \right) / M \tag{3.7.1}$$

where $\hat{F}_f$ uses the friction model (3.5.2) with the identified friction parameters. Then, velocity $\hat{v}$ and position $\hat{y}$ are integrated from $\hat{a}$ using the Verlet method (Verlet, 1967). The Verlet method was chosen since it is executes faster than more accurate methods such as the Runge-Kutta methods, while still being much more accurate than the very fast Euler method, especially for larger time steps. Verlet integration is more accurate than Euler integration, especially with large sampling period. The superior performance of the Verlet integration method is demonstrated for an underdamped mass-spring-damper system in Figure 3.7.1. The Euler method uses the forward difference approximation to the first derivative in differential equations of order one, while the Verlet method can the seen as using the central difference approximation to the second derivative. The basic Verlet algorithm is

$$x\left(t + T_s\right) = x\left(t\right) + v\left(t\right) T_s + \frac{1}{2} a T_s^2 \text{ and} \tag{3.7.2}$$

$$v\left(t + T_s\right) = v\left(t\right) + \frac{a\left(t\right) + a\left(t + T_s\right)}{2} T_s \tag{3.7.3}$$

This will be used to obtain the simulated position and velocity from the acceleration in this thesis.

The validation results for cylinder dynamics model (including the friction model) are shown in Figure 3.7.2. The position in the simulation is very close to the one in the experiment. The error might be due to effect of piston position on the actual friction force. The model's friction coefficients are constants that were averaged over a range of positions.

The validation results for the valve models are shown in Figure 3.7.3. The pressures of chambers A and B in the simulation are close to the experimental values. This demonstrates that the valve models work well when the velocity is not zero (as it was in section 3.6).

The validation results of friction model and valve models together are shown in Figure 3.7.4. Since the positions, velocities and pressures are all predicted, they affect each other in the simulation. From Figure 3.7.4, the predicted position and pressures are close to the experimental data, which demonstrates that both the friction model and valve models are very good.

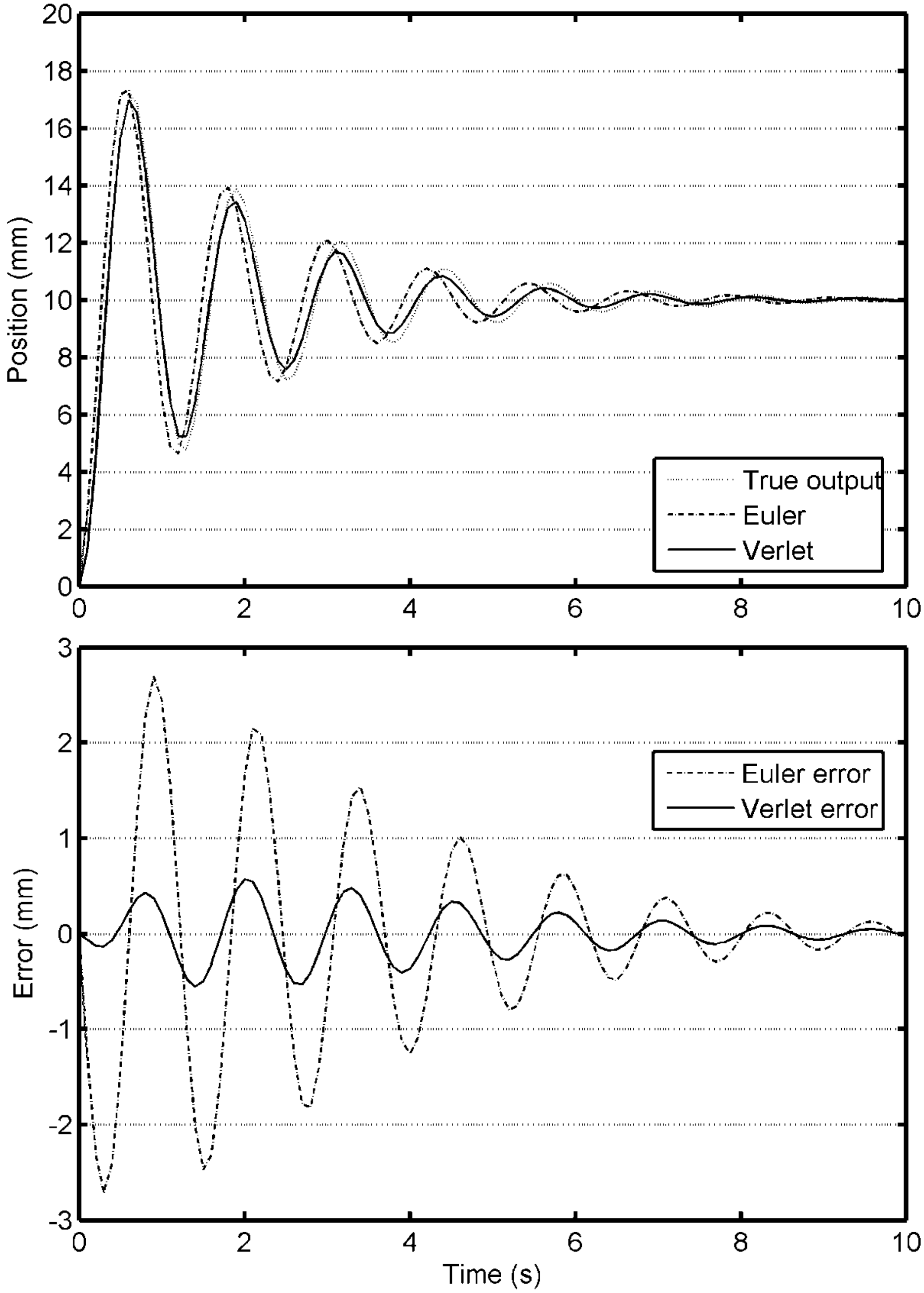

Figure 3.7.1 Comparison of Euler integration and Verlet integration for an underdamped mass-spring-damper system.

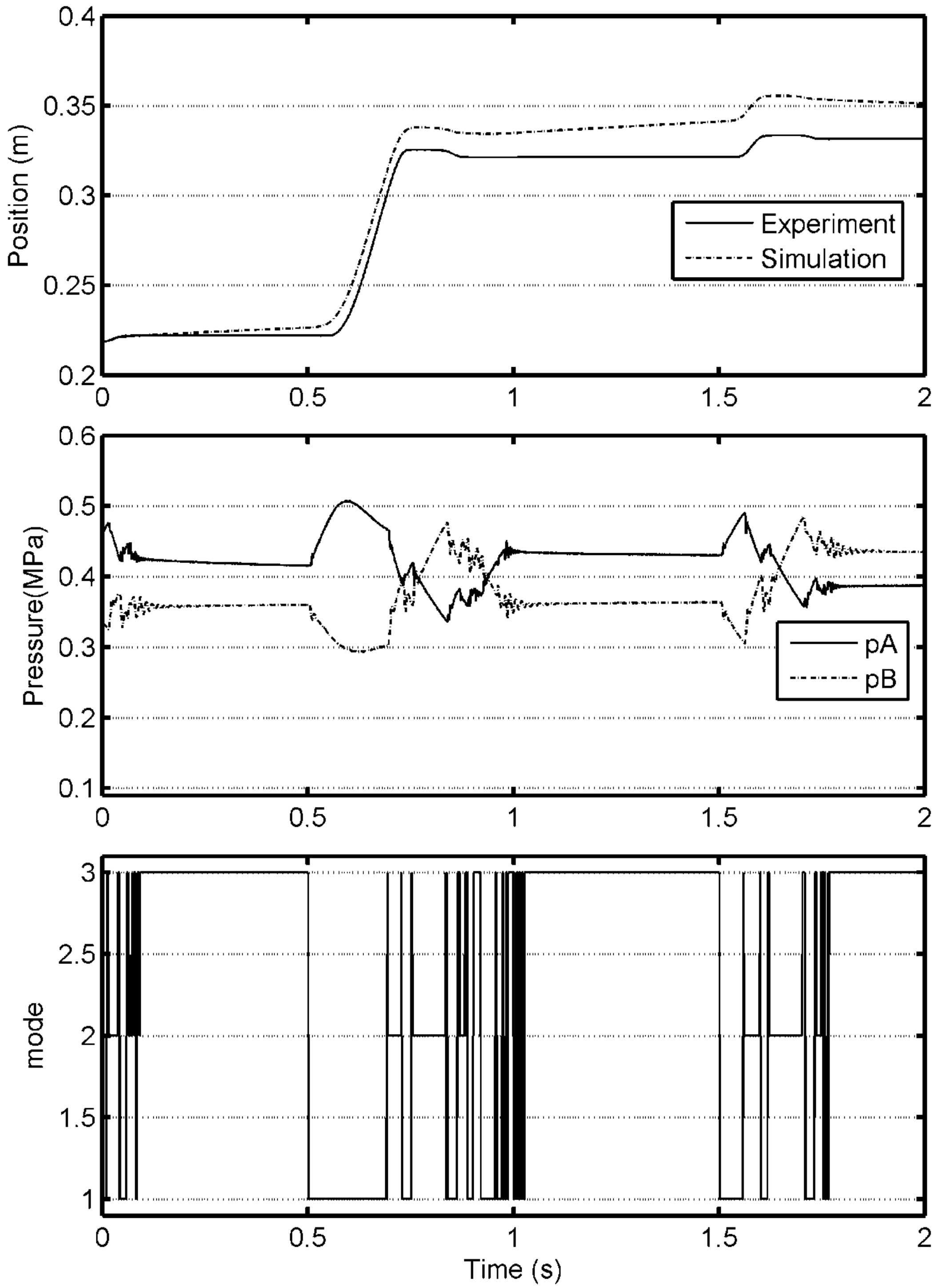

Figure 3.7.2 Comparison of experimental results and cylinder dynamics model simulation results. (Note that the simulated pressures were set equal to the measured pressures.)

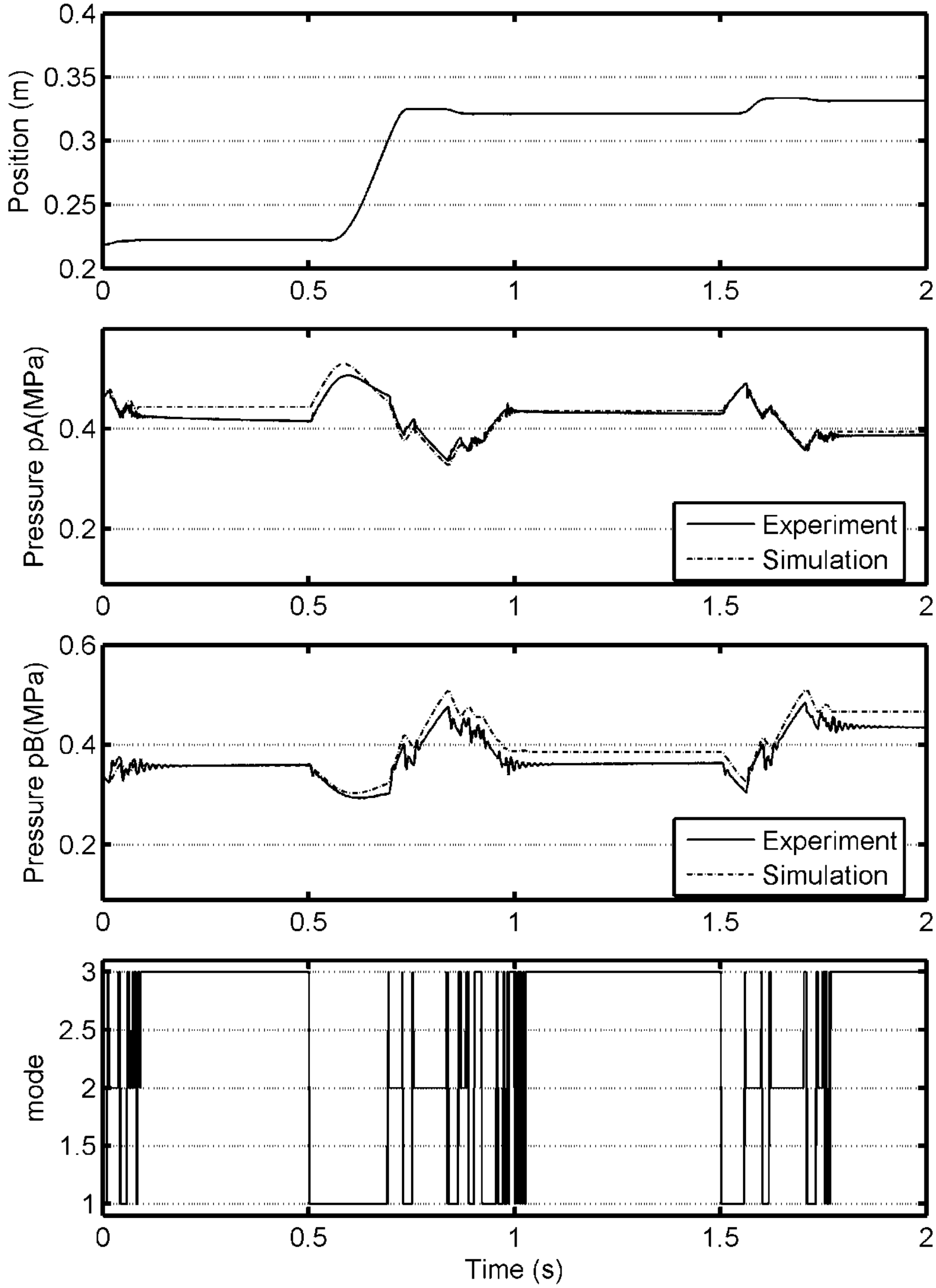

Figure 3.7.3 Comparison of experimental results and valve model simulation results. (Note that the simulated positions and velocities were set equal to the values from the experiments.)

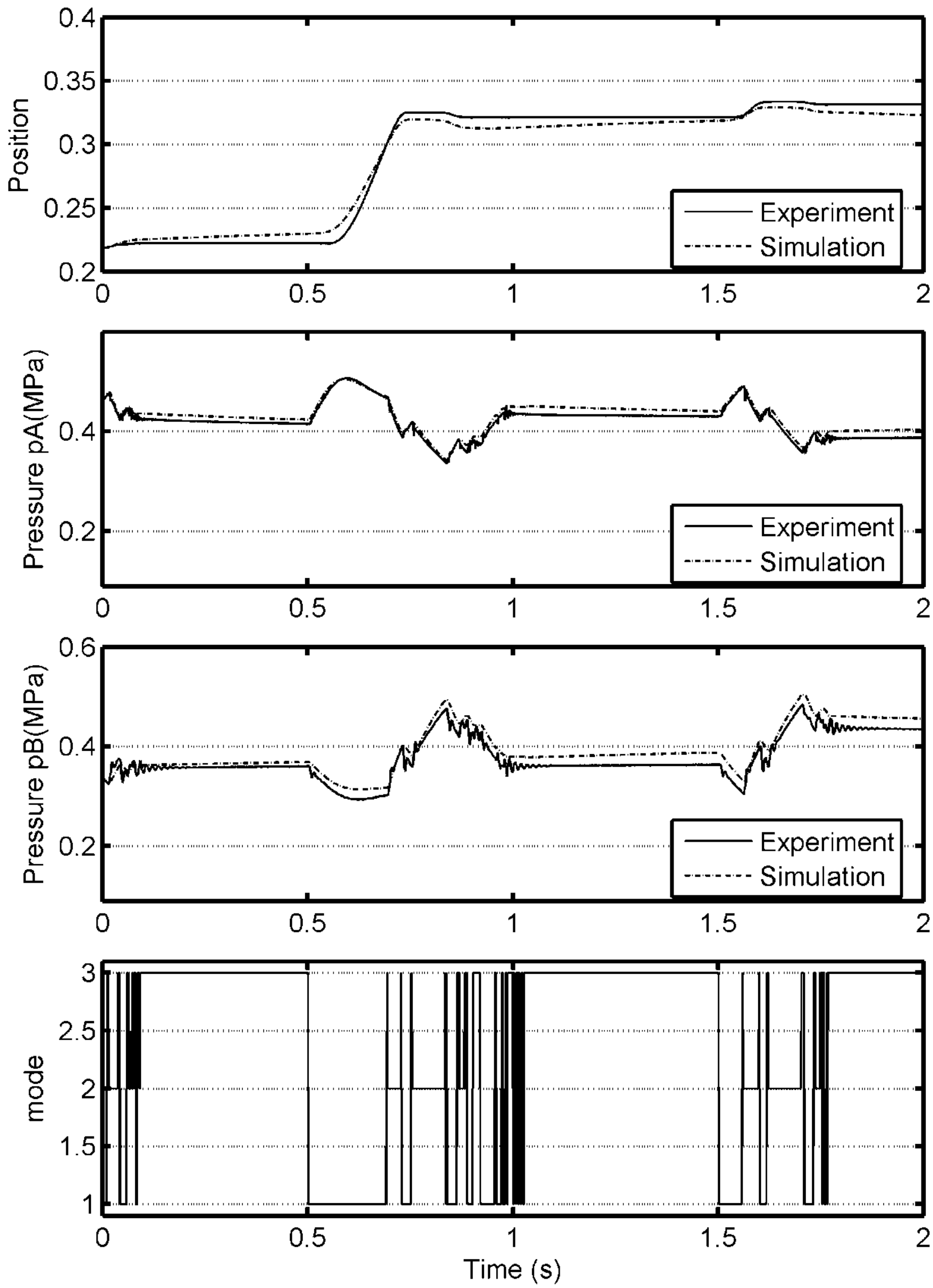

Figure 3.7.4 Comparison of experimental results and system model simulation results.

CHAPTER 4 CONTROLLER DESIGN

4.1 Introduction

In the previous chapter, the system model is derived and validated. In the remainder of this thesis, the designs and performance of two existing SMC algorithms will be compared with three proposed control algorithms. The designs of the five control algorithms will be presented in this chapter. The two existing SMC algorithms constitute the state of the art for directly switching on/off valves without PWM, and are described first. Next, two novel improved versions of those SMC algorithms are proposed. Finally, a novel version of discrete-valued model predictive control is proposed.

4.2 Existing sliding mode control algorithms

4.2.1 Three-mode sliding mode control algorithm

In this section, the three-mode sliding mode controller (abbreviated as SMC3) proposed by Nguyen et al. (2007) is applied to our system model from Chapter 3. Their SMC3 does not use PWM and directly switches the valves. This direct switching is intended to reduce the valve switching frequency and thus prolong the valve life compared with PWM-based methods. The three modes are defined as follows:

Mode 1: both chambers' valves are closed ($u_1 = 0$, $u_2 = 0$, $u_3 = 0$ and $u_4 = 0$);

Mode 2: chamber A charges and chamber B discharges ($u_1 = 1, u_2 = 0, u_3 = 0$ and $u_4 = 1$);

Mode 3: chamber A discharges and chamber B charges ($u_1 = 0, u_2 = 1, u_3 = 1$ and $u_4 = 0$).

Mode 2 is used to move the piston in the positive direction and mode 3 is used to move the piston in the negative direction. Mode 1 is used to reduce the chattering when the tracking error is small enough and to save energy.

In order to apply their method, our friction model (3.5.3) must be highly simplified by neglecting the non-differentiable terms; and assuming $\beta_{p,p} = \beta_{p,n} = \beta_p$ and $C_{v,p} = C_{v,n} = C_v$; yielding

$$F_f = \beta_p \Delta P + C_v \dot{y} \tag{4.2.1}$$

The simplified version of (3.4.16) is then

$$\begin{aligned} M\ddot{y} &= P_a A_a - P_b A_b - F_f \\ &= P_a A_a - P_b A_b - \beta_p \Delta P + F_v \dot{y} \end{aligned} \tag{4.2.2}$$

It is also necessary to rearrange (3.4.12) and (3.4.13) as follows:

$$\dot{P}_a = \frac{KRT\dot{m}_a - KA_a \dot{y} P_a}{A_a y} \text{ and} \tag{4.2.3}$$

$$\dot{P}_b = \frac{KRT\dot{m}_b + KA_b \dot{y} P_b}{A_b (L - y)} \tag{4.2.4}$$

The system dynamics equation for the three discrete modes is obtained by taking the derivative of (4.2.2) with respect to time; and substituting (4.2.3) and (4.2.4) for $\dot{P}_a$ and $\dot{P}_b$, respectively. The result is

$$\dddot{y} = \begin{cases} F(Z), & \text{mode 1} \\ F(Z) + B_2(Z), & \text{mode 2} \\ F(Z) - B_3(Z), & \text{mode 3} \end{cases} \tag{4.2.5}$$

where $Z = \{y, \dot{y}, \ddot{y}, P_a, P_b\}$ is the state vector; and

$$F(Z) = -\frac{KA_a \dot{y} P_a}{A_a y}\left(A_a - \beta_p\right) - \frac{KA_b \dot{y} P_b}{A_b\left(L - y\right)}\left(A_b - \beta_p\right) - F_v \ddot{y}\ , \tag{4.2.6}$$

$$B_2(Z) = \frac{KRT\dot{m}_1}{A_a y}\left(A_a - \beta_p\right) + \frac{KRT\dot{m}_4}{A_b\left(L - y\right)}\left(A_b - \beta_p\right) \text{ and} \tag{4.2.7}$$

$$B_3(Z) = \frac{KRT\dot{m}_2}{A_a y}\left(A_a - \beta_p\right) + \frac{KRT\dot{m}_3}{A_b\left(L - y\right)}\left(A_b - \beta_p\right) \tag{4.2.8}$$

It should be noted that their model and controller equations assumed $\beta_p = 0$.

They define the second-order sliding surface

$$s = \frac{\ddot{e}}{\omega^2} + \frac{2\zeta\dot{e}}{\omega} + e \tag{4.2.9}$$

where $e = y - y_d$ is the position error, y is the actual position, y_d is the desired position, and ζ and ω are constant and positive controller parameters. They use the function s from (4.2.9) and implement the three discrete modes based on three regions as follows

$$\begin{cases} s > \varepsilon, & \text{mode 3} \\ s < -\varepsilon, & \text{mode 2} \\ -\varepsilon \le s \le \varepsilon, & \text{mode 1} \end{cases} \tag{4.2.10}$$

where ε is termed the deadband. It is used to reduce the valve switching caused by control chattering. From a tracking error point of view, it is desirable to choose ε as small as possible. However, ε also needs to be sufficiently large to reduce chattering. This trade-off when choosing ε will be considered in the simulations and experiments.

4.2.2 Seven-mode sliding mode control algorithm

The seven-mode sliding mode controller (abbreviated as SMC7) proposed by Hodgson et al. (2012) will be applied to our model in this section. They extended the SMC3 of Nguyen et al. (2007) to the seven-modes in order to reduce valve switching frequency. The four additional modes are:

chamber A charges and chamber B is closed ($u_1 = 1$, $u_2 = 0$, $u_3 = 0$ and $u_4 = 0$)

chamber A discharges and chamber B is closed ($u_1 = 0$, $u_2 = 1$, $u_3 = 0$ and $u_4 = 0$)

chamber A is closed and chamber A discharges ($u_1 = 0$, $u_2 = 0$, $u_3 = 0$ and $u_4 = 1$)

chamber A is closed and chamber B charges ($u_1 = 0$, $u_2 = 0$, $u_3 = 1$ and $u_4 = 0$)

The seven discrete modes and valve inputs u_1, u_2, u_3 and u_4 are shown in Table 4.2.1. Mode 6 is used to move the piston to the positive direction, and is the same as mode 2 in SMC3. New modes 2 and 4 also provide the positive direction of movement, but the acceleration of those is smaller than that of mode 6. Conversely, mode 7 is used to move the piston to the negative direction, and is the same as mode 3 in SMC3. New modes 3 and 5 also provide the negative direction of movement, but acceleration of those is smaller than that of mode 7. As in SMC3, mode 1 is used to reduce the valve switching when the tracking error is small enough and to save energy.

Same as SMC3, they defined the second-order sliding surface as

$$s = \frac{\ddot{e}}{\omega^2} + \frac{2\zeta\dot{e}}{\omega} + e \tag{4.2.16}$$

They extended the three regions in SMC3 to five regions to reduce switching. In addition to deadband ε in SMC3, they introduce a larger deadband β. The five regions of s and the selected modes are shown in Table 4.2.2.

Table 4.2.1 Seven discrete modes and valve inputs u_1, u_2, u_3 and u_4

	mode 1	mode 2	mode 3	mode 4	mode 5	mode 6	mode 7
u_1	0	1	0	0	0	1	0
u_2	0	0	1	0	0	0	1
u_3	0	0	0	0	1	0	1
u_4	0	0	0	1	0	1	0

Table 4.2.2 Five regions of s and the selected modes

Region	Modes	Pneumatic forces
$s < -\beta$	mode 6	Large positive
$-\beta \leq s \leq -\varepsilon$	mode 2 or mode 4	Small positive
$-\varepsilon \leq s \leq \varepsilon$	mode 1	Zero
$\varepsilon < s \leq \beta$	mode 3 or mode 5	Small negative
$s > \beta$	mode 7	Large negative

The regions $|s| \leq \varepsilon$ and $|s| > \beta$ have unique control modes. The region $-\beta \leq s < -\varepsilon$ or $\varepsilon < s \leq \beta$ has two control modes thus pressure sensors are needed to select control modes.

They first studied the region $-\beta \leq s < -\varepsilon$. For mode 2, chamber A is connected to the supply pressure and chamber B is closed. From the dynamic equation (3.4.16), the piston acceleration is $\ddot{y} \propto P_s - P_b$ if the mode 2 is invoked for a sufficient amount of time. For mode 4, chamber A is closed and chamber B is connected to atmospheric pressure.

The piston acceleration is $\ddot{y} \propto P_a - P_0$ if the mode 4 is invoked for a sufficient amount of time. Based on the above analysis, they defined

$$E_1 = \left(P_s - P_b\right) - \left(P_a - P_0\right) = \left(P_s + P_0\right) - \left(P_a + P_b\right) \tag{4.2.17}$$

If the magnitude of E_1 is larger than zero, mode 2 has a higher pressure difference than mode 4. The piston acceleration of mode 2 is larger than that of mode 4. Thus, mode 2 is used if E_1 is positive. Conversely, mode 4 is used if E_1 is negative.

The next region is $\varepsilon < s \le \beta$. For mode 3, chamber A is connected to the atmosphere pressure and chamber B is closed. From the dynamic equation (3.4.16), the absolute value of piston acceleration is $\ddot{y} \propto P_b - P_0$ if the mode 3 is invoked for a sufficient amount of time. For mode 5, chamber A is closed and chamber B is connected to supply pressure. The absolute value of piston acceleration is $\ddot{y} \propto P_s - P_a$ if the mode 5 is invoked for a sufficient amount of time. Based on the above analysis, we define

$$E_2 = \left(P_s - P_a\right) - \left(P_b - P_0\right) = \left(P_s + P_0\right) - \left(P_a + P_b\right) = E_1 \tag{4.2.18}$$

If the magnitude of E_2 is larger than zero, mode 5 has a higher piston acceleration than mode 3. Thus, mode 5 is used if E_2 is positive. Conversely, mode 3 if E_2 is negative.

In order to reduce switching between the modes used in the region $\varepsilon < |s| \le \beta$, they use a timeout parameter τ to enforcing a minimal amount of mode transitions: mode 2 to mode 4, mode 4 to mode 2, mode 3 to mode 5 and mode 5 to mode 3. A large τ will reduce these mode transitions. but it might cause larger tracking error. Thus, choosing τ

involves a trade-off. The value of τ will be manually tuned in the simulations and experiments.

4.3 Proposed sliding mode control algorithms

4.3.1 Introduction

Adding integral action to a controller can help to reduce steady state error and settling time. In this section, two sliding mode controllers with integral action will be proposed. These controllers are extensions of SMC3 and SMC7 from section 4.2.

4.3.2 Design of sliding mode control with integral action

In order to add integral action, the sliding surface is based on $\int_0^t e\,dt$ rather than e. Thus, we define the sliding surface as

$$s = \frac{\ddot{e}}{\omega^3} + \frac{3\zeta\dot{e}}{\omega^2} + \frac{3\zeta^2 e}{\omega} + \int_0^t e\,dt \tag{4.3.1}$$

where $\int_0^t e\,dt$ is integral action. Integral windup may occur when there is a large change in setpoint and the integral term accumulates a significant error during the rise time, leading to overshoot and a longer settling time. Anti-windup is implemented by bounding the integral action. We limit $\int_0^t e\,dt$ to satisfy

$$\left|\int_0^t e\,dt\right| \le e_{limit} \tag{4.3.2}$$

The bound e_{limit} in (4.3.2) will be manually tuned in the simulations and experiments. We replaced (4.2.9) with (4.3.1) to create a three-mode sliding mode control with integral action algorithm (SMCI3); and replaced (4.2.16) with (4.3.1) to create a seven-mode sliding mode control with integral action algorithm (SMCI7).

4.4 Proposed discrete-valued model predictive control algorithm

4.4.1 Introduction

Model-predictive control (MPC) is an optimization-based nonlinear control strategy. MPC uses the system dynamic model and the current state of the plant to yield an optimal control sequence by minimizing a cost function, and the first control in this sequence then is applied to the plant. The main advantage of MPC is its ability to deal with hard constraints on controls and states. The pneumatic actuator is a highly nonlinear system due to the compressibility of the air and the nonlinearity of the mass flow rate. Model-based controllers are able to stabilize highly nonlinear systems. For our pneumatic system, the discrete modes possible with the four on/off solenoid valves limit the numbers of possible solutions within a finite prediction horizon, making the optimization problem discrete-valued, hence the name discrete-valued MPC (DVMPC). In this section, a DVMPC algorithm, which is an improved version of the algorithm by Bone, Xue and Flett (2015), will be proposed. Then the stability of the proposed algorithm will be analyzed.

4.4.2 Design of discrete-valued model predictive control

The pneumatic actuator has two chambers and four solenoid valves. Each chamber is controlled by two on/off valves independently, thus there are sixteen possible input combinations defined directly from the state of the four on/off valves present in the system. For each chamber, only one valve can be opened at one given time to avoid wasting energy, thus there are nine of input combinations we can use. The corresponding discrete modes are listed in Table 4.4.1. The modes M_1, M_8 and M_9 are functionally similar and are used to reduce valve switching when the tracking error is small enough. The modes M_1, M_8 and M_9 correspond to the two chambers being both closed, both venting and both pressurized, respectively. For all of these three modes, the pressure differences between the two chambers will be similar and thus the acceleration of the piston will be similar. For reasons of safety, it is desirable to keep the chamber pressures close to atmospheric pressure, so we will use M_1 and M_8, and eliminate M_9. With mode M_2, chamber A is pressurized and chamber B is closed. With mode M_4, chamber A is closed and chamber B is depressurized. With mode M_6, chamber A is pressurized and chamber B is depressurized. Therefore in modes M_2, M_4 and M_6, the piston should move in the positive direction. With mode M_3, chamber A is depressurized and chamber B is closed. With mode M_5, chamber A is closed and chamber B is pressurized. With mode M_7, chamber A is depressurized and chamber B is pressurized. Therefore in modes M_3, M_5 and M_7, the piston should move in the negative direction.

Table 4.4.1 Nine discrete modes of four on/off valves

	M_1	M_2	M_3	M_4	M_5	M_6	M_7	M_8	M_9
u_1	0	1	0	0	0	1	0	0	1
u_2	0	0	1	0	0	0	1	1	0
u_3	0	0	0	0	1	0	1	0	1
u_4	0	0	0	1	0	1	0	1	0

The DVMPC control schematic for our system is shown in Figure 4.4.1. At one given time, current states including position y and chamber pressures P_a and P_b are predicted by simulation or measured. DVMPC uses current states and system model to optimize the control sequences in the prediction horizon by minimizing the cost function. The first control in this sequence is applied to either the system (in an experiment) to the model (in a simulation).

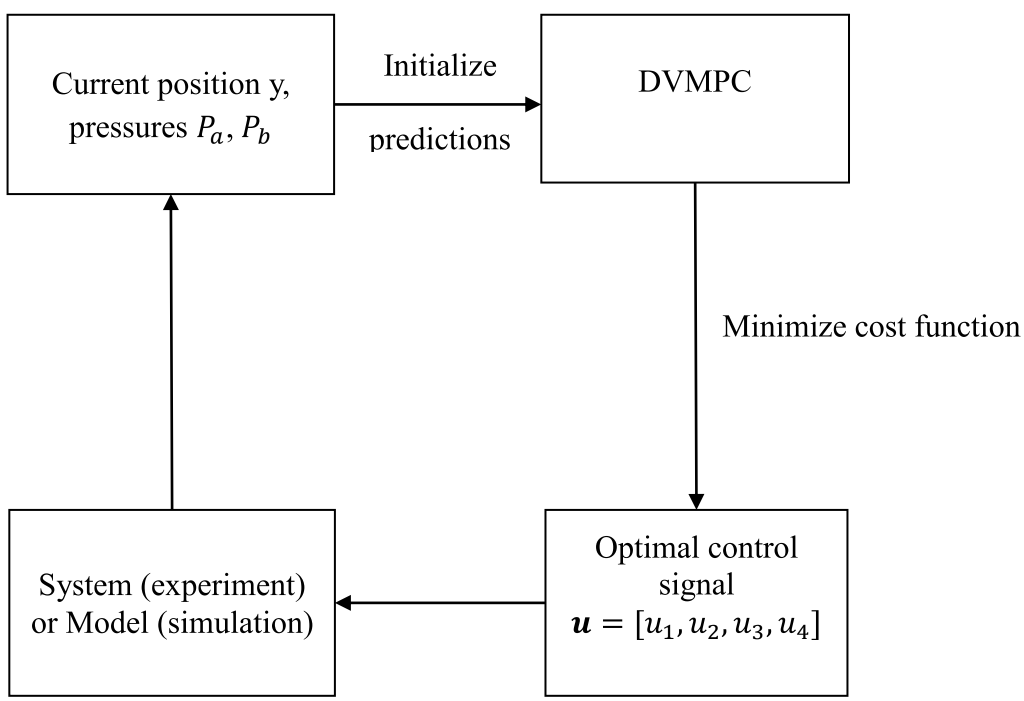

Figure 4.4.1 DVMPC schematic diagram.

For our pneumatic system, the purpose of the control algorithm is to keep the position errors small, during both transient and steady state conditions. The valve switching frequency also should be small to prolong valve life. Finally, high chamber pressures should be avoided for safety. Based on these considerations, the following cost function was designed:

$$\begin{aligned} J &= ITAE + VC + SC + PC \\ &= \sum_{i=1}^{N_p} i \cdot T_s \cdot \left|\hat{y}(t_i) - y_d(t_i)\right| + w_v \cdot \sum_{i=1}^{N_p} \left(\hat{\dot{y}}(t_i) - \dot{y}_d(t_i)\right)^2 \\ &+ w_{du} \cdot \sum_{i=0}^{N_p-1} \left[\sum_{n=1}^{4} \left|\Delta\hat{u}_n(t_i)\right|\right] + w_p \cdot \sum_{i=1}^{N_p} \left[\left(\hat{P}_a(t_i) - P_{a,d}(t_i)\right)^2 + \left(\hat{P}_b(t_i) - P_{b,d}(t_i)\right)^2\right] \end{aligned} \tag{4.4.1}$$

where ITAE stands for integral of time-weighted absolute error; VC stands for velocity cost; SC stands for switching cost; PC stands for pressure cost; N_p is the prediction horizon; $P_{a,d}$ and $P_{b,d}$ are desired chamber pressures; $\hat{P}_a$ and $\hat{P}_b$ are the predicted chamber pressures; $t_i = t_k + i \cdot T_s$ is the future sampling instant; $\Delta\hat{u}_n$ is the predicted change in the n^{th} valve input; w_v, w_{du} and w_p are weighting coefficients; y_d is the desired position; $\hat{y}$ is the predicted position; $\dot{y}_d$ is the desired velocity; and $\hat{\dot{y}}$ is the predicted velocity. $\Delta\hat{u}_n$ is defined as

$$\Delta\hat{u}_n(t_i) = \begin{cases} \hat{u}_n(t_i) - u_n(t_i - T_s) & i = 0 \\ \hat{u}_n(t_i) - \hat{u}_n(t_i - T_s) & 1 \le i < N_p \end{cases} \tag{4.4.2}$$

The following optimization problem is solved every sampling instant:

$$\mathbf{U}_{opt} = \arg \min_{\mathbf{U}} J \tag{4.4.3}$$

subject to:

$$\hat{\mathbf{u}} = \left[\hat{u}_1, \hat{u}_2, \hat{u}_3, \hat{u}_4\right] \in M_i, \quad \forall i = 1, 2, ..., 8, \tag{4.4.4}$$

$$\mathbf{U} = \left[\hat{\mathbf{u}}(t_k), \hat{\mathbf{u}}(t_k + T_s), ..., \hat{\mathbf{u}}\left(t_k + \left(N_p - 1\right)T_s\right)\right] \tag{4.4.5}$$

$$\begin{aligned}&\left[\hat{y}(t_i+T_s),\hat{\dot{y}}(t_i+T_s),\hat{P}_a(t_i+T_s),\hat{P}_b(t_i+T_s)\right]= \\ &f\left(\hat{\mathbf{u}}(t_i),\hat{y}(t_i),\hat{\dot{y}}(t_i),\hat{P}_a(t_i),\hat{P}_b(t_i)\right) \quad \forall i=0,1,\ldots,N_p-1\end{aligned} \quad \text{and} \tag{4.4.6}$$

$$V\left(t_k+N_p\cdot T_s\right)<V\left(t_k\right) \quad \vee \quad V\left(t_k+N_p\cdot T_s\right)<V_{threshold} \tag{4.4.7}$$

where $V=\left(y_d-y\right)^2+d\cdot\left(\dot{y}_d-\dot{y}\right)^2$ is a Lyapunov-like function that is discussed further in section 4.4.3.

The optimal predicted valve input vector $\mathbf{u}\left(t_k\right)$ is obtained by extracting the first four elements of $\mathbf{U}_{opt}$.

The prediction algorithm for solving (4.4.5) is as follows:

1) Set $i=0$.

2) Compute $t_i=t_k+i\cdot T_s$.

3) If $t_i=t_k$ then use:

$$\hat{P}_a\left(t_i\right)=P_a\left(t_k\right)$$

$$\hat{P}_b\left(t_i\right)=P_b\left(t_k\right)$$

$$\hat{y}\left(t_i\right)=y\left(t_k\right)$$

$$\hat{\dot{y}}\left(t_i\right)=\left(y\left(t_k\right)-y\left(t_k-T_s\right)\right)\big/T_s$$

4) If $t_i=t_k+T_s$ then use:

$$\hat{P}_a\left(t_i\right)=\hat{P}_a\left(t_i-T_s\right)+T_s\hat{\dot{P}}_a\left(t_i-T_s\right)$$

$$\hat{P}_b\left(t_i\right)=\hat{P}_b\left(t_i-T_s\right)+T_s\hat{\dot{P}}_b\left(t_i-T_s\right)$$

$$\hat{y}(t_i) = \hat{y}(t_i - T_s) + T_s\hat{\dot{y}}(t_i - T_s) + \frac{1}{2}T_s^2\hat{\ddot{y}}(t_i - T_s)$$

$$\hat{\dot{y}}(t_i) = \hat{\dot{y}}(t_i - T_s) + \frac{1}{2}T_s\left(\hat{\ddot{y}}(t_i - T_s) + \ddot{y}(t_i - 2T_s)\right)$$

5) If $t_i > t + T_s$ then use:

$$\hat{P}_a(t_i) = \hat{P}_a(t_i - T_s) + T_s\hat{\dot{P}}_a(t_i - T_s)$$

$$\hat{P}_b(t_i) = \hat{P}_b(t_i - T_s) + T_s\hat{\dot{P}}_b(t_i - T_s)$$

$$\hat{y}(t_i) = \hat{y}(t_i - T_s) + T_s\hat{\dot{y}}(t_i - T_s) + \frac{1}{2}T_s^2\hat{\ddot{y}}(t_i - T_s)$$

$$\hat{\dot{y}}(t_i) = \hat{\dot{y}}(t_i - T_s) + \frac{1}{2}T_s\left(\hat{\ddot{y}}(t_i - T_s) + \hat{\ddot{y}}(t_i - 2T_s)\right)$$

6) Compute the predicted mass flow rate using:

$$\hat{\dot{m}}_a(t_i) = \hat{\dot{m}}_1\left(\hat{P}_a(t_i), \hat{u}_1(t_i)\right) - \hat{\dot{m}}_2\left(\hat{P}_a(t_i), \hat{u}_2(t_i)\right)$$

$$\hat{\dot{m}}_b(t_i) = \hat{\dot{m}}_3\left(\hat{P}_b(t_i), \hat{u}_3(t_i)\right) - \hat{\dot{m}}_4\left(\hat{P}_b(t_i), \hat{u}_4(t_i)\right)$$

7) Compute the predicted pressure derivatives using:

$$\hat{\dot{P}}_a(t_i) = \frac{KA_a\hat{\dot{y}}(t_i)\hat{P}_a(t_i) - KRT\hat{\dot{m}}_a(t_i)}{A_a\hat{y}(t_i)}$$

$$\hat{\dot{P}}_b(t_i) = \frac{-KA_b\hat{\dot{y}}(t_i)\hat{P}_b(t_i) - KRT\hat{\dot{m}}_b(t_i)}{A_b\left(L - \hat{y}(t_i)\right)}$$

8) Substitute $\hat{P}_a(t_i)$ and $\hat{P}_b(t_i)$ into (3.3.18) to obtain the predicted pneumatic force $\hat{F}_p(t_i)$.

9) Compute the predicted acceleration $\hat{\ddot{y}}(t_i)$ using (3.6.1).

10) Set $i = i + 1$.

11) If $i < N_p$ then go to Step 2.

12) Stop.

The optimization problem (4.4.3)-(4.4.7) is known as an integer nonlinear program. We use an open-source C++ software called Nonlinear Optimization by Mesh Adaptive Direct Search (NOMAD) to solve it. NOMAD is designed to efficiently solve nonlinear constrained optimization problems. Based on timed runs, for reasonably small values of N_p it is possible to solve (4.4.3) in real-time using NOMAD and the PC-based data acquisition and control system described in section 3.3.

4.4.3 Stability of the DVMPC algorithm

In this section, we will discuss how stability of DVMPC is guaranteed by design for the nominal case (*i.e.,* when the model matches the plant). In the previous section we defined the Lyapunov-like function:

$$V = \left(y_d - y\right)^2 + d \cdot \left(\dot{y}_d - \dot{y}\right)^2 \tag{4.4.8}$$

where d is positive weighting coefficient. Only the errors of position and velocity are included in the Lyapunov-like function V. The chamber pressures are not included in V since DVMPC's goal is to produce stable position control, and leaving out the pressures gives DVMPC more freedom to improve the position control. The pressures are already bounded by P_0 and P_s. The stability guarantee comes from the constraint (4.4.7). It includes two inequalities. The first inequality, $V\left(t_k + N_p \cdot T_s\right) < V\left(t_k\right)$, will be satisfied if V decreases over the prediction horizon which implies that the position and velocity errors are decreasing at every sampling instant. If this inequality always held then those errors would decrease to zero. Unfortunately, it will not always hold due to the control signal being discrete-valued and the finite prediction horizon. As mentioned by Grancharova and Johansen (2011), steady state errors or limit cycles can occur with this type of system. For these reasons it was necessary to include the second inequality, $V\left(t_k + N_p \cdot T_s\right) < V_{threshold}$, in (4.4.7). This inequality is similar to (2.3.2) except that we have included the velocity errors. Inclusion of the velocity errors in V prevents DVMPC from returning a solution that may produce high frequency velocity oscillations in the plant. This inequality guarantees that the position and velocity errors are bounded for the nominal case. Specifically, the error vector $\left[e \quad \dot{e}\right]^T$ is forced inside an ellipse that is centred at the origin. The dimensions of the ellipse are determined by the choices of $V_{threshold}$ and *d*. As with the choice of δ in Grancharova and Johansen (2011), the choice of $V_{threshold}$ involves a trade-off between the feasibility and stability of DVMPC.

4.5 Summary

In this chapter, three control algorithms for the pneumatic servo system were proposed. First, two state-of-the-art SMC algorithms were described for comparison purposes. Then, two novel improved versions of those SMC algorithms were proposed to reduce the steady state error and valve switching frequency. Next, a novel discrete-valued model predictive control was presented. The stability of the proposed algorithm was analyzed. In the next two chapters, these controllers will be compared using simulations and experiments.

CHAPTER 5 SIMULATIONS

5.1 Introduction

In the previous chapter, five nonlinear controllers were designed. In this chapter, computer simulations will be used to study their performance. First, the desired trajectory and performance metrics are described. Next, the controllers are simulated and compared for the HFC. Robustness to payload mass mismatch with the HFC is also simulated and discussed. Finally, simulation results for a single rod low friction cylinder are presented and discussed to show how well that the controllers perform with a different type of cylinder.

5.2 Simulation settings

5.2.1 Introduction

In the simulations, the HFC parameters for the nominal plant are the same as presented in chapter 3. The supply pressure was set to 0.6 MPa. The nominal moving mass is 2.14 kg. In software, the sampling frequency was set at 1 kHz for all the controllers. The desired trajectory, performance metrics and ZOH will be described in this section.

5.2.2 Trajectory selection

The controller should work well under dynamic and steady state conditions. A multi-step desired position trajectory will be used to test and compare the dynamic and steady state performance of the five controllers. Figure 5.2.1 shows the desired trajectory where the setpoint is varied from near fully retracted (222 mm), to near fully extended (422 mm), back to near fully retracted (222 mm), to mid-stroke (322 mm), then to (332 mm). The largest size of step tests is 200 mm. The smallest size is 10 mm. The total duration is 4 s. The desired velocity and acceleration are set equal to zero (*i.e.*, the discontinuities at the step changes are ignored).

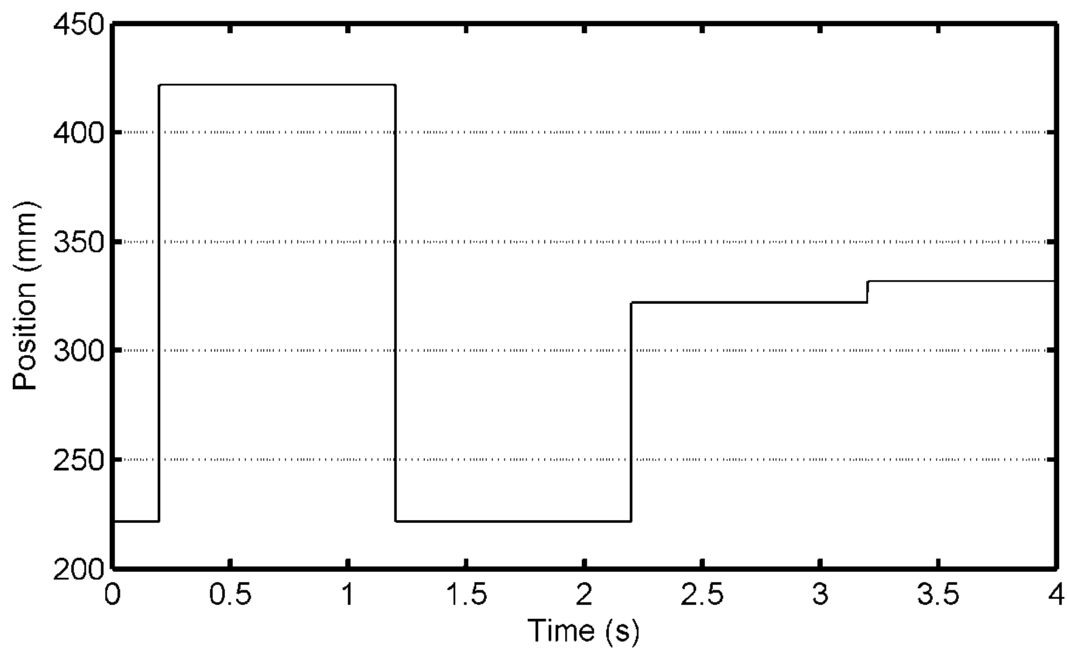

Figure 5.2.1 Multi-step trajectory

5.2.3 Performance metrics

Performance metrics will be used to make quantitative comparisons of the controller performances in simulations and experiments. We define the performance metrics as follows:

Root Mean Square Error (RMSE) provides a measure of the differences between the desired position and the actual position and is given by

$$RMSE = \sqrt{\frac{1}{n}\sum_{k=1}^{n}\left(y\left(t_k\right)-y_d\left(t_k\right)\right)^2}$$

where n is the number of points.

Steady State Error (SSE) is used to quantize the steady state performance. SSE is calculated as the maximum absolute value of the error when the response is judged to be at steady state. One problem is that the response may not reach the perfect steady state condition of zero velocity so another approach had to be used to judge it. Based on observations of the results, the errors from 0.6 s to 1 s after each step change may be approximated as being at steady state. This time window was used to obtain the SSE unless the settling time exceeded 0.6 s. In those situations, the errors from 0.8 s to 1 s after the step were used. Since the desired trajectory is multi-step trajectory, the SSEs for the four steps will be reported separately. These are named SSE_1, SSE_2, SSE_3 and SSE_4, respectively. The average steady state error (SSE) of all four steps will be also reported.

Settling time (t_s) is defined in this thesis as the time required for the response to settle within 1 mm of its steady state and stay there. Traditionally, settling time is defined as "the time required for the response curve to reach and stay with a range of certain percentage (usually 5% or 2%) of the final value" (Tay, Mareel and Moore, 1997). This traditional definition was not used since it gave widely varying results for different step sizes. The likely reason is that the errors appeared to be uncorrelated with the step size. Since the desired trajectory has multiple steps with different sizes, we use an absolute error threshold rather than a relative (*i.e.*, percentage) threshold. The settling times for the four steps; named t_{s1}, t_{s2}, t_{s3} and t_{s4}, respectively; will be reported. The average settling time (t_s) of all four steps will be also reported.

Overshoot (OS) is the height of the maximum (peak) position relative to the steady state value of the position. We use overshoot in mm rather than in percent since percentage works for linear systems and our pneumatic system is a nonlinear system. The overshoots for the four steps; named OS_1, OS_2, OS_3 and OS_4, respectively; will be reported. The average overshoot (OS) of all the four steps will be also reported.

Switches Per Second (SPS) reflects the aggregated occurrence of switches in all four solenoid valves. SPS is defined as the average number of switches per second per valve.

For pneumatic systems, the best controller should have small RMSE, SSE, t_s, OS and SPS. However, trade-offs exist with these performance metrics. It is difficult to reduce all of them at the same time. For example, a smaller SPS might result in larger SSE. The controller and its parameters, along with the plant, determine the values of these performance metrics.

5.2.4 Zero-order hold

The valves need time to energize and de-energize when they receive control signals thus they need time to fully open or fully close. The switch on delay of MAC valve is about 4 ms and switch off delay is about 2 ms. The sampling period T_s in data acquisition is 1 ms, less than the switch on/off delay time. If the period of the valve input is 1 ms, the valve switching frequency would tend to be large and the valve's lifespan would be reduced. To prevent excessive valve switching a ZOH may be used to keep the valve input constant for a certain period. The same method was used by Bone, Xue and Flett. (2015). They chose ZOH to be 5 ms to ensure that each valves state (on/off) agreed with value of the valve at the end of each ZOH period since 5 ms is greater than the on and off delays. With a larger value of ZOH, the computer will have longer time to calculate the valve inputs, but the computational delay will be also larger. In the simulation, we tried ZOH periods of 5 ms, 10 ms and 20 ms to compare their performance and to select the best one for the experiments.

5.3 Sliding mode controllers without zero-order hold

The four sliding mode controllers (SMC3, SMC7, SMCI3 and SMCI7) were simulated for the HFC with the multi-step trajectory. The controller parameters were manually tuned based on the nominal case (i.e., model equals plant). The goals of tuning the controller parameters were to reduce the tracking errors and valve switch frequency. Since the definitions of the sliding surface are different between SMC and SMCI, the choice of controller parameters for SMC and SMCI are different. The tuned sliding surface parameters for SMC are: $\omega_{SMC} = 40$ rad/s , $\zeta_{SMC} = 0.6$ and $\varepsilon_{SMC} = 0.5\ mm$. For SMC7, the additional deadband is $\beta_{SMC} = 2\ mm$ and the timeout is $\tau_{SMC} = 10\ ms$. The tuned sliding surface parameters for SMCI3 are: $\omega_{SMCI} = 5$ rad/s , $\zeta_{SMCI} = 5$ and $\varepsilon_{SMCI} = 5\ mm$. For the SMCI7, the additional deadband is $\beta_{SMCI} = 20\ mm$ and the timeout is $\tau_{SMC} = 10\ ms$. The cut-off frequency of low-pass filter is 50 Hz. Figures 5.3.1 - 5.3.4 show the results of the four SMC controllers without ZOH plotted vs. time.

The performance metrics for the four SMC controllers are compared in Table 5.3.1. The SSE, t_s and OS values are the averages of results from the four steps. The SPS with SMC7 is reduced by 44% compared to SMC3, and that of SMCI7 is reduced by 63% compared to SMCI3. This demonstrates that the additional four modes helped to lower the valve switching frequency. The SSE values of four steps and average values are shown in Table 5.3.2. SMC7 and SMCI7 have smaller SSE values than SMC3 and SMCI3. The t_s and OS values are shown in Tables 5.3.3 and 5.3.4, respectively. The OS of SMCI3 is reduced by 91% compared to SMC3, and the OS of SMCI7 is reduced by 93% compared to SMC7. Adding integral action to the SMC algorithms sliding mode controller was clearly able to reduce the OS. Due to the smaller OS, SMCI3 and SMCI7 have smaller t_s than SMC3 and SMC7. Compared with SMC3, the t_s of SMCI7 is reduced by 22%. Considering the values of SPS, SSE, settling time and overshoot, SMC7 and SMCI7 are better than SMC3 and SMCI3. Thus, we will study the effects of ZOH for only SMC7 and SMCI7 in the next subsection.

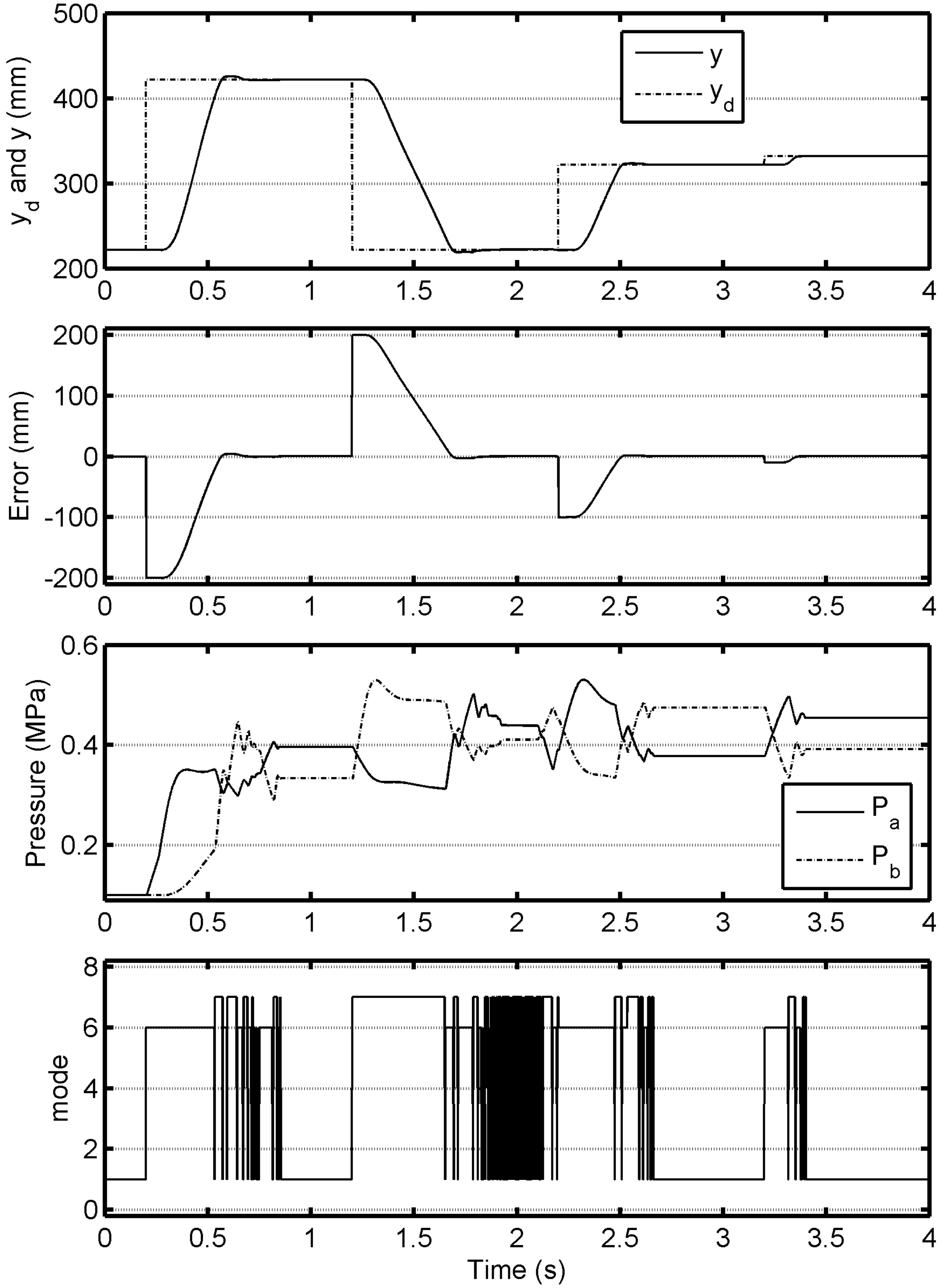

Figure 5.3.1 Simulation of HFC with SMC3, without ZOH and with *M*=2.14 kg

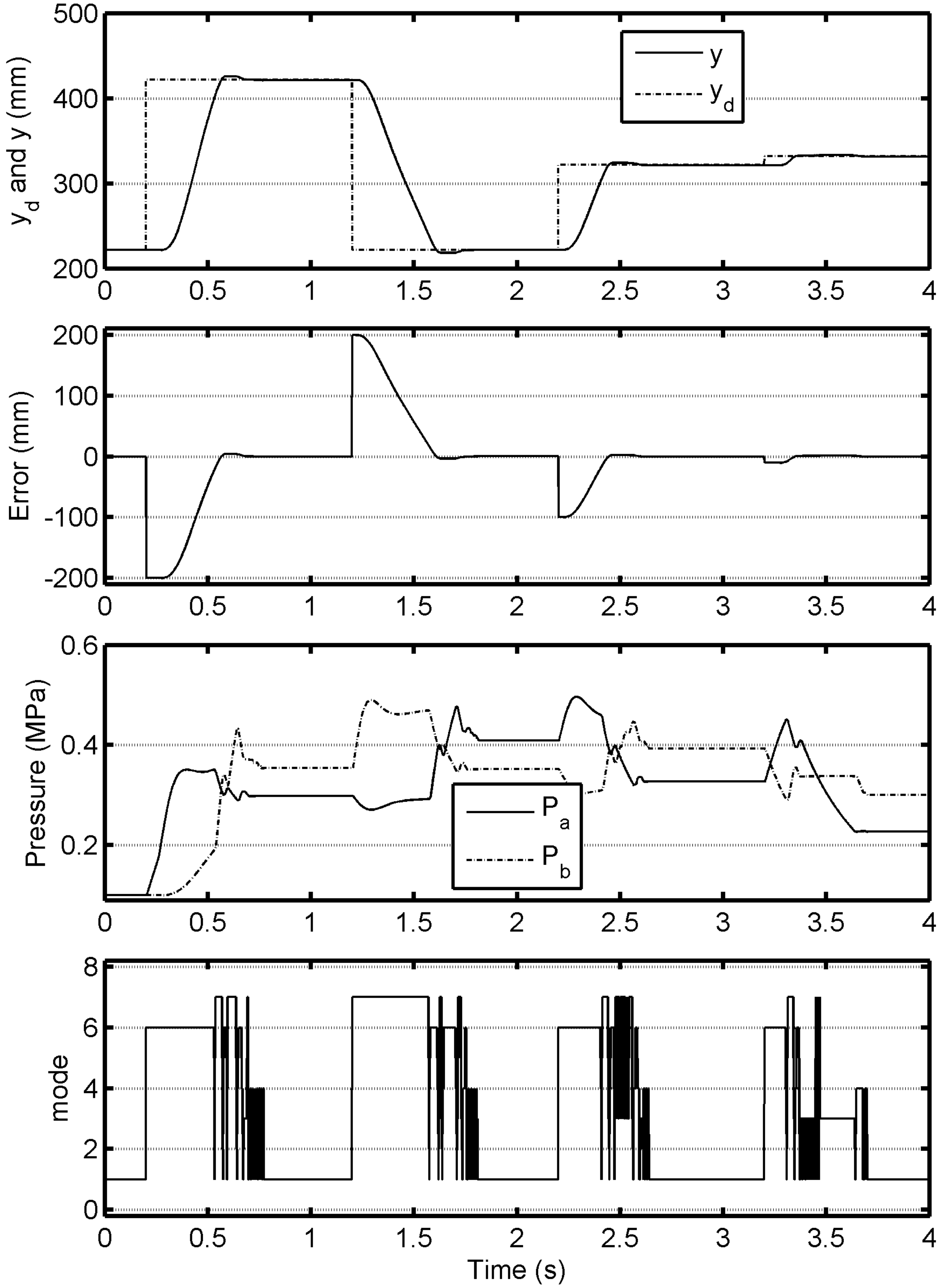

Figure 5.3.2 Simulation of HFC with SMC7, without ZOH and with M=2.14 kg

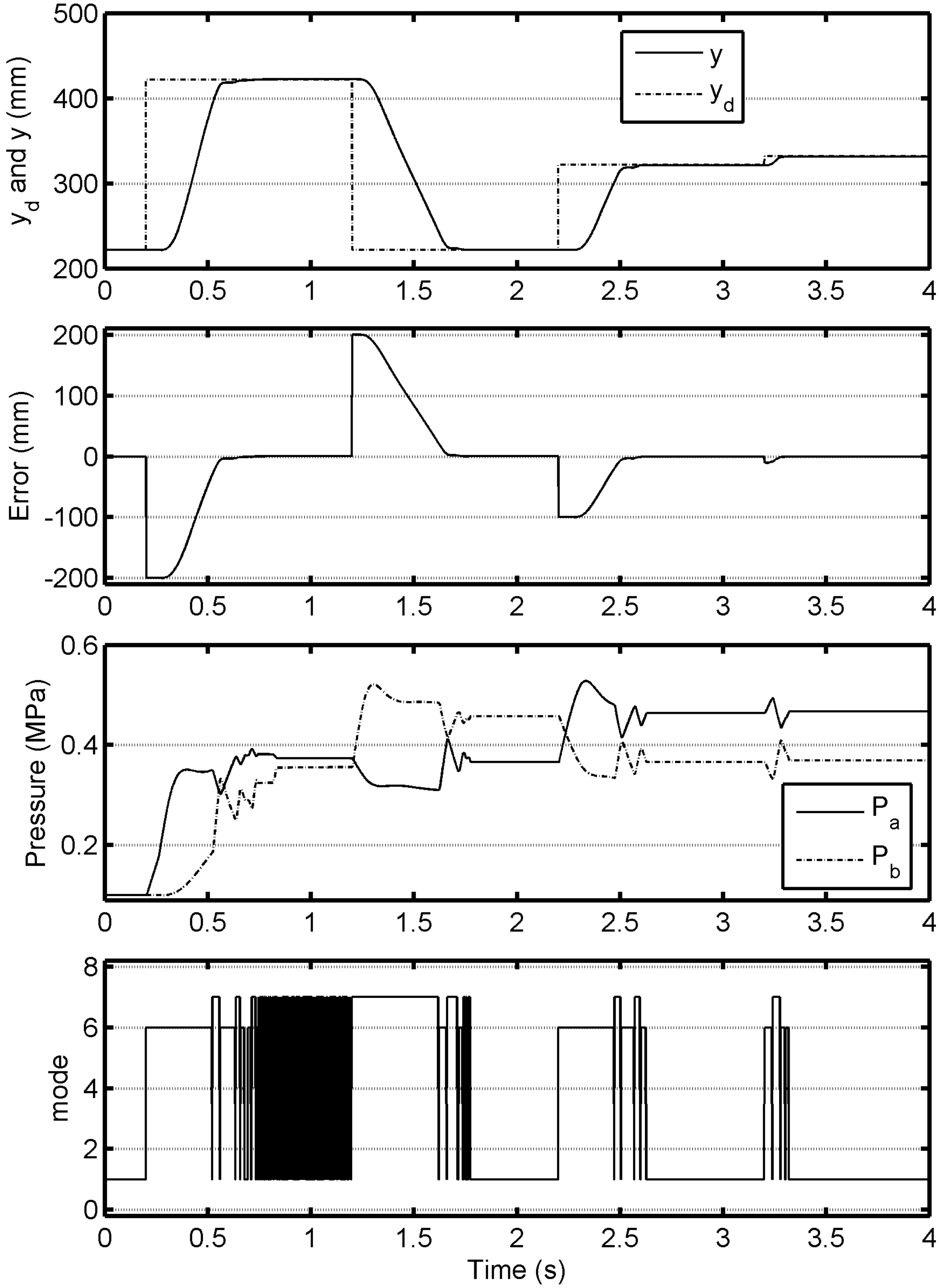

Figure 5.3.3 Simulation of HFC with SMCI3, without ZOH and with *M*=2.14 kg

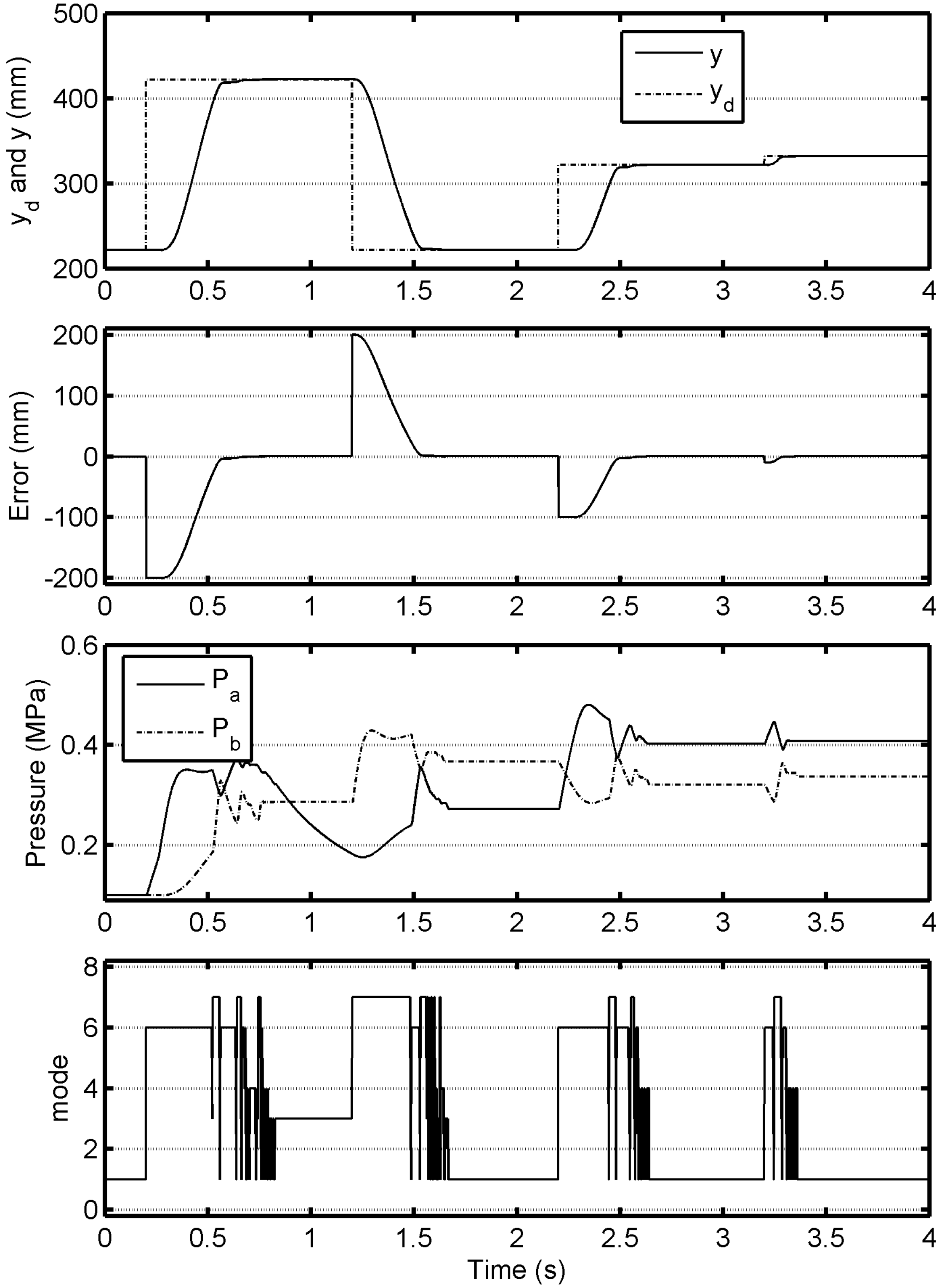

Figure 5.3.4 Simulation of HFC with SMCI7, without ZOH and with M=2.14 kg

Table 5.3.1 Comparisons of performance metrics for SMC controllers without ZOH in simulation.

Controller	RMSE (mm)	SPS	SSE (mm)	t_s (s)	OS (mm)
SMC3	68.69	24.50	0.36	0.41	2.1
SMC7	63.69	13.63	0.33	0.46	2.8
SMCI3	67.53	28.25	0.42	0.36	0.18
SMCI7	62.13	10.50	0.19	0.32	0.18

Table 5.3.2 Comparisons of SSE values (mm) for SMC controllers without ZOH in simulation.

Controller	SSE_1	SSE_2	SSE_3	SSE_4	SSE
SMC3	0.07	0.88	0.11	0.37	0.36
SMC7	0.32	0.18	0.38	0.45	0.33
SMCI3	0.73	0.16	0.40	0.40	0.42
SMCI7	0.66	0.04	0.01	0.05	0.19

Table 5.3.3 Comparisons of t_s values (s) for SMC controllers without ZOH in simulation.

Controller	t_{s1}	t_{s2}	t_{s3}	t_{s4}	t_s
SMC3	0.47	0.61	0.42	0.15	0.41
SMC7	0.47	0.53	0.38	0.44	0.46
SMCI3	0.46	0.53	0.39	0.08	0.36
SMCI7	0.46	0.39	0.37	0.08	0.32

Table 5.3.4 Comparisons of OS values (mm) for SMC controllers without ZOH in simulation.

Controller	OS_1	OS_2	OS_3	OS_4	OS
SMC3	3.64	2.73	1.66	0.37	2.1
SMC7	4.11	3.44	2.52	1.13	2.8
SMCI3	0.74	0	0	0	0.18
SMCI7	0.66	0	0.01	0.05	0.18

5.4 Seven-mode sliding mode controllers with zero-order hold

In the previous subsection, four sliding mode controllers without ZOH were compared. The results of SMC7 and SMCI7 were better than those of SMC3 and SMCI3. In section 5.2.3, we stated that using a ZOH with the valve inputs can help reduce the valve's switching frequency. In this section, we will study SMC7 and SMCI7 with ZOH.

SMC7 and SMCI7 were simulated with multi-step trajectory using ZOH =5 ms and ZOH =10 ms, respectively. Other controller parameters are the same as section 5.3. Figures 5.4.1 - 5.4.4 show the results plotted vs. time. The performance metrics are compared in Tables 5.4.1- 5.4.4. From Table 5.4.1 and Table 5.3.1, SPS of SMCI7 is reduced by 46% on average due to the addition of ZOH. For both SMC7 and SMCI7, SPS is similar with ZOH=5 ms and ZOH=10 ms. From Table 5.5.1 and Figures 5.5.1 - 5.5.2, the error does not settle within 1 mm of its steady-state in 1 *s* using SMC7 with ZOH=5 ms and ZOH=10 ms. The OS of SMC7 with ZOH=10 ms is also almost twice that of SMC7 with ZOH=5 ms. From Table 5.5.1 and Figures 5.5.3 - 5.5.4, the system settles within 1 mm of its steady-state in 1 *s* using SMCI7 with ZOH=5 ms but does not when using SMCI7 with ZOH=10 ms. Overshoot of SMCI7 with ZOH=10 ms is almost four times that of SMCI7 with ZOH=5 ms.

Comparing the results of SMC7 with those of SMCI7, we can find that SPS of SMCI7 is 36% smaller on average than that of SMC7 with different values of ZOH. The overshoot of SMCI7 is much smaller than that of SMC7. For example, the overshoot of SMCI7 is 83% smaller than that of SMC7 with ZOH =5 ms. Thus, the SMCI7 with

ZOH=5 ms gives better tracking results than SMC7. The 5 ms and 10 ms values of ZOH helped the controller reduce the valve switching frequency.

Table 5.4.1 Comparisons of performance metrics for SMC controllers with ZOH in simulation.

Controller	ZOH (ms)	RMSE (mm)	SPS	SSE (mm)	t_s (s)	OS (mm)
SMC7	5	63.28	9.38	0.76	N/A	4.14
SMC7	10	61.25	8.50	0.88	N/A	7.74
SMCI7	5	62.98	5.13	0.35	0.32	0.34
SMCI7	10	64.92	6.25	0.67	N/A	1.29

Table 5.4.2 Comparisons of SSE values (mm) for SMC controllers with ZOH in simulation.

Controller	ZOH (ms)	SSE_1	SSE_2	SSE_3	SSE_4	SSE
SMC7	5	1.04	0.37	0.84	0.79	0.76
SMC7	10	0.72	0.96	1.18	0.69	0.88
SMCI7	5	0.55	0.06	0.32	0.46	0.35
SMCI7	10	0.12	0.54	1.25	0.75	0.67

Table 5.4.3 Comparisons of t_s values (s) for SMC controllers with ZOH in simulation.

Controller	ZOH (ms)	t_{s1}	t_{s2}	t_{s3}	t_{s4}	t_s
SMC7	5	N/A	0.49	0.36	0.60	N/A
SMC7	10	0.63	0.65	N/A	0.53	N/A
SMCI7	5	0.46	0.36	0.36	0.09	0.32
SMCI7	10	0.37	0.44	N/A	0.23	N/A

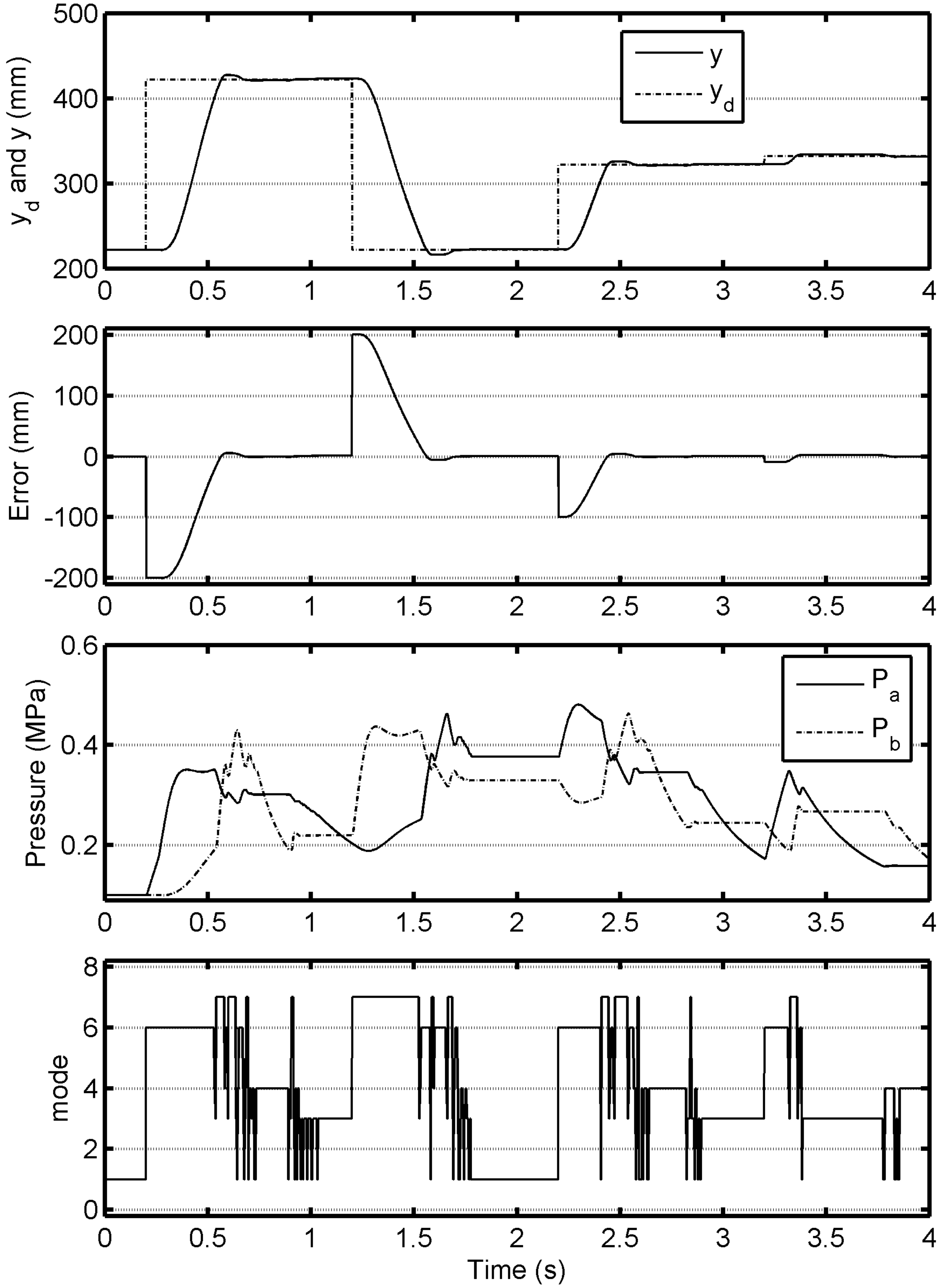

Figure 5.4.1 Simulation of HFC with SMC7, ZOH=5 ms and M=2.14 kg

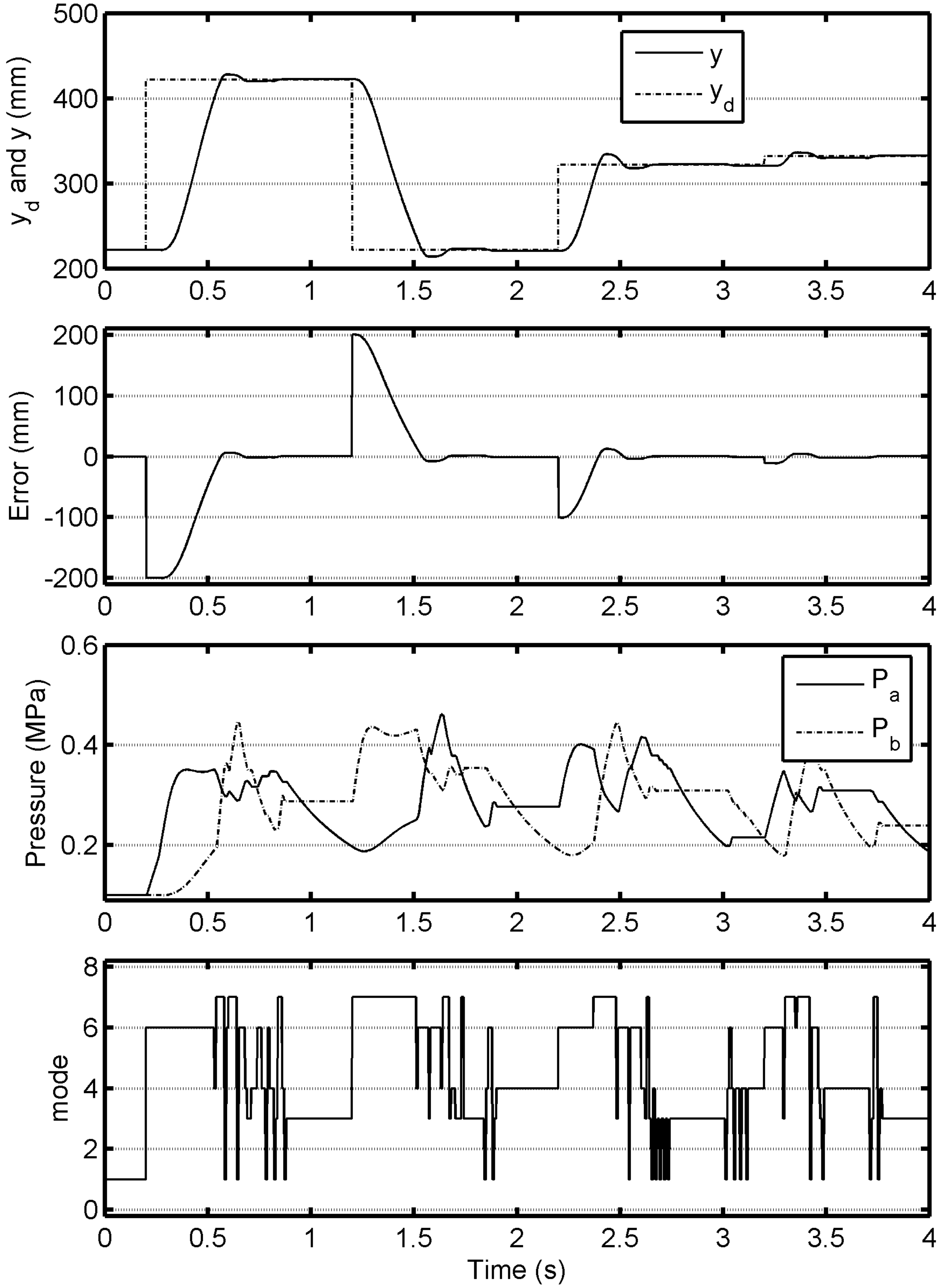

Figure 5.4.2 Simulation of HFC with SMC7, ZOH=10 ms and *M*=2.14 kg

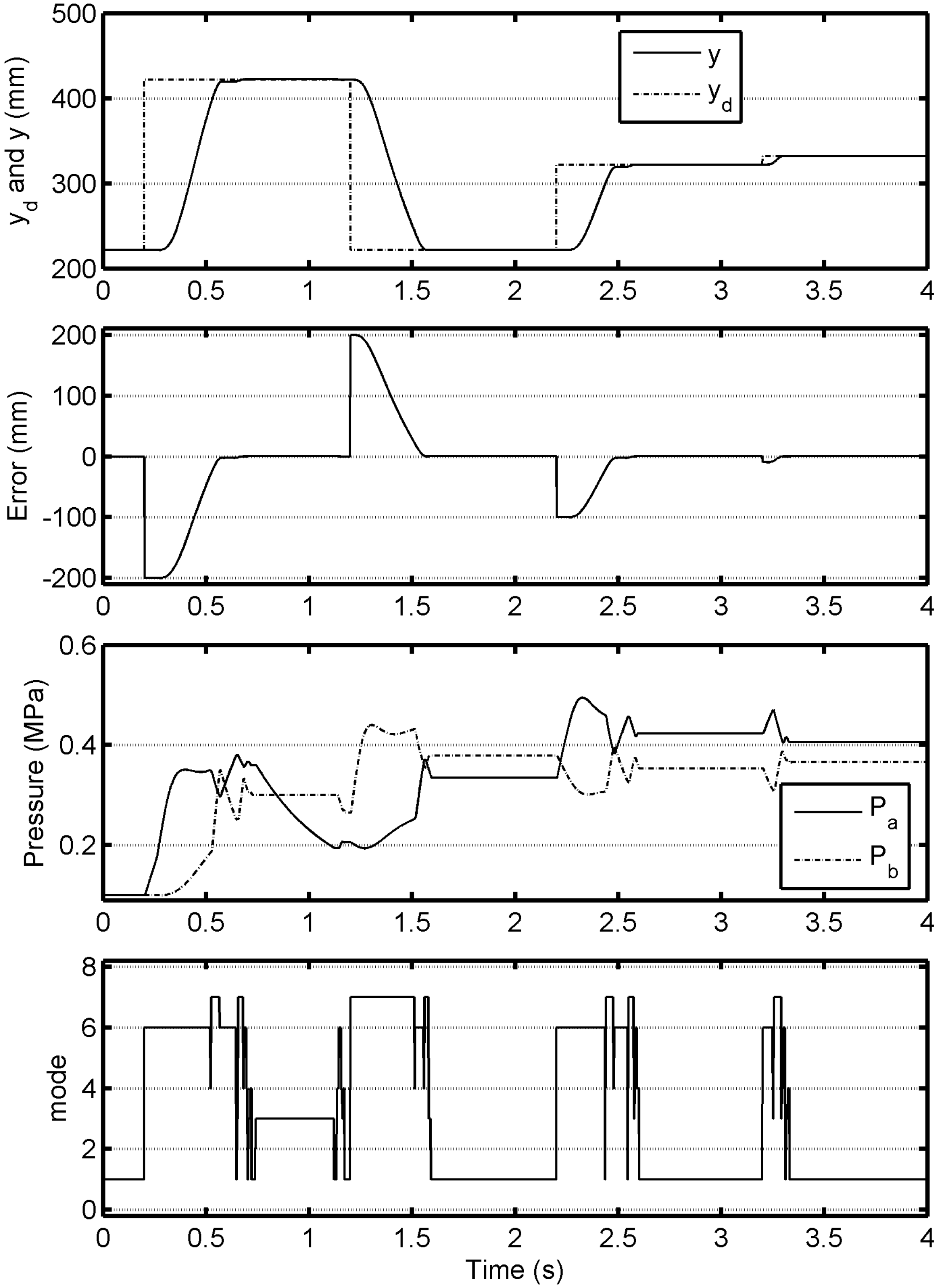

Figure 5.4.3 Simulation of HFC with SMCI7, ZOH=5 ms and M=2.14 kg

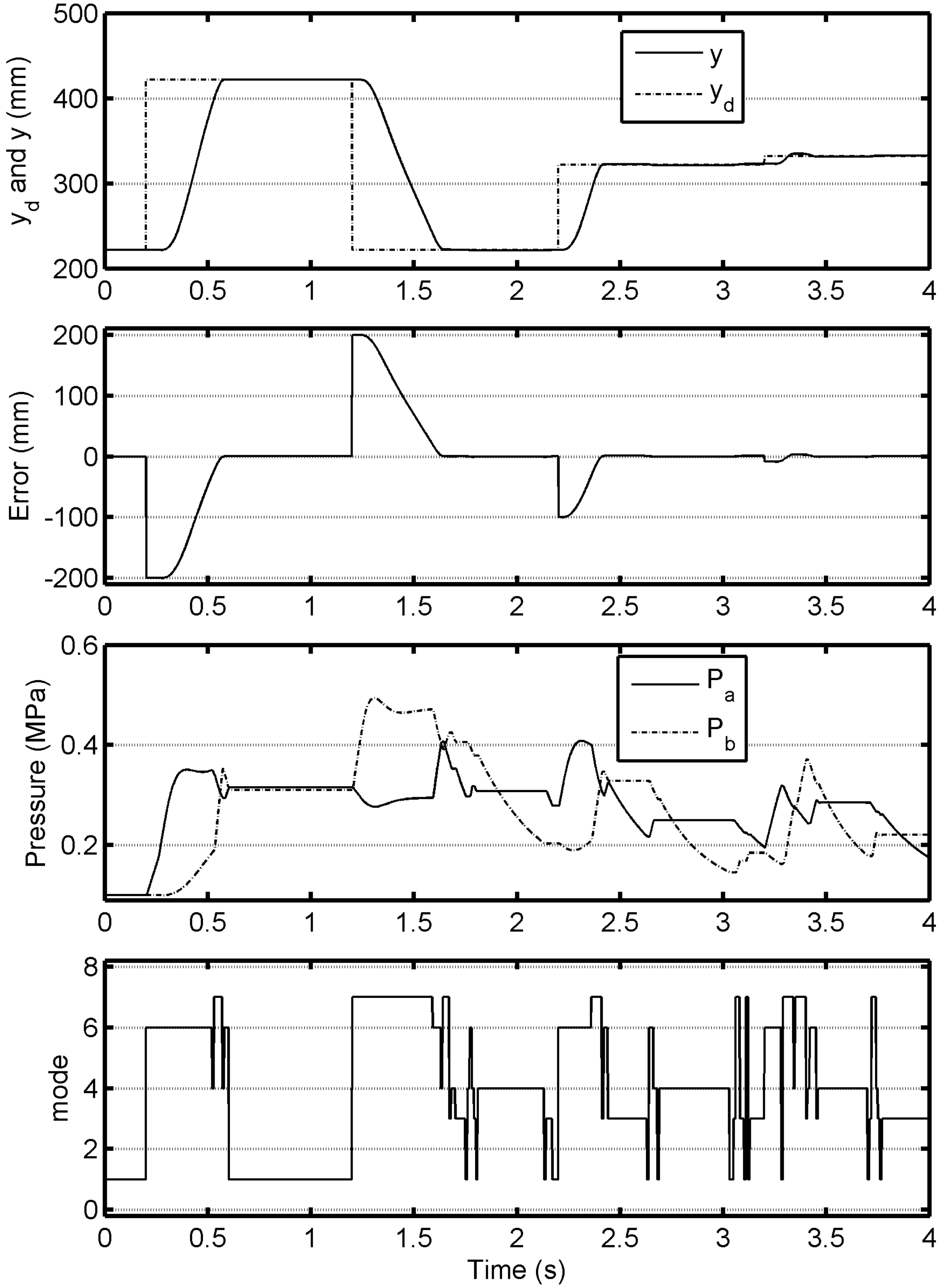

Figure 5.4.4 Simulation of HFC with SMCI7, ZOH=10 ms and *M*=2.14 kg

Table 5.4.4 Comparisons of OS values (mm) for SMC controllers with ZOH in simulation.

Controller	ZOH (ms)	OS_1	OS_2	OS_3	OS_4	OS
SMC7	5	5.53	5.42	3.65	1.97	4.14
SMC7	10	6.18	7.87	12.59	4.30	7.74
SMCI7	5	0.56	0	0.33	0.46	0.34
SMCI7	10	0.13	0.55	1.26	3.24	1.29

5.5 DVMPC results

In the previous section, it was found that the use of ZOH helps the pneumatic system to reduce the valve switching frequency. Comparing the four sliding mode controllers, we found that SMCI7 gives the best tracking performance. Thus, we will study the DVMPC performance with different values of ZOH in this section.

As the SMCI7 in the previous section, we will first study DVMPC with ZOH=5 ms. In section 4.4.2, the cost function to be minimized was given. The desired pressures where set to $P_{a,d} = P_{b,d} = \frac{1}{2}(P_0 + P_s)$ to avoid operating with the chambers pressure too close to their upper or lower bounds. The values of N_p, w_v, w_{du} and w_p were manually tuned. The goal of tuning was to reduce the tracking errors and valve switching frequency. During the transient at the start of each step the piston is expected to move from it starting position to the desired final position immediately. This means that a large acceleration and large pneumatic force are required so DVMPC should not limit the pressures very much. To make this happen the value of w_p should be small. During the steady state portion, the piston is expected to stay at (or close to) the desired final position value. The pressures should be equal and kept close to their desired values in preparation for the next desired step change. The DVMPC should control the pressures more and therefore the value of w_p should be larger. Thus, a larger value of w_p was set when the tracking error was smaller than 2 mm, called w_{ps}. The tuning results are N_p = 15, w_v = $2\times10^{-6} s^3 \cdot m^{-1}$, w_{du} = $5.63\times10^{-5} s \cdot m$, w_p = $3\times10^{-17} s^5 \cdot m^3 \cdot kg^{-2}$ and w_{ps} = $1.5\times10^{-16} s^5 \cdot m^3 \cdot kg^{-2}$. The performance metrics are listed in Table 5.5.1 and the tracking performance is presented in Figure 5.5.1. Compared to SMCI7 with ZOH=5 ms, DVMPC with ZOH=5 ms has smaller values of SPS and t_s, but produced larger values of OS and RMSE.

To try to reduce the valve switching frequency, we set ZOH=10 ms with DVMPC. The tuned parameters are: N_p = 10, w_v = $2\times10^{-7} s^3 \cdot m^{-1}$, w_{du} = $5.43\times10^{-5} s \cdot m$, w_p = $3\times10^{-18} s^5 \cdot m^3 \cdot kg^{-2}$ and w_{ps} = $1.5\times10^{-17} s^5 \cdot m^3 \cdot kg^{-2}$. The performance metrics are listed in Table 5.5.1 and the tracking performance was presented in Figure 5.5.2. The value of SPS was reduced by 42% to 2.63 compared with DVMPC with ZOH=5 ms. The value of SSE was larger than 1 mm for the first step so it settling time was undefined. The value of OS for DVMPC ZOH=10 ms was similar to that of DVMPC with ZOH=5 ms.

Table 5.5.1 Comparisons of performance metrics for DVMPC with different values of ZOH in simulation.

ZOH (ms)	RMSE (mm)	SPS	SSE (mm)	ts (s)	OS (mm)
5	66.63	4.50	0.42	0.31	0.54
10	68.32	2.63	0.98	N/A	0.55

Table 5.5.2 Comparisons of SSE values (mm) for DVMPC with different values of ZOH in simulation.

ZOH (ms)	SSE_1	SSE_2	SSE_3	SSE_4	SSE
5	0.50	0.61	0.28	0.30	0.42
10	1.09	1.17	0.52	1.13	0.98

Table 5.5.3 Comparisons of t_s values (s) for DVMPC with different values of ZOH in simulation.

ZOH (ms)	t_{s1}	t_{s2}	t_{s3}	t_{s4}	t_s
5	0.42	0.39	0.27	0.17	0.31
10	N/A	0.84	0.69	0.97	N/A

Table 5.5.4 Comparisons of OS values (mm) for DVMPC with different values of ZOH in simulation.

ZOH (ms)	OS_1	OS_2	OS_3	OS_4	OS
5	0.50	0.65	0.37	0.66	0.54
10	1.09	0	0	1.13	0.55

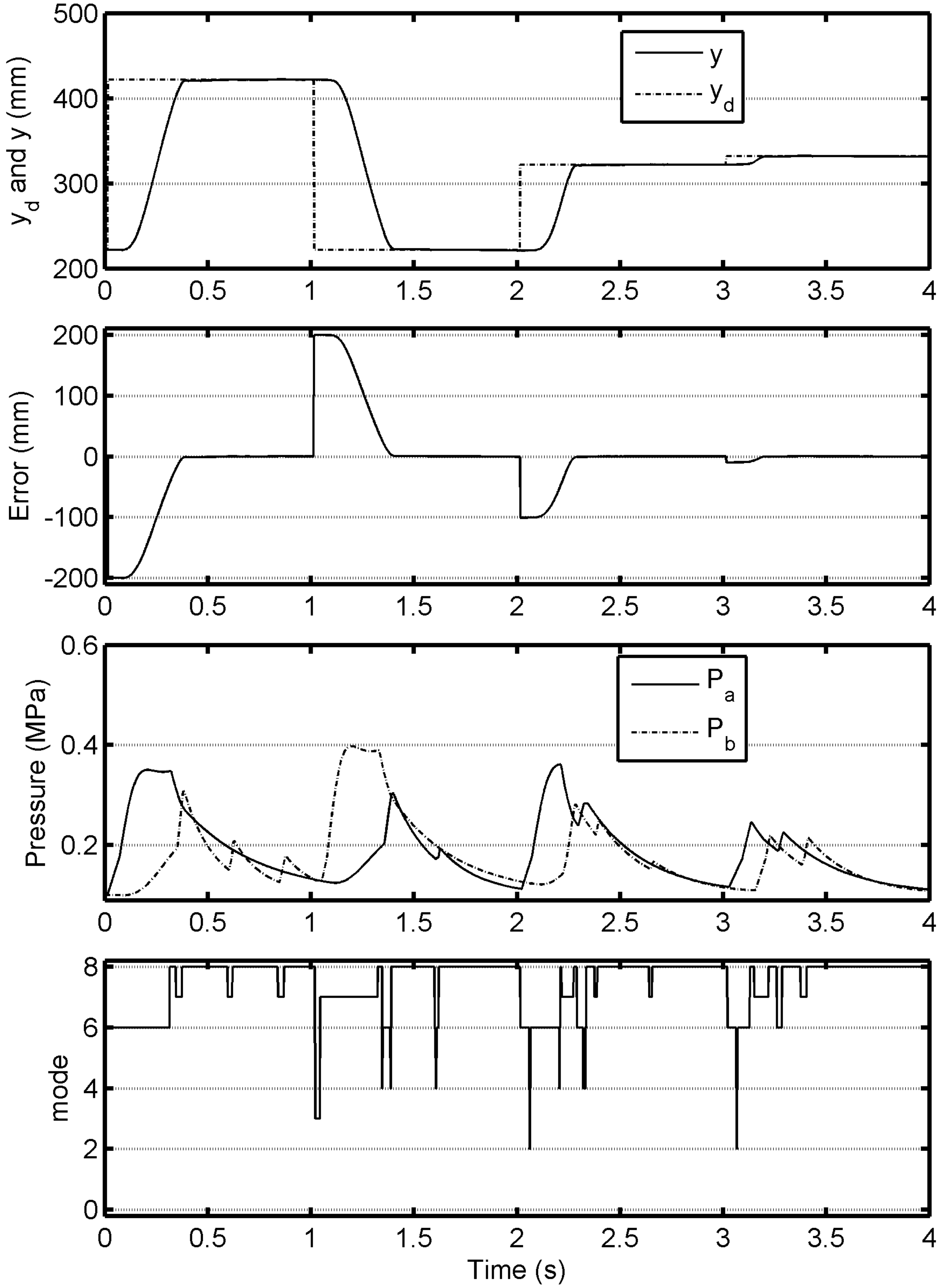

Figure 5.5.1 Simulation of HFC with DVMPC, ZOH=5 ms and *M*=2.14 kg

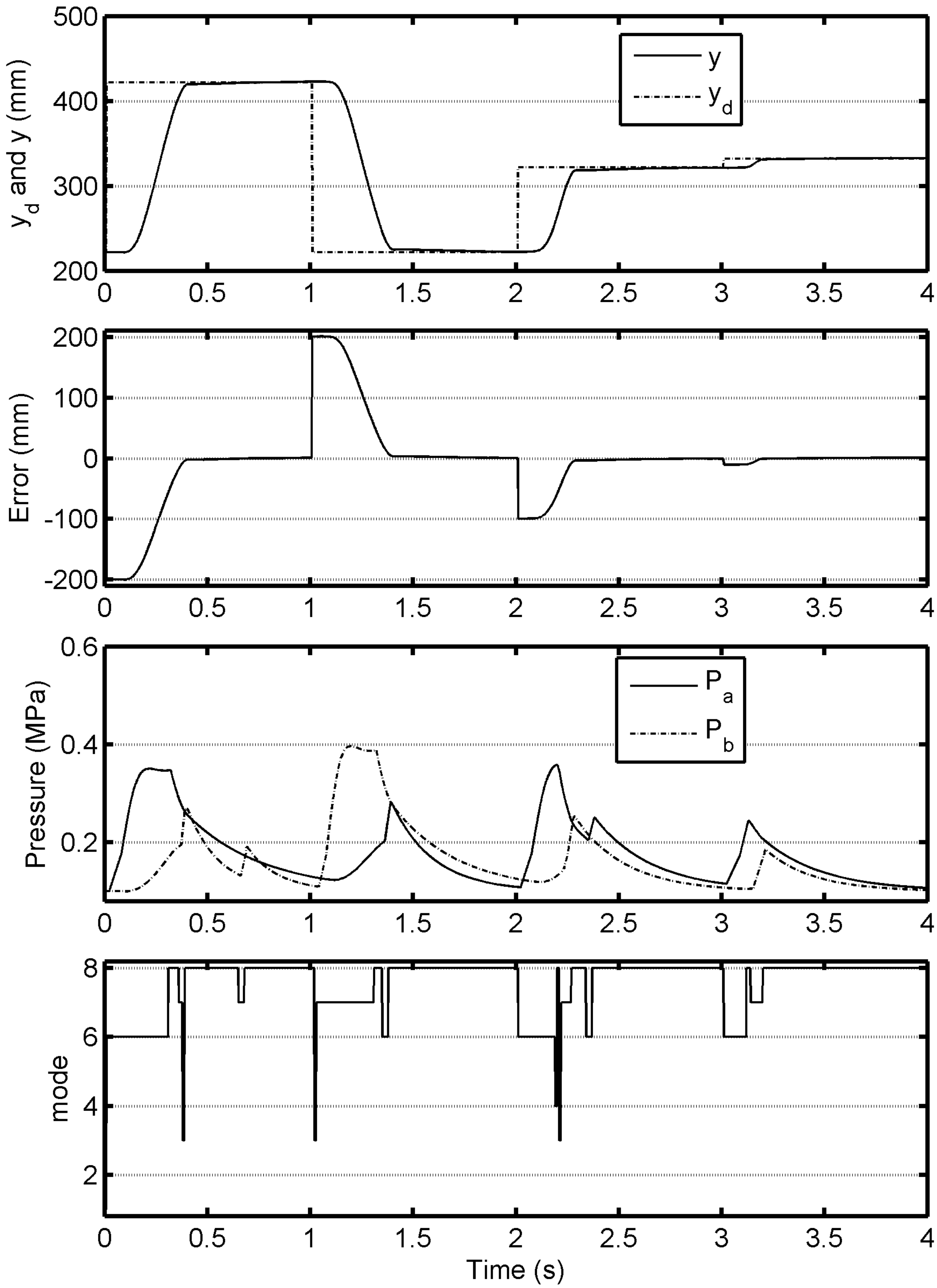

Figure 5.5.2 Simulation of HFC with DVMPC, ZOH=10 ms and M=2.14 kg

5.6 Payload mismatch simulations

5.6.1 Introduction

Robustness may be defined as the capacity of a controller to deal with external disturbances and plant modeling mismatch. Robustness is important in the design of controllers since it is unrealistic to assume we have a perfect plant model. In this section, we will study the effects of payload mismatch on the SMCI7 and DVMPC.

5.6.2 DVMPC

For the nominal case, the payload mass is 2.14 kg. Due to the existing mass in the lab, the smaller payload mass is 0.95 kg and the larger one is 3.24 kg in simulation. Since the results for DVMPC with ZOH = 5 ms are better than those with ZOH = 10 ms, we studied the robustness to payload mismatch for DVMPC with ZOH= 5 ms. With the controller parameters fixed, Tables 5.6.1 – 5.6.4 show the performance metrics for DVMPC with payload mismatch. Compared with the nominal case, the larger mass case has the similar RMSE, SPS and t_s, but has five times larger OS. It might be due to time required to decelerate the motion of the larger payload. For the smaller mass case, SPS is two times larger and SSE was increased by 57%. The value of OS of the smaller case is comparable with that of the nominal case. The worse performance with the smaller mass was unexpected and its reason is not obvious. It is a reminder that nonlinear systems often behave in unexpected ways.

Table 5.6.1 Comparisons of performance metrics for DVMPC with HFC and payload mismatch in simulation.

Mass (kg)	RMSE (mm)	SPS	SSE (mm)	t_s (s)	OS (mm)
2.14	66.63	4.50	0.42	0.31	0.54
0.95	62.38	12.75	0.66	0.45	0.76
3.24	65.75	4.63	0.41	0.36	3.31

Table 5.6.2 Comparisons of SSE values (mm) for DVMPC with HFC and payload mismatch in simulation.

Mass (kg)	SSE_1	SSE_2	SSE_3	SSE_4	SSE
2.14	0.50	0.61	0.28	0.30	0.42
0.95	0.55	0.55	0.55	0.99	0.66
3.24	0.69	0.44	0.21	0.29	0.41

Table 5.6.3 Comparisons of t_s values (s) for DVMPC with HFC and payload mismatch in simulation.

Mass (kg)	t_{s1}	t_{s2}	t_{s3}	t_{s4}	t_s
2.14	0.42	0.39	0.27	0.17	0.31
0.95	0.74	0.42	0.42	0.23	0.45
3.24	0.44	0.43	0.40	0.19	0.36

Table 5.6.4 Comparisons of OS values (mm) for DVMPC with HFC and payload mismatch in simulation.

Mass (kg)	OS_1	OS_2	OS_3	OS_4	OS
2.14	0.50	0.65	0.37	0.66	0.54
0.95	1.21	0.64	0.25	0.96	0.76
3.24	4.32	4.22	4.32	0.38	3.31

5.6.3 SMCI7

For the SMCI7, the values of the nominal, smaller and larger payload mass are also 2.14 kg, 0.95 kg and 3.24 kg, respectively. We also simulated SMCI7 with ZOH = 5 ms. With the controller parameters fixed, Tables 5.6.5 – 5.6.8 show the performance metrics for SMCI7 with payload mismatch. Compared with the nominal case, the larger mass case has the similar RMSE, SSE and SPS, but has a 15 times larger OS and 79% larger t_s. t_s, OS and SPS are 44% , 59% and 57% larger, respectively, compared to the larger mass case of DVMPC. For the smaller mass case, RMSE is 2% smaller than that of the nominal case but the values of SPS and SSE are 190% and 51% larger, respectively. The value of OS and t_s of the smaller case is comparable with that of the nominal case. Similarly, t_s is 25% larger than that of the smaller mass case of DVMPC.

Table 5.6.5 Comparisons of performance metrics for SMCI7 with HFC and payload mismatch in simulation.

Mass (kg)	RMSE (mm)	SPS	SSE (mm)	t_s (s)	OS (mm)
2.14	62.98	5.13	0.35	0.32	0.34
0.95	61.99	14.88	0.53	0.34	0.61
3.24	64.55	7.25	0.37	0.52	5.27

Table 5.6.6 Comparisons of SSE values (mm) for SMCI7 with HFC and payload mismatch in simulation.

Mass (kg)	SSE_1	SSE_2	SSE_3	SSE_4	SSE
2.14	0.55	0.06	0.32	0.46	0.35
0.95	0.56	0.53	0.78	0.27	0.53
3.24	0.08	0.61	0.19	0.62	0.37

Table 5.6.7 Comparisons of t_s values (s) for SMCI7 with HFC and payload mismatch in simulation.

Mass (kg)	t_{s1}	t_{s2}	t_{s3}	t_{s4}	t_s
2.14	0.46	0.36	0.36	0.09	0.32
0.95	0.47	0.47	0.28	0.15	0.34
3.24	0.46	0.49	0.69	0.44	0.52

Table 5.6.8 Comparisons of OS values (mm) for SMCI7 with HFC and payload mismatch in simulation.

Mass (kg)	OS_1	OS_2	OS_3	OS_4	OS
2.14	0.56	0	0.33	0.46	0.34
0.95	0.89	0.53	0.72	0.28	0.61
3.24	3.71	2.66	10.40	4.32	5.27

5.7 Simulations with a low friction cylinder

In the previous subsection, DVMPC performed well with the HFC. In this section, we will try simulating DVMPC with a low friction cylinder (LFC). SMCI7 will be also be simulated with the LFC for comparison purposes. Payload mismatch will also be simulated with the LFC to study the robustness of the controllers.

The LFC (SMC Corporation, model number CM2XB25-300) has a 300mm stroke. It is a single rod cylinder with a 25 mm dia. piston and a 10 mm dia. rod. The simulated LFC system uses the same four on/off valves, flow control, encoder and pressure sensors as the HFC. Thus, the system dynamic model and valve model of the LFC are same as those of the HFC. A 1 kHz sampling frequency is used. Friction model is used same as that presented for this LFC by Ning and Bone (2005). The equation is (3.5.2) and the parameters are $F_s = 18$ N, $F_c = 13$ N and $C_v = 44$ N/m/s.

5.7.1 DVMPC and SMCI7 with nominal mass

In this subsection, DVMPC and SMCI7 will be used with the LFC and its nominal payload mass. The controllers with different values of ZOH will be also studied.

5.7.1.1 DVMPC

Similar to DVMPC in section 5.5, we will first study the case with ZOH= 5 ms. The values of N_p, w_v, w_{du}, w_p and w_{ps} were manually tuned to minimize SPS and SSE at the same time. The results are listed in Table 5.7.1. To reduce the valve switching frequency, we tried DVMPC with ZOH = 10 ms and ZOH = 20 ms. The parameters of cost function are also listed in Table 5.7.1. Tables 5.7.2 – 5.7.5 show the comparisons of the performance metrics with different values of ZOH. Figures 5.7.1 –5.7.3 show the tracking performances with different values of ZOH.

From Tables 5.7.2 – 5.7.5 and Figures 5.7.1 – 5.7.3, the value of SPS is smaller, but the values of RMSE, SSE, t_s and OS are larger with larger values of ZOH. With ZOH = 10 ms, the SPS is reduced by 21%, but RMSE, t_s and SSE are increased by 3%, 35% and 95%, respectively. The preferable value of ZOH depends on which metric is more important to the application. Large values of ZOH give the valves less opportunities to switch, thus the valve switching frequency is reduced and tracking errors are increased.

Table 5.7.1 Parameters of DVMPC for the LFC with different values of ZOH in simulation.

ZOH(ms)	N_p	w_v ($s^3 \cdot m^{-1}$)	w_{du} ($s \cdot m$)	w_p ($s^5 \cdot m^3 \cdot kg^{-2}$)	w_{ps} ($s^5 \cdot m^3 \cdot kg^{-2}$)
5	20	2×10^{-9}	1.4×10^{-5}	3×10^{-17}	1.5×10^{-16}
10	10	2×10^{-8}	9×10^{-6}	9×10^{-18}	9×10^{-17}
20	6	2×10^{-8}	3×10^{-6}	0	1.5×10^{-17}

Table 5.7.2 Comparisons of performance metrics for DVMPC of the LFC with different values of ZOH in simulation.

ZOH (ms)	RMSE (mm)	SPS	SSE (mm)	t_s (s)	OS (mm)
5	21.61	5.88	0.20	0.17	0.39
10	22.19	4.63	0.39	0.23	0.40
20	25.22	3.88	0.41	0.25	0.67

Table 5.7.3 Comparisons of SSE values (mm) for DVMPC of the LFC with different values of ZOH in simulation.

ZOH (ms)	SSE_1	SSE_2	SSE_3	SSE_4	SSE
5	0.17	0.16	0.32	0.15	0.20
10	0.60	0.42	0.39	0.17	0.39
20	0.93	0.14	0.39	0.17	0.41

Table 5.7.4 Comparisons of t_s values (s) for DVMPC of the LFC with different values of ZOH in simulation.

ZOH (ms)	t_{s1}	t_{s2}	t_{s3}	t_{s4}	t_s
5	0.21	0.20	0.19	0.09	0.17
10	0.27	0.32	0.23	0.12	0.23
20	0.34	0.29	0.25	0.12	0.25

Table 5.7.5 Comparisons of OS values (mm) for DVMPC of the LFC with different values of ZOH in simulation.

ZOH (ms)	OS_1	OS_2	OS_3	OS_4	OS
5	0.17	0.18	1.01	0.20	0.39
10	0.60	0.45	0.39	0.17	0.40
20	0.93	1.16	0.41	0.17	0.67

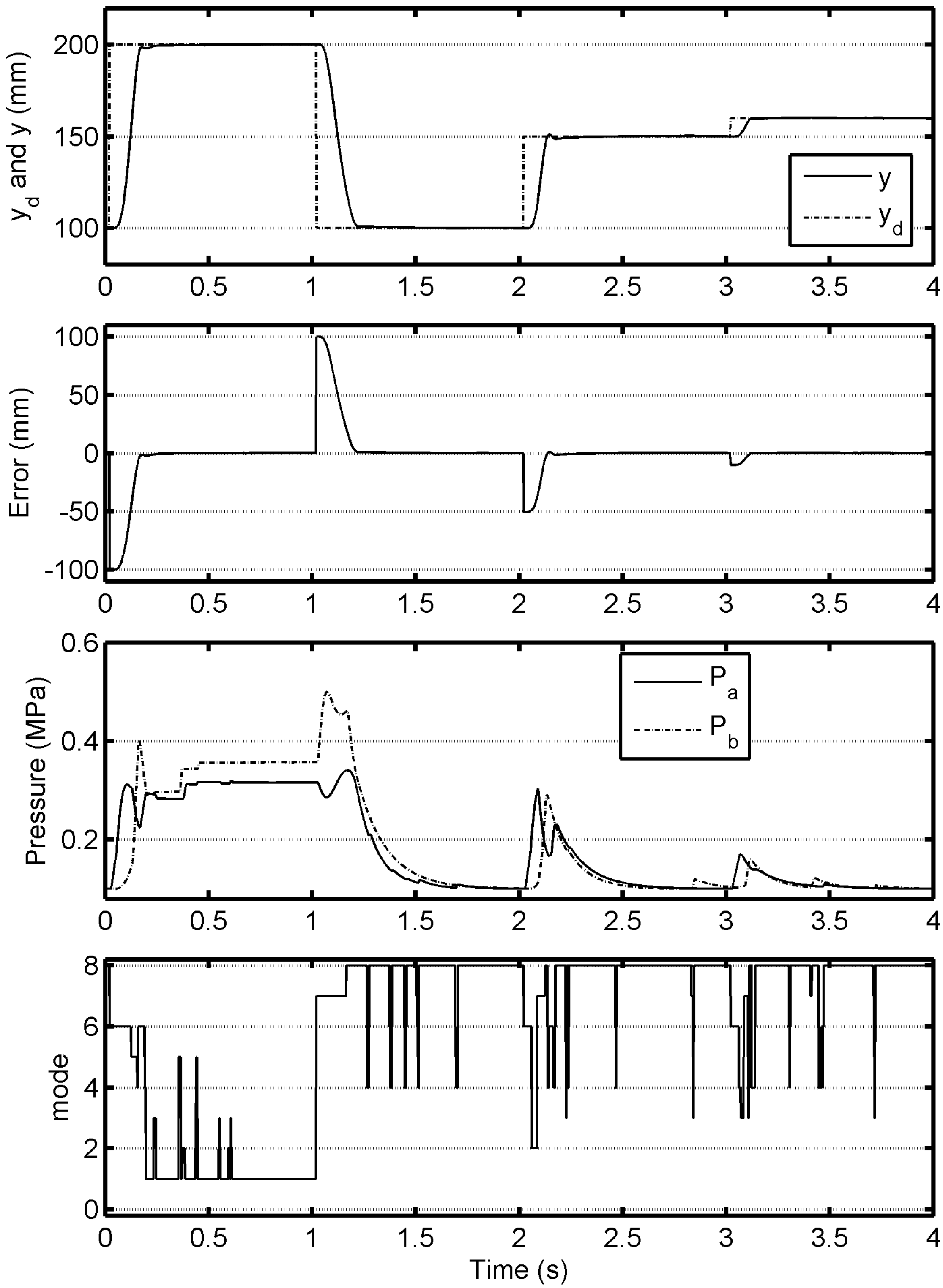

Figure 5.7.1 Simulation of LFC with DVMPC, ZOH=5 ms and *M*=2.14 kg

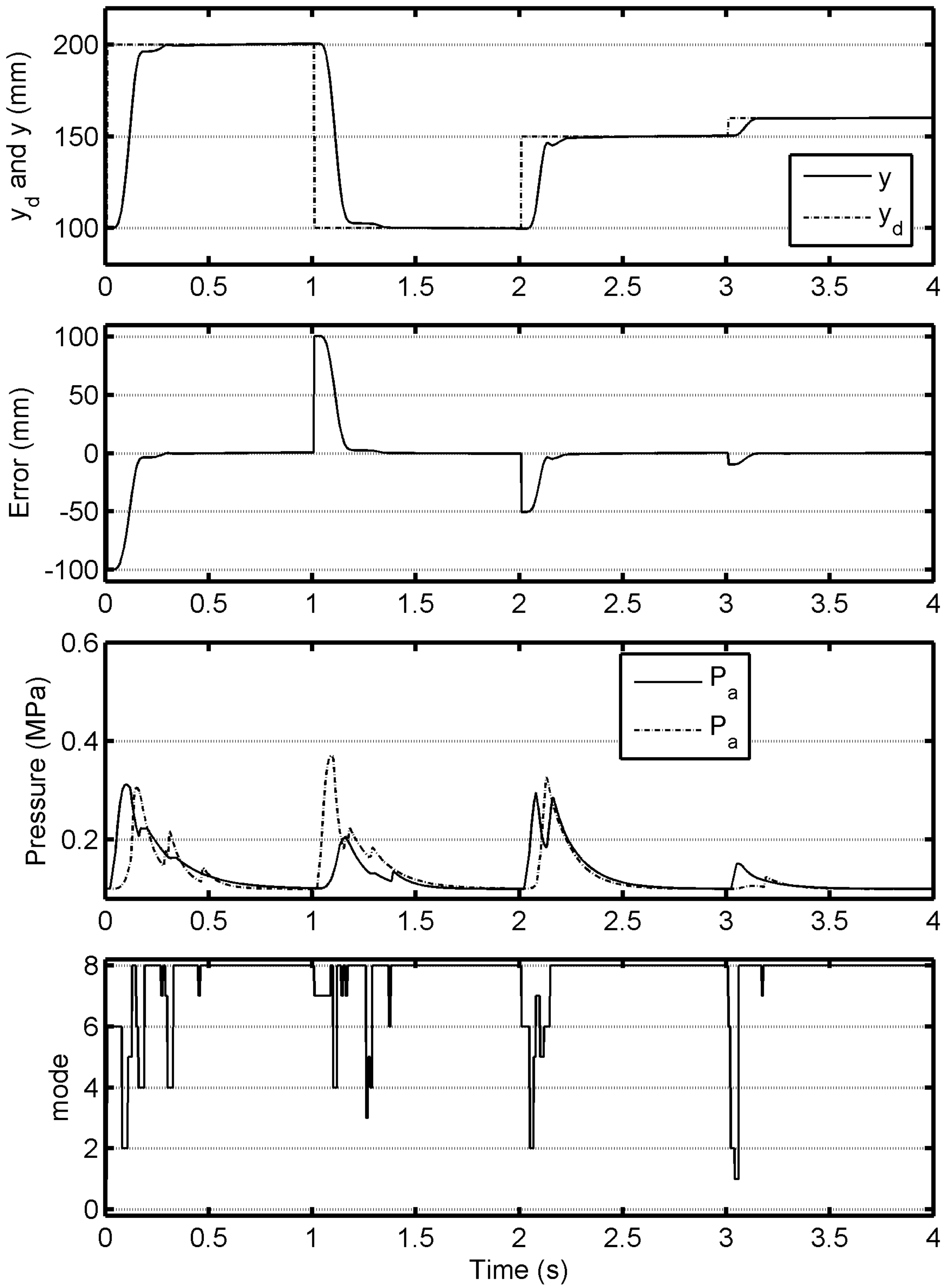

Figure 5.7.2 Simulation of LFC with DVMPC, ZOH=10 ms and *M*=2.14 kg

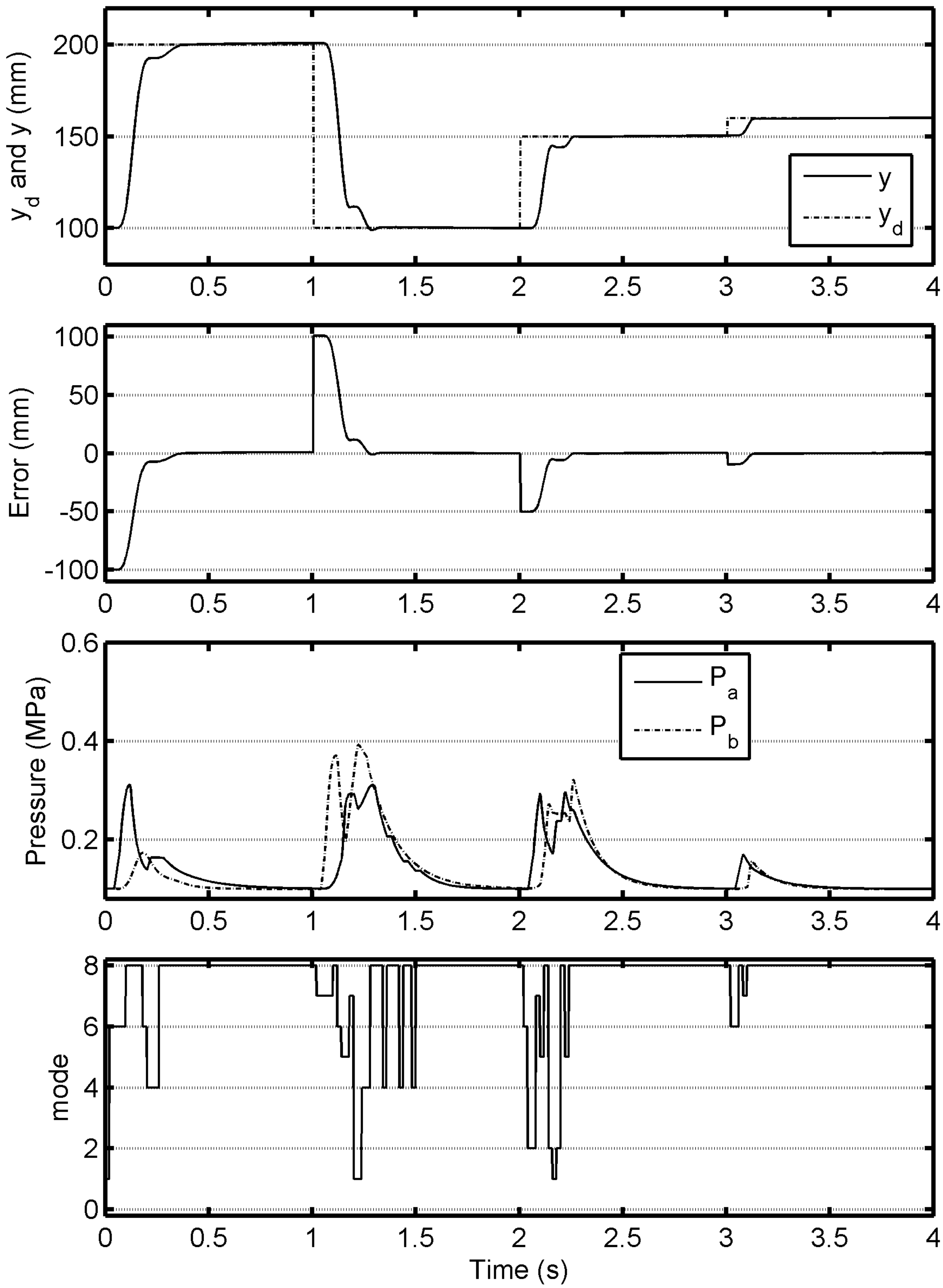

Figure 5.7.3 Simulation of LFC with DVMPC, ZOH=20 ms and M=2.14 kg

5.7.1.2 SMCI7

We simulated SMCI7 with ZOH= 5 ms, ZOH= 10 ms and ZOH= 20 ms on the LFC for the purposes of comparison with DVMPC. The controller parameters are same as those in section 5.4. Tables 5.7.6 – 5.7.9 show the comparisons of performance metrics with different values of ZOH. Figures 5.7.4 – 5.7.6 show the tracking performances.

With ZOH= 5 ms, SMCI7 has similar SSE, t_s and OS as DVMPC but 51% larger value of SPS and 3% smaller value of RMSE. With larger values of ZOH, the values of SPS are not reduced as expected. With ZOH= 10 ms, SPS is twice as that with ZOH= 20 ms. RMSE is 1% smaller and SSE, t_s and OS are 84%, 85% and 241% larger than those with ZOH= 5 ms. Thus, SMCI7 with ZOH= 5 ms gives a worse tracking performance than SMCI7 with ZOH= 10 ms. For the case with ZOH= 20 ms, the system is oscillating in a limit cycle as shown in Figure 5.7.6. Instability is not allowed, thus SMCI7 with ZOH= 20 ms fails to control our system. Overall, SMCI7 has a good tracking performance with ZOH= 5 ms.

Table 5.7.6 Comparisons of performance metrics for SMCI7 of the LFC with different values of ZOH in simulation.

ZOH (ms)	RMSE (mm)	SPS	SSE (mm)	t_s (s)	OS (mm)
5	21.03	8.88	0.18	0.20	0.34
10	20.85	16.38	0.42	0.37	1.16
20	22.86	21.75	11.50	N/A	10.11

Table 5.7.7 Comparisons of SSE values (mm) for SMCI7 of the LFC with different values of ZOH in simulation.

ZOH (ms)	SSE_1	SSE_2	SSE_3	SSE_4	SSE
5	0.11	0.36	0.06	0.17	0.18
10	0.57	0.54	0.17	0.42	0.42
20	unstable				

Table 5.7.8 Comparisons of t_s values (s) for SMCI7 of the LFC with different values of ZOH in simulation.

ZOH (ms)	t_{s1}	t_{s2}	t_{s3}	t_{s4}	t_s
5	0.26	0.28	0.19	0.09	0.20
10	0.70	0.33	0.21	0.24	0.37
20	N/A	N/A	N/A	N/A	N/A

Table 5.7.9 Comparisons of OS values (mm) for SMCI7 of the LFC with different values of ZOH in simulation.

ZOH (ms)	OS_1	OS_2	OS_3	OS_4	OS
5	0.18	0.36	0	0.82	0.34
10	1.63	0.54	0.18	2.29	1.16
20	12.36	6.33	11.03	10.72	10.11

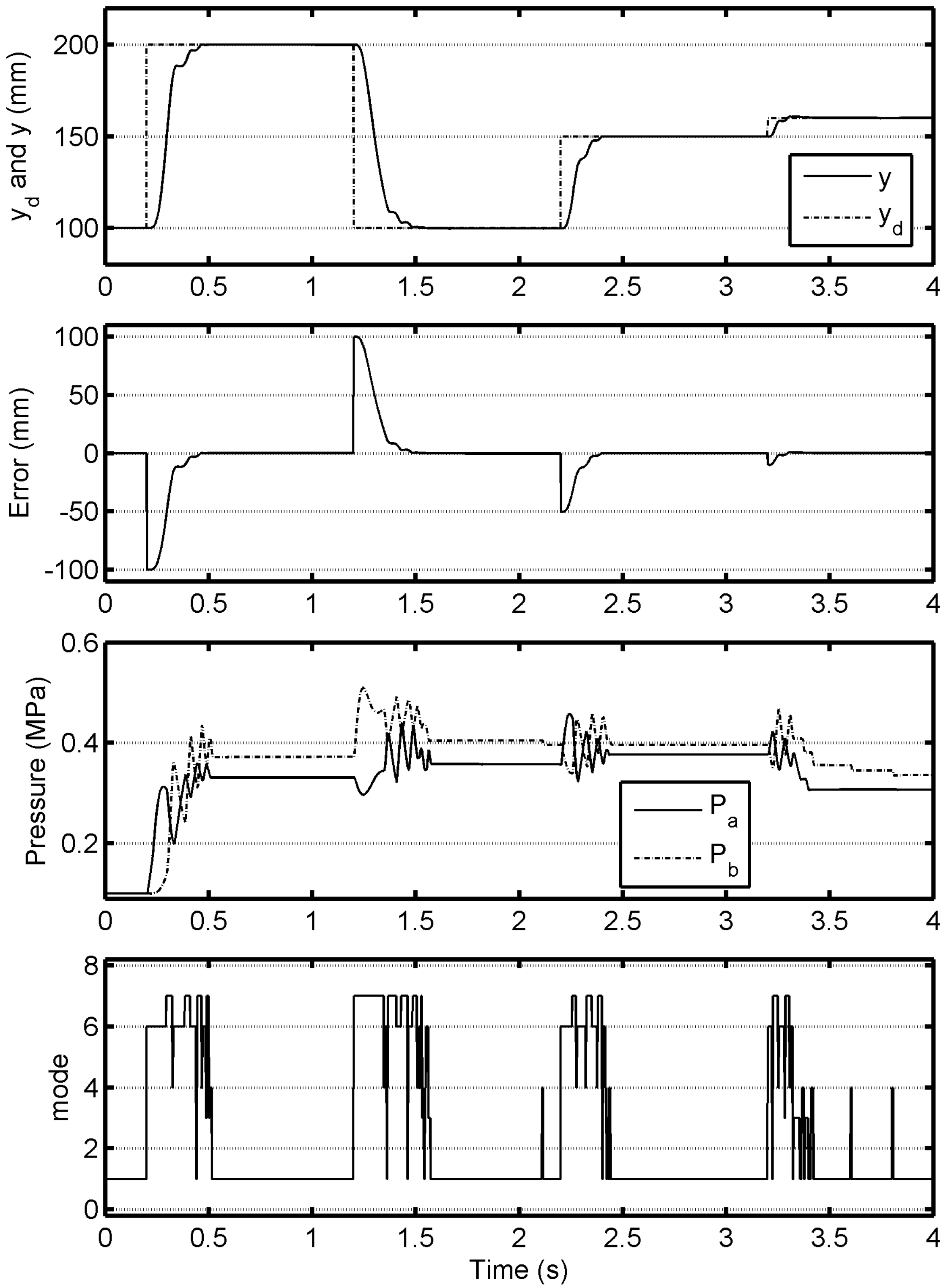

Figure 5.7.4 Simulation of LFC with SMCI7, ZOH=5 ms and *M*=2.14 kg

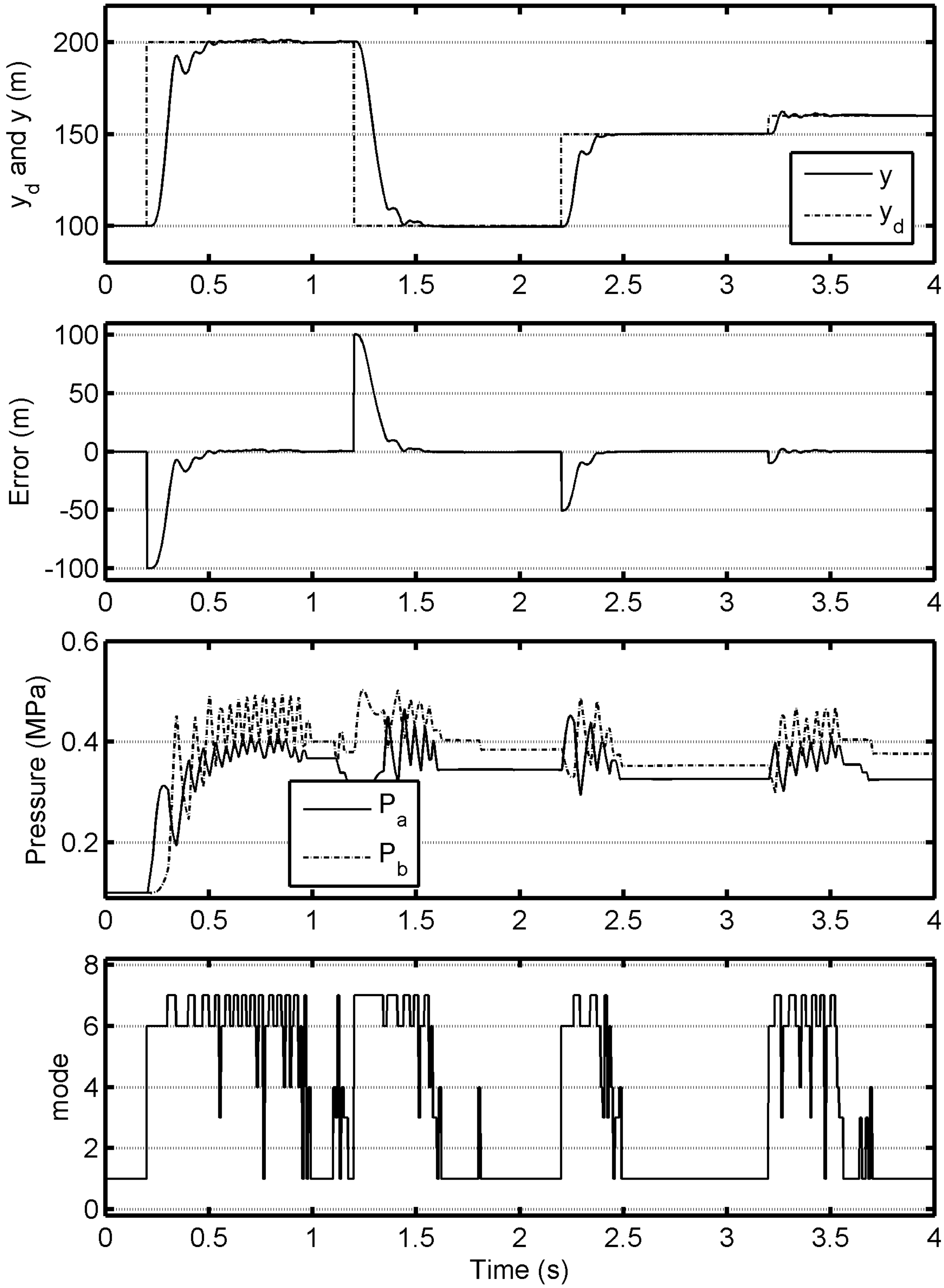

Figure 5.7.5 Simulation of LFC with SMCI7, ZOH=10 ms and *M*=2.14 kg

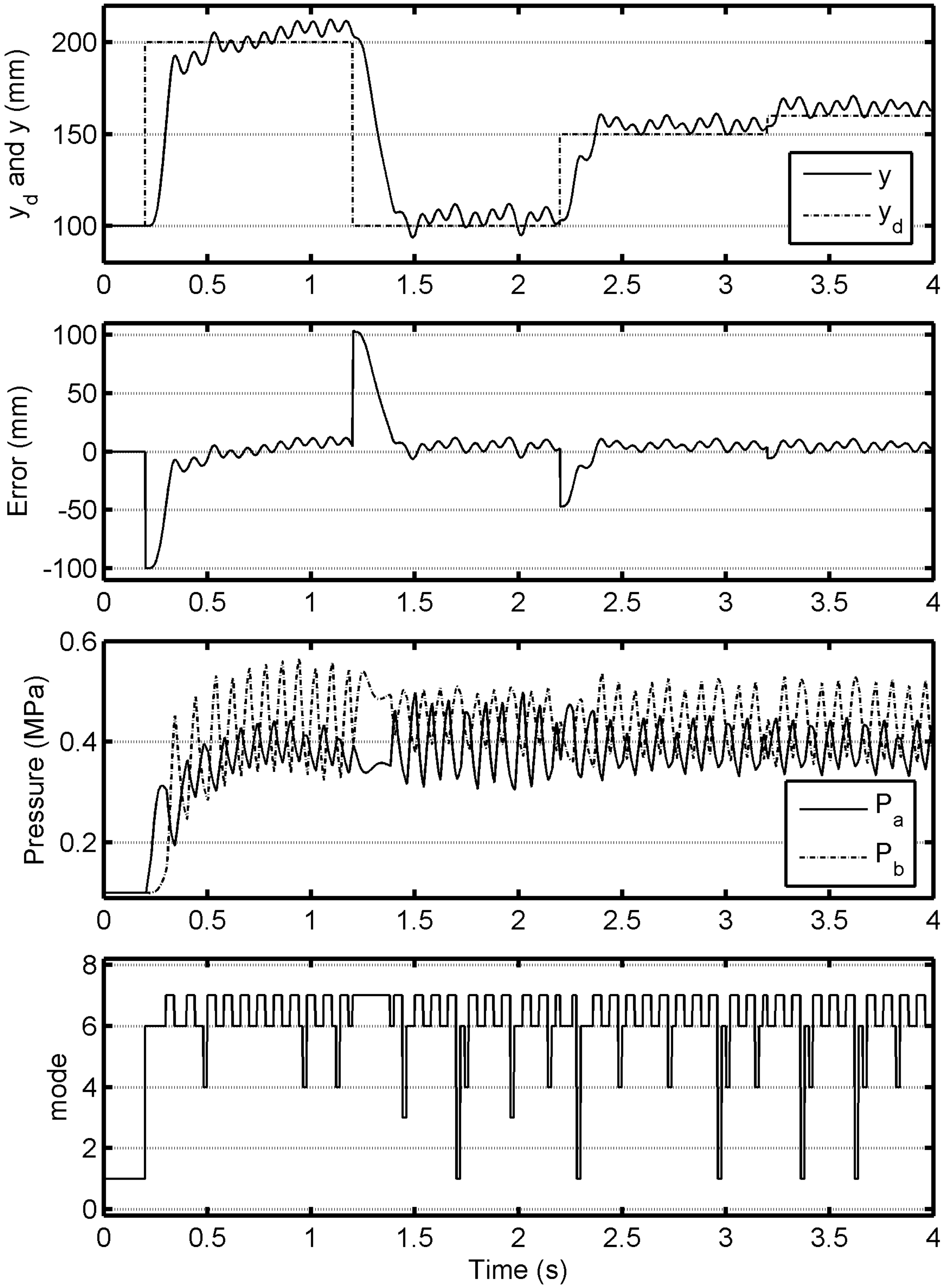

Figure 5.7.6 Simulation of LFC with SMCI7, ZOH=20 ms and M=2.14 kg

5.7.2 DVMPC and SMCI7 with payload mismatch

In this subsection, robustness to payload mismatch will be studied for DVMPC and SMCI7 of the LFC. The larger payload mass is 3.24 kg and the smaller one is 0.95 kg.

5.7.2.1 DVMPC

In subsection 5.7.1.1, we simulated DVMPC of the LFC with different values of ZOH. DVMPC with ZOH = 5 ms, ZOH = 10 ms and ZOH = 20 ms gave satisfactory tracking results, thus we will study the payload mismatch for DVMPC with ZOH = 5 ms, ZOH = 10 ms and ZOH= 20 ms in this subsection.

Tables 5.7.10 – 5.7.13 list the performance metrics for DVMPC with payload mismatch. With ZOH= 5 ms, the smaller payload case has a 7% smaller RMSE but SPS and SSE are increased by 166% and 180%, respectively, compared with the nominal payload case. The t_s and OS are similar for the smaller payload and nominal payload cases. For the larger payload case, RMSE and t_s are increased by 11% and 23%, respectively. The value of OS is ten times larger than that of the nominal payload case. With ZOH= 10 ms, the smaller payload case has 4% smaller RMSE but 146% larger SPS and 125% larger SSE than the nominal payload case. The values of OS are similar for the smaller payload and nominal payload cases. The system does not settle within 1 mm for the first and fourth step thus the settling time is undefined. The larger payload case has larger RMSE and OS than the nominal payload case. The values of SPS, SSE and t_s are similar for the smaller payload and nominal payload cases. With ZOH= 20 ms, the smaller payload case has 226%, 68%, 1.2% larger SPS, SSE and t_s, respectively. The larger payload case has 52%, 88% and 60% larger SPS, SSE and t_s, respectively. The values of RMSE and OS are similar for all the three cases.

Table 5.7.10 Comparisons of performance metrics for DVMPC of the LFC with payload mismatch in simulation.

Mass (kg)	RMSE (mm)	SPS	SSE (mm)	t_s (s)	OS (mm)
ZOH = 5 ms, N_p =20, w_v =2×10^{-9} $s^3 \cdot m^{-1}$, w_{du} =1.4×10^{-5} $s \cdot m$, w_p =3×10^{-17} $s^5 \cdot m^3 \cdot kg^{-2}$ and w_{ps} =1.5×10^{-16} $s^5 \cdot m^3 \cdot kg^{-2}$					
2.14	21.61	5.88	0.20	0.17	0.39
0.95	20.16	15.63	0.56	0.18	0.56
3.24	22.30	6.00	0.24	0.21	4.02
ZOH = 10 ms, N_p =10, w_v =2×10^{-8} $s^3 \cdot m^{-1}$, w_{du} =9×10^{-6} $s \cdot m$, w_p =9×10^{-18} $s^5 \cdot m^3 \cdot kg^{-2}$ and w_{ps} =9×10^{-17} $s^5 \cdot m^3 \cdot kg^{-2}$					
2.14	22.19	4.63	0.40	0.22	0.40
0.95	21.20	11.38	0.90	N/A	0.27
3.24	23.01	4.50	0.36	0.25	2.41
ZOH = 20 ms, N_p =6, w_v =2×10^{-8} $s^3 \cdot m^{-1}$, w_{du} =3×10^{-6} $s \cdot m$, w_p =0 and w_{ps} =1.5×10^{-17} $s^5 \cdot m^3 \cdot kg^{-2}$					
2.14	25.22	3.88	0.41	0.25	0.67
0.95	24.72	12.63	0.69	0.55	1.53
3.24	25.93	5.88	0.77	0.40	0.79

Table 5.7.11 Comparisons of SSE values (mm) for DVMPC of the LFC with payload mismatch in simulation.

Mass (kg)	SSE_1	SSE_2	SSE_3	SSE_4	SSE
ZOH = 5 ms, N_p =20, w_v =2×10^{-9} $s^3 \cdot m^{-1}$, w_{du} =1.4×10^{-5} $s \cdot m$, w_p =3×10^{-17} $s^5 \cdot m^3 \cdot kg^{-2}$ and w_{ps} =1.5×10^{-16} $s^5 \cdot m^3 \cdot kg^{-2}$					
2.14	0.17	0.16	0.32	0.15	0.20
0.95	0.23	0.66	0.54	0.82	0.56
3.24	0.17	0.19	0.24	0.37	0.24
ZOH = 10 ms, N_p =10, w_v =2×10^{-8} $s^3 \cdot m^{-1}$, w_{du} =9×10^{-6} $s \cdot m$, w_p =9×10^{-18} $s^5 \cdot m^3 \cdot kg^{-2}$ and w_{ps} =9×10^{-17} $s^5 \cdot m^3 \cdot kg^{-2}$					
2.14	0.60	0.42	0.39	0.17	0.40
0.95	1.02	0.53	0.56	1.48	0.90
3.24	0.78	0.11	0.30	0.26	0.36
ZOH = 20 ms, N_p =6, w_v =2×10^{-8} $s^3 \cdot m^{-1}$, w_{du} =3×10^{-6} $s \cdot m$, w_p =0 and w_{ps} =1.5×10^{-17} $s^5 \cdot m^3 \cdot kg^{-2}$					
2.14	0.93	0.14	0.39	0.17	0.41
0.95	0.79	0.30	0.88	0.80	0.69
3.24	0.85	0.53	0.90	0.78	0.77

Table 5.7.12 Comparisons of t_s values (s) for DVMPC of the LFC with payload mismatch in simulation.

Mass (kg)	t_{s1}	t_{s2}	t_{s3}	t_{s4}	t_s
ZOH = 5 ms, N_p =20, w_v =2×10^{-9} $s^3 \cdot m^{-1}$, w_{du} =1.4×10^{-5} $s \cdot m$, w_p =3×10^{-17} $s^5 \cdot m^3 \cdot kg^{-2}$ and w_{ps} =1.5×10^{-16} $s^5 \cdot m^3 \cdot kg^{-2}$					
2.14	0.20	0.20	0.19	0.09	0.17
0.95	0.19	0.28	0.14	0.12	0.18
3.24	0.25	0.25	0.21	0.12	0.21
ZOH = 10 ms, N_p =10, w_v =2×10^{-8} $s^3 \cdot m^{-1}$, w_{du} =9×10^{-6} $s \cdot m$, w_p =9×10^{-18} $s^5 \cdot m^3 \cdot kg^{-2}$ and w_{ps} =9×10^{-17} $s^5 \cdot m^3 \cdot kg^{-2}$					
2.14	0.26	0.31	0.22	0.11	0.22
0.95	N/A	0.32	0.40	N/A	N/A
3.24	0.46	0.23	0.15	0.14	0.25
ZOH = 20 ms, N_p =6, w_v =2×10^{-8} $s^3 \cdot m^{-1}$, w_{du} =3×10^{-6} $s \cdot m$, w_p =0 and w_{ps} =1.5×10^{-17} $s^5 \cdot m^3 \cdot kg^{-2}$					
2.14	0.34	0.29	0.25	0.12	0.25
0.95	0.74	0.76	0.35	0.36	0.55
3.24	0.35	0.40	0.46	0.41	0.40

Table 5.7.13 Comparisons of OS values (mm) for DVMPC of the LFC with payload mismatch in simulation.

Mass (kg)	OS_1	OS_2	OS_3	OS_4	OS
ZOH = 5 ms, N_p =20, w_v =2×10^{-9} $s^3 \cdot m^{-1}$, w_{du} =1.4×10^{-5} $s \cdot m$, w_p =3×10^{-17} $s^5 \cdot m^3 \cdot kg^{-2}$ and w_{ps} =1.5×10^{-16} $s^5 \cdot m^3 \cdot kg^{-2}$					
2.14	0.17	0.18	1.01	0.20	0.39
0.95	0.79	0.66	0.54	0.26	0.56
3.24	5.33	7.26	3.12	0.37	4.02
ZOH = 10 ms, N_p =10, w_v =2×10^{-8} $s^3 \cdot m^{-1}$, w_{du} =9×10^{-6} $s \cdot m$, w_p =9×10^{-18} $s^5 \cdot m^3 \cdot kg^{-2}$ and w_{ps} =9×10^{-17} $s^5 \cdot m^3 \cdot kg^{-2}$					
2.14	0.60	0.45	0.39	0.17	0.40
0.95	0.39	0.12	0.56	0	0.27
3.24	4.88	4.51	0	0.26	2.41
ZOH = 20 ms, N_p =6, w_v =2×10^{-8} $s^3 \cdot m^{-1}$, w_{du} =3×10^{-6} $s \cdot m$, w_p =0 and w_{ps} =1.5×10^{-17} $s^5 \cdot m^3 \cdot kg^{-2}$					
2.14	0.93	1.16	0.41	0.17	0.67
0.95	4.11	0.31	0.88	0.80	1.53
3.24	0.86	0	2.32	0	0.79

5.7.2.2 SMCI7

In the subsection 5.7.1.2, SMCI7 with ZOH = 5 ms and ZOH = 10 ms produced stable results, while SMCI7 with ZOH = 20 ms did not. In this subsection, we will evaluate the robustness to payload mismatch for SMCI7 of the LFC with ZOH= 5 ms and ZOH= 10 ms.

Tables 5.7.14 –5.7.17 list the performance metrics with payload mismatch for SMCI7 with ZOH= 5 ms and ZOH= 10 ms. With ZOH= 5 ms, the smaller payload case has 7% smaller RMSE but 94%, 15% and 118% larger SPS, t_s and OS, respectively than the nominal case. The values of SSE are similar for the smaller payload and nominal payload cases. The larger payload case has 6% larger RMSE but 133% larger SSE than the nominal case. The values of SPS and t_s are similar for the larger payload and nominal payload cases.

With ZOH= 10 ms, the smaller payload case has 47% larger SPS, 245% SSE and 113% OS than the nominal case. The value of RMSE is similar for the smaller payload and nominal payload cases. The settling times became undefined due to the SSE greater than 1 mm. The larger payload case has 43% smaller SPS and 45% smaller SSE and 45% smaller 30% t_s than the nominal case. The values of RMSE and OS of larger payload case are larger than the nominal case.

Table 5.7.14 Comparisons of performance metrics for SMCI7 of the LFC with payload mismatch in simulation.

ZOH (ms)	Mass (kg)	RMSE (mm)	SPS	SSE (mm)	t_s (s)	OS (mm)
5	2.14	21.03	8.88	0.18	0.20	0.34
5	0.95	19.51	17.25	0.20	0.23	0.74
5	3.24	22.24	8.25	0.42	0.19	0.42
10	2.14	20.85	16.38	0.42	0.37	1.16
10	0.95	20.75	24	1.45	N/A	2.47
10	3.24	22.16	9.38	0.23	0.26	1.63

Table 5.7.15 Comparisons of SSE values (mm) for SMCI7 of the LFC with payload mismatch in simulation.

ZOH (ms)	Mass (kg)	SSE_1	SSE_2	SSE_3	SSE_4	SSE
5	2.14	0.11	0.36	0.06	0.17	0.18
5	0.95	0.50	0.11	0.14	0.04	0.20
5	3.24	0.40	0.31	0.34	0.65	0.42

10	2.14	0.57	0.54	0.17	0.42	0.42
10	0.95	4.70	0.88	0.13	0.08	1.45
10	3.24	0.23	0.21	0.36	0.12	0.23

Table 5.7.16 Comparisons of t_s values (s) for SMCI7 of the LFC with payload mismatch in simulation.

ZOH (ms)	Mass (kg)	t_{s1}	t_{s2}	t_{s3}	t_{s4}	t_s
5	2.14	0.26	0.28	0.19	0.09	0.20
5	0.95	0.28	0.30	0.25	0.09	0.23
5	3.24	0.29	0.25	0.17	0.06	0.19
10	2.14	0.70	0.33	0.21	0.24	0.37
10	0.95	N/A	0.36	0.39	0.28	N/A
10	3.24	0.47	0.29	0.21	0.09	0.26

Table 5.7.17 Comparisons of OS values (mm) for SMCI7 of the LFC with payload mismatch in simulation.

ZOH (ms)	Mass (kg)	OS_1	OS_2	OS_3	OS_4	OS
5	2.14	0.18	0.36	0	0.82	0.34
5	0.95	0.56	0.88	1.22	0.30	0.74
5	3.24	0.56	0.47	0	0.65	0.42
10	2.14	1.63	0.54	0.18	2.29	1.16
10	0.95	4.70	0.91	2.85	1.42	2.47
10	3.24	1.44	1.77	1.78	1.53	1.63

5.8 Discussions of the plots and tables

In the previous sections, the sliding mode controllers and DVMPC were simulated for the HFC and LFC; and some comparisons were made. The results will be further compared and discussed in this section.

From Tables 5.3.1 – 5.3.4, the value of SPS of SMC7 was reduced by 44% compared with SMC3 and that of SMCI7 is reduced by 63% compared with SMCI3. The values of SPS illustrate that the additional four modes contribute to the reduction of valve switching frequency. The value of OS of SMCI7 was reduced by 94% compared by SMC7 and the value of t_s is reduced by 30%, which demonstrates that the addition of integral action is useful for reduction of OS and t_s. Due to the integral action, the value of SSE of SMCI7 was reduced by 42%.

Comparing Tables 5.4.1 and 5.3.1, the value of SPS of SMCI7 with ZOH = 5 ms was reduced by 51%. The value of SSE was increased by 41%. The error does not settle within 1 mm for all the steps for SMCI7 with ZOH = 10 ms. These results indicate the system does not necessarily have better tracking performance with large values of ZOH. A larger value of ZOH can help reduce the valve switching frequency but might result in larger steady state error.

From Tables 5.4.1 and 5.5.1, the value of SPS of DVMPC with ZOH = 5 ms is reduced by 12% compared with SMCI7 with ZOH = 5 ms but the value of RMSE is increased by 6%. The values of SSE, t_s and OS are comparable for both controllers. It is difficult to select a better one of SMCI7 and DVMPC. With ZOH = 10 ms, the value of SPS is reduced by 42% but the value of SSE is increased by 57%. For DVMPC, the larger value of ZOH might reduce the valve switching frequency but increase steady state error.

For the payload mismatch tests of DVMPC, the OS of the larger payload case is six times of that of the nominal case and other performance metrics are similar. For the smaller payload case, the value of SPS is three times of that of the nominal case and other metrics are increased by 50%. For the larger payload case, the larger inertial may result in the increase of OS. For the smaller payload case, the smaller friction forces than predicted are due to increase of SPS and SSE. The results of payload mismatch tests with SMCI7 are similar to the results with DVMPC.

DVMPC and SMCI7 of the LFC were also simulated. From Tables 5.7.1 and 5.7.6, the value of SPS of DVMPC with ZOH = 5 ms is reduced by 34% compared with SMCI7 with ZOH = 5 ms while the other metrics are similar. For SMCI7, the system has worse performance with ZOH = 10 ms and ZOH = 20 ms. For DVMPC, the value of SPS of ZOH =20 ms case is reduced by 34% compared with ZOH =5 ms case but the value of SSE is twice. For the payload mismatch tests, the OS of the larger payload case is increased and the SPS of smaller payload case is increased, similar to the HFC results.

5.9 Conclusions

The four sliding mode controllers (i.e. SMC3, SMC7, SMCI3 and SMCI7) and DVMPC were simulated with the HFC and the LFC. The robustness of the controllers to payload mismatch was studied.

In the simulations of sliding mode controllers applied to the HFC without ZOH, the SMCI7 produced smaller tracking errors and valve switching in all of four controllers. The additional four modes and integral action were useful. In the simulations of the seven mode controllers applied to the HFC with ZOH, the SMCI7 with ZOH = 5 ms outperformed the other controllers with smaller SPS and SSE. The results indicated that ZOH of 5 ms helped to reduce the valve switching frequency. In the simulation of

DVMPC and SMCI7 for the nominal case, the results were comparable. In the payload mismatch tests, the results of DVMPC and SMCI7 were also similar.

In the simulations of DVMPC and SMCI7 applied to the LFC, DVMPC was superior. It produced a lower valve switching frequency, while it maintained similar values for the other metrics. With larger values of ZOH, the values of SPS were smaller with DVMPC.

CHAPTER 6 EXPERIMENTS

6.1 Introduction

The DVMPC and two kinds of sliding mode controllers with integral action were designed in chapter 4. The proposed controllers were studied and compared through simulations in chapter 5. In this chapter, experiments will be performed on the HFC with the proposed sliding mode controllers (*i.e.*, SMCI3 and SMCI7) and the existing controllers (*i.e.*, SMC3 and SMC7); and the results compared. Next, robustness experiments will be performed for mismatched payloads. The LFC was not available for performing experiments. The possibility of testing DVMPC experimentally will be discussed at the end of the chapter.

6.2 Sliding mode controllers without ZOH

In this section, the four sliding mode controllers (SMC3, SMC7, SMCI3 and SMCI7) without ZOH were tested on the HFC system.

6.2.1 Sliding mode controllers with nominal mass

The four sliding mode controllers were tuned with the nominal moving mass $M = 2.14\text{kg}$. Each test was performed five times. The performance metrics were averaged from five experiments and are listed in Tables 6.2.1 – 6.2.4. The experimental results are shown in Figures 6.2.1 – 6.2.4.

Table 6.2.1 Comparison of performance metrics for HFC with SMC controllers without ZOH in experiments.

Controller	RMSE (mm)	SPS	SSE (mm)	t_s (s)	OS (mm)
SMC3	62.14	17.85	0.35	0.40	7.99
SMC7	63.95	14.60	0.33	0.44	6.20
SMCI3	60.98	12.20	0.17	0.34	2.78
SMCI7	61.18	9.65	0.19	0.34	3.28

Table 6.2.2 Comparison of SSE values (mm) for HFC with SMC controllers without ZOH in experiments.

Controller	SSE_1	SSE_2	SSE_3	SSE_4	SSE
SMC3	0.34	0.38	0.35	0.32	0.35
SMC7	0.30	0.20	0.44	0.37	0.33
SMCI3	0.06	0.20	0.24	0.17	0.17
SMCI7	0.05	0.21	0.26	0.25	0.19

Table 6.2.3 Comparisons of t_s values (s) for HFC with SMC controllers without ZOH in experiments.

Controller	t_{s1}	t_{s2}	t_{s3}	t_{s4}	t_s
SMC3	0.50	0.53	0.37	0.21	0.40
SMC7	0.54	0.58	0.35	0.29	0.44
SMCI3	0.38	0.40	0.37	0.21	0.34
SMCI7	0.37	0.41	0.37	0.21	0.34

Table 6.2.4 Comparisons of OS values (mm) for HFC with SMC controllers without ZOH in experiments.

Controller	OS_1	OS_2	OS_3	OS_4	OS
SMC3	22.78	1.76	4.66	2.80	7.99
SMC7	17.10	3.05	3.54	1.10	6.20
SMCI3	8.69	0.08	0.36	1.98	2.78
SMCI7	9.45	0.03	0.59	3.04	3.28

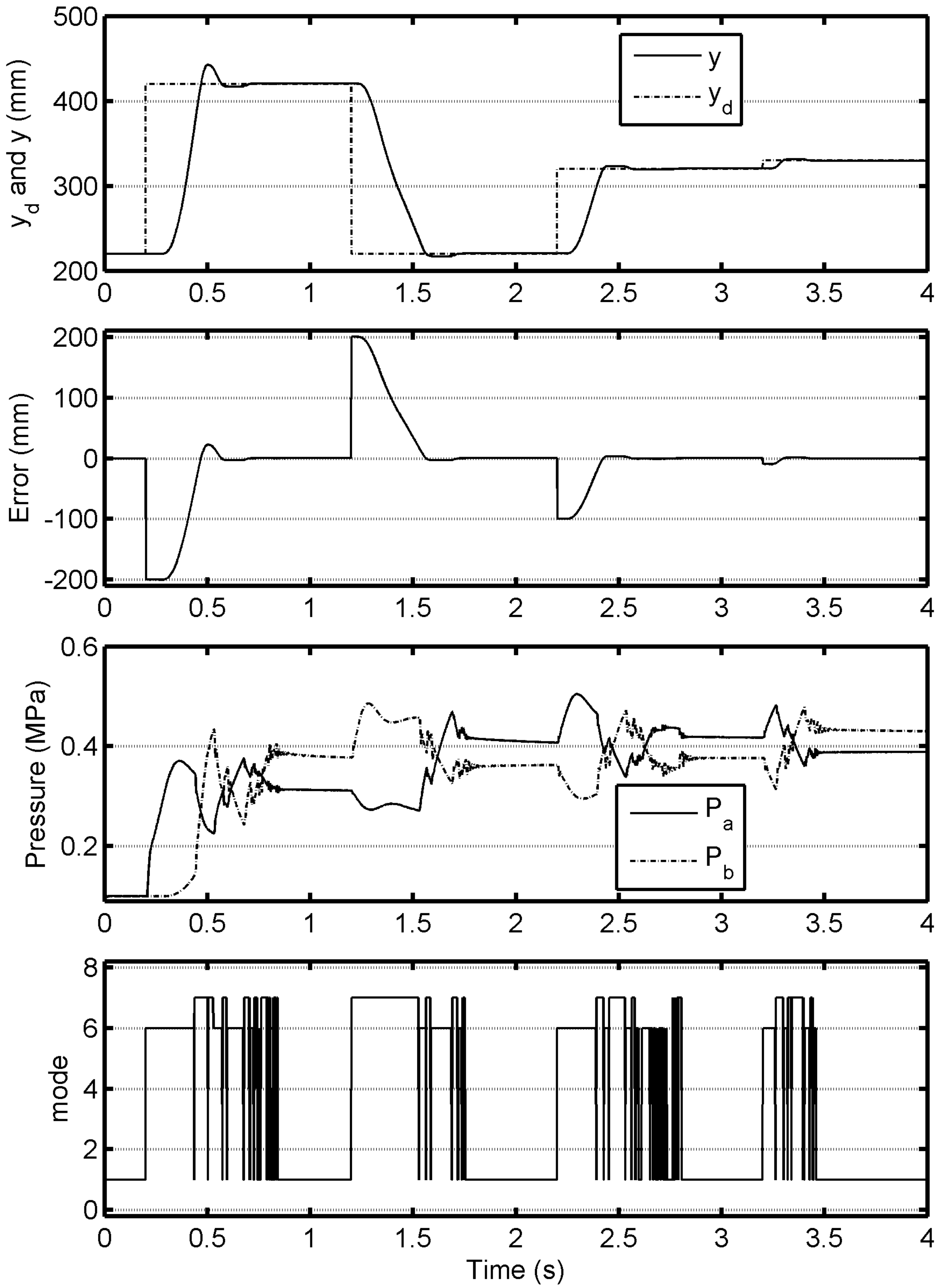

Figure 6.2.1 Experiment on the HFC with SMC3, without ZOH and with M = 2.14 kg

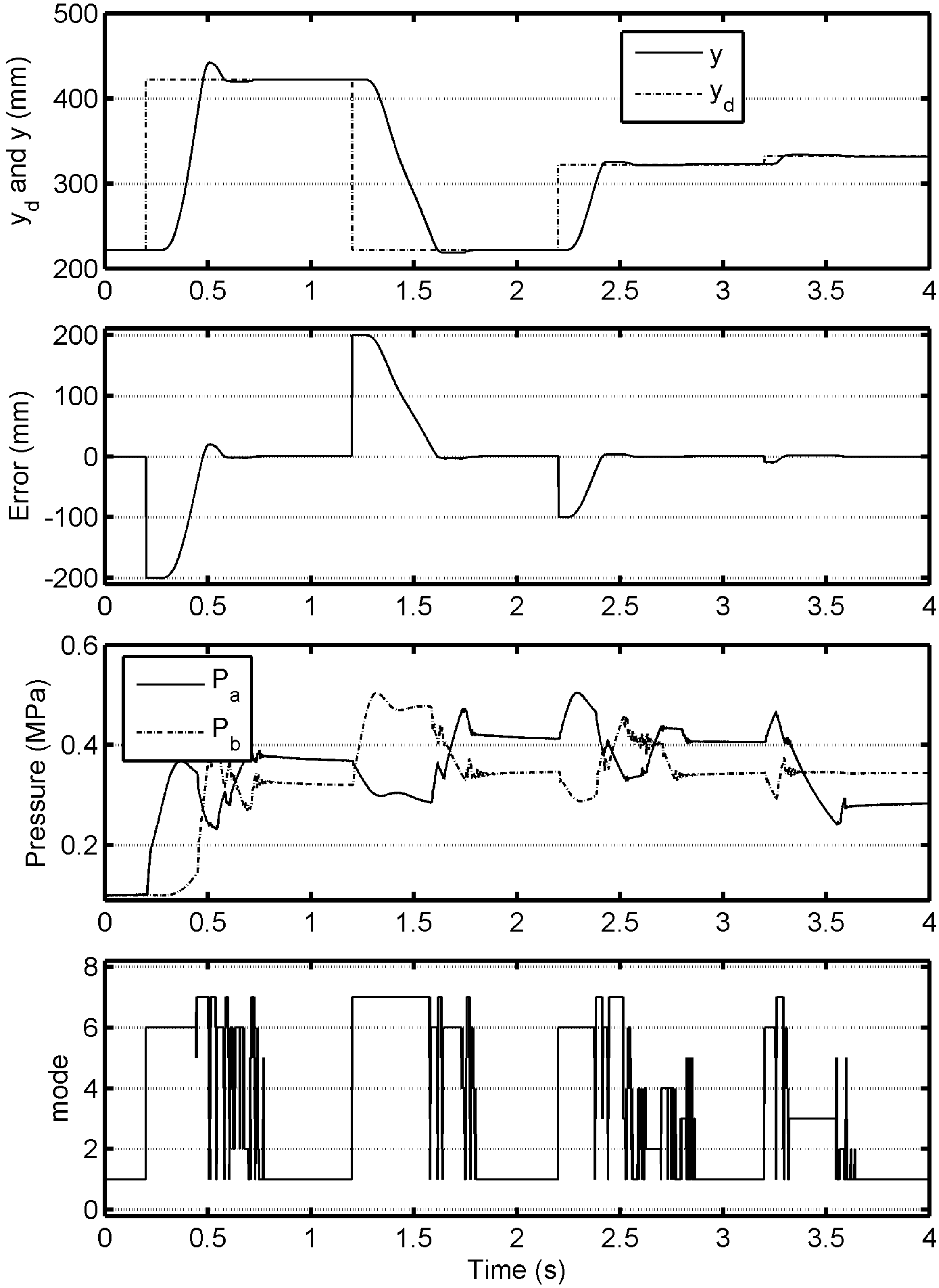

Figure 6.2.2 Experiment on the HFC with SMC7, without ZOH and with M = 2.14 kg

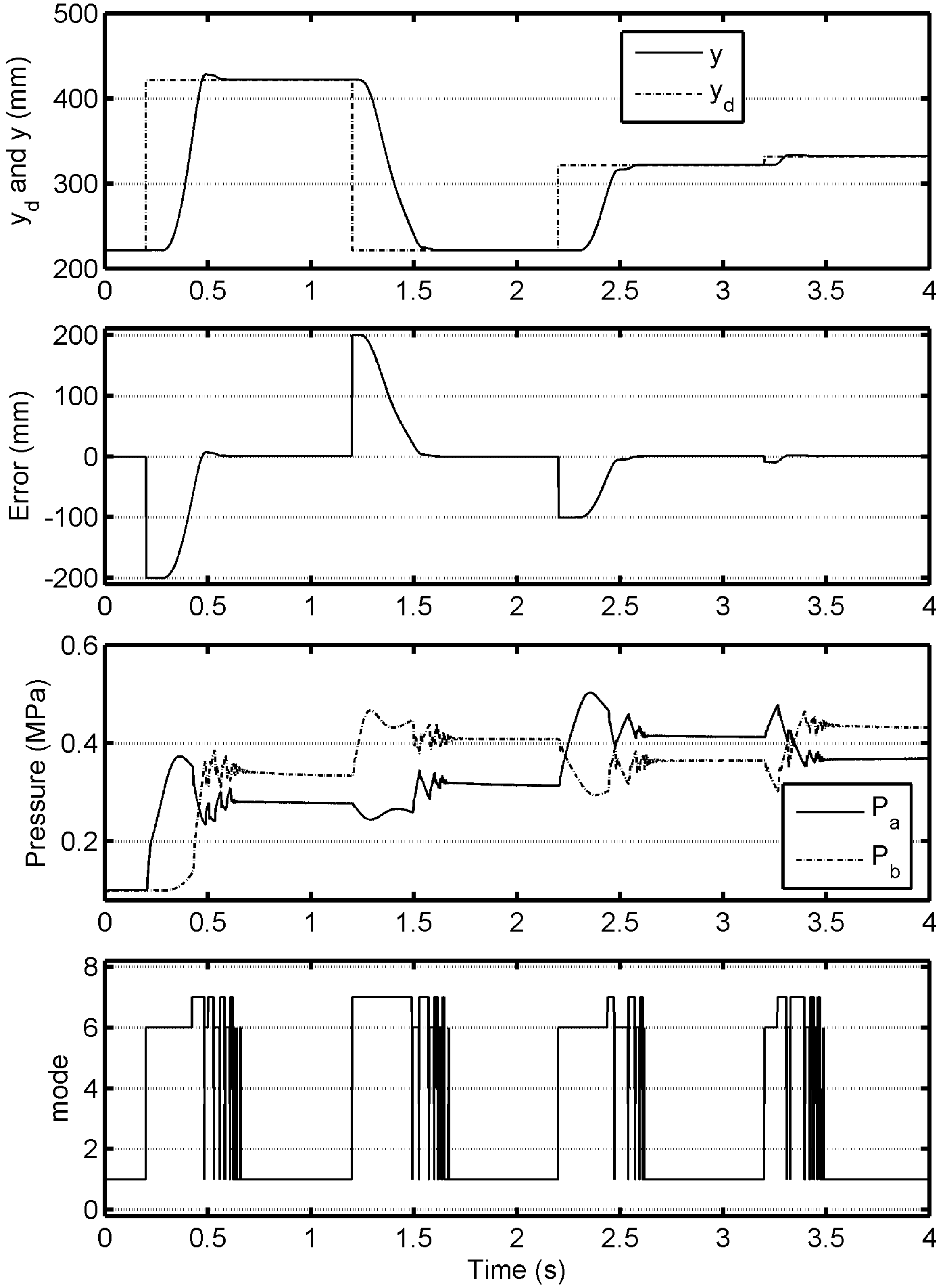

Figure 6.2.3 Experiment on the HFC with SMCI3, without ZOH and with M = 2.14 kg

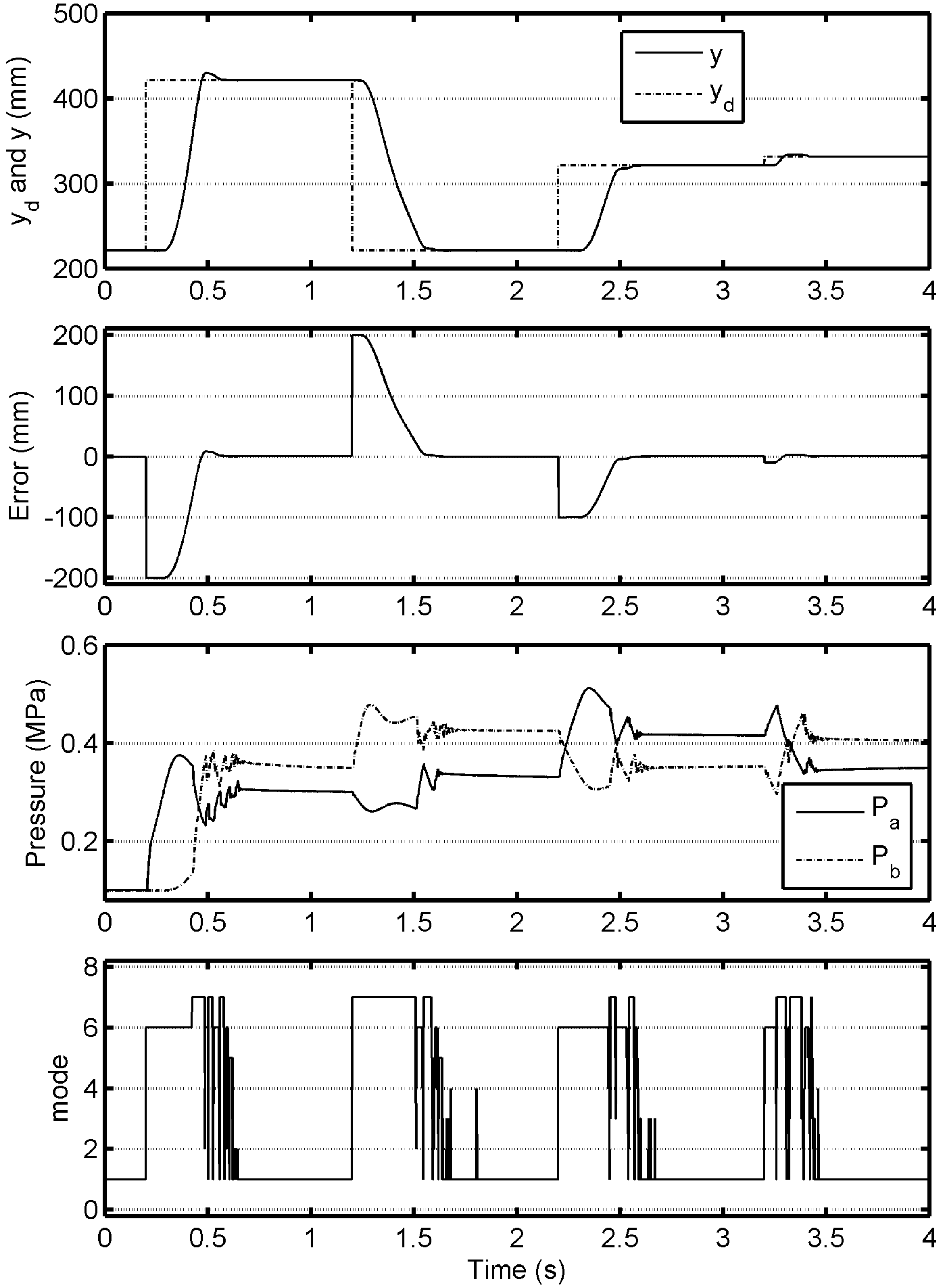

Figure 6.2.4 Experiment on the HFC with SMCI7, without ZOH and with M = 2.14 kg

From Table 6.2.1, the SPS of SMC7 is 18% smaller than that of SMC3 and the SPS of SMCI7 is 21% smaller than that of SMCI3. The reduction of SPS is due to additional four discrete modes. The SPS of SMCI3 is reduced by 37% comparing SMC3 and that of SMCI7 is reduced by 34% comparing SMCI3, which is caused by integral action. Compared with SMC3, the SPS of SMCI7 is reduced by 48%. SMCI3 and SMCI7 produce the similar value of SSE and RMSE. Compared with SMC3, the average SSE of SMCI7 is reduced by 46%, mainly because of integral action. The SSE of SMCI7 is in the range of ±0.3 *mm* and the average SSE for four steps is less than ±0.2 *mm*. In comparison of SMC3, the t_s and OS of SMCI7 are reduced by 15% and 59%, respectively. Thus, SMCI7 achieves better tracking performance than SMC.

The main difference between experiment and simulation is that the values of OS are larger in the experiment. This might be due to imperfect friction model. The friction forces in the model are based on velocity and pressures. In reality, the friction forces are more complex and related to the positions or other factors. The noises of pressure sensors and encoder might also contribute to the difference.

6.2.2 Sliding mode controllers with payload mismatch

In this subsection, we examine the robustness of the four sliding mode controllers without ZOH. The four sliding mode controllers were tuned with the nominal moving mass $M = 2.14\text{kg}$. With the controller gains fixed, tests were performed with the smaller mass $M = 0.95\text{kg}$ and the larger mass $M = 3.24\text{kg}$. Each test was performed five times. The average performance metrics are listed in Tables 6.2.5 – 6.2.8. In the experiments, all the controllers were still stable with the increased payload and decreased payload. With a decrease in *M* of 56%, the tracking performance was even better than that of the nominal moving mass. For example, RMSE, SSE, t_s and OS of the smaller case payload are 8%, 15%, 5% and 39% smaller than those of the nominal one for the SMC7. For the increased payload, the OS values for the four controllers were obviously increased. The OS of SMCI7 was increased by 101%. Even with the increased *M*, SMCI3 and SMCI7 still produced only half the OS of SMC3 and SMC7. Other performance metrics like SSE, SPS and t_s were not obviously changed due to the increased payload.

Table 6.2.5 Comparisons of performance metrics for HFC with SMC controllers and payload mismatch in experiments.

Controller	Mass (kg)	RMSE (mm)	SPS	SSE (mm)	t_s (s)	OS (mm)
SMC3	2.14	62.14	17.85	0.35	0.40	7.99
SMC3	0.95	59.82	19.50	0.21	0.34	2.87
SMC3	3.24	64.10	20.35	0.26	0.45	12.53
SMC7	2.14	63.95	14.60	0.33	0.44	6.20
SMC7	0.95	58.64	16.03	0.28	0.42	2.43
SMC7	3.24	63.17	18.60	0.40	0.47	12.77
SMCI3	2.14	60.98	11.20	0.15	0.34	2.78
SMCI3	0.95	62.68	14.05	0.17	0.35	0.78
SMCI3	3.24	66.79	11.65	0.21	0.38	6.61
SMCI7	2.14	61.18	9.65	0.19	0.34	3.28
SMCI7	0.95	62.76	11.88	0.20	0.35	1.14
SMCI7	3.24	67.29	8.55	0.17	0.38	6.60

Table 6.2.6 Comparisons of SSE values (mm) for HFC with SMC controllers and payload mismatch in experiments.

Controller	Mass (kg)	SSE_1	SSE_2	SSE_3	SSE_4	SSE
SMC3	2.14	0.34	0.38	0.35	0.32	0.35
SMC3	0.95	0.19	0.13	0.24	0.26	0.21
SMC3	3.24	0.24	0.27	0.24	0.3	0.26
SMC7	2.14	0.30	0.20	0.44	0.37	0.33
SMC7	0.95	0.42	0.17	0.19	0.35	0.28
SMC7	3.24	0.36	0.37	0.47	0.38	0.40
SMCI3	2.14	0.06	0.21	0.21	0.12	0.15
SMCI3	0.95	0.06	0.20	0.24	0.17	0.17
SMCI3	3.24	0.10	0.29	0.35	0.11	0.21
SMCI7	2.14	0.05	0.21	0.26	0.25	0.19
SMCI7	0.95	0.06	0.35	0.11	0.28	0.20
SMCI7	3.24	0.07	0.20	0.30	0.10	0.17

Table 6.2.7 Comparisons of t_s values (s) for HFC with SMC controllers and payload mismatch in experiments.

Controller	Mass (kg)	t_{s1}	t_{s2}	t_{s3}	t_{s4}	t_s
SMC3	2.14	0.50	0.53	0.37	0.21	0.40
SMC3	0.95	0.38	0.52	0.33	0.13	0.34
SMC3	3.24	0.60	0.55	0.45	0.22	0.45
SMC7	2.14	0.54	0.58	0.35	0.29	0.44
SMC7	0.95	0.48	0.59	0.46	0.16	0.42
SMC7	3.24	0.57	0.56	0.48	0.28	0.47
SMCI3	2.14	0.38	0.39	0.36	0.21	0.34
SMCI3	0.95	0.38	0.40	0.37	0.20	0.35
SMCI3	3.24	0.50	0.45	0.32	0.23	0.38
SMCI7	2.14	0.37	0.41	0.37	0.21	0.34
SMCI7	0.95	0.38	0.46	0.36	0.21	0.35
SMCI7	3.24	0.50	0.46	0.30	0.24	0.38

Table 6.2.8 Comparisons of OS values (mm) for HFC with SMC controllers and payload mismatch in experiments.

Controller	Mass (kg)	OS_1	OS_2	OS_3	OS_4	OS
SMC3	2.14	22.78	1.76	4.66	2.80	7.99
SMC3	0.95	5.95	0.77	2.96	1.79	2.87
SMC3	3.24	37.33	4.38	6.75	1.76	12.53
SMC7	2.14	17.10	3.05	3.54	1.10	6.20
SMC7	0.95	5.26	1.75	1.76	0.95	2.43
SMC7	3.24	36.28	4.12	8.58	2.12	12.77
SMCI3	2.14	8.69	0.08	0.36	1.98	2.78
SMCI3	0.95	0.40	0.05	0.46	2.20	0.78
SMCI3	3.24	22.90	0.27	0.63	2.65	6.61
SMCI7	2.14	9.45	0.03	0.59	3.04	3.28
SMCI7	0.95	0.79	0.07	0.85	2.87	1.14
SMCI7	3.24	23.32	0.20	0.44	2.42	6.60

6.3 Sliding mode controllers with ZOH

In the chapter 5, we demonstrated that ZOH could help the reduction of the valve switching frequency without significantly increased tracking errors in simulations. With ZOH = 5 ms, the tracking performance was satisfactory. In this section, the four sliding mode controllers will be experimentally tested with ZOH = 5 ms. First we test the system with nominal moving mass $M = 2.14\text{kg}$, then we test the robustness of the system with the smaller mass $M = 0.95\text{kg}$ and with the larger mass $M = 3.24\text{kg}$.

6.3.1 Sliding mode controllers with ZOH = 5 ms and nominal mass

In this subsection, the four sliding mode controllers were tested with ZOH = 5 ms using the nominal moving mass $M = 2.14\text{kg}$. The control parameters were same as those used in section 6.3 without ZOH. Each test was performed five times. The average results for five experiments are listed in Tables 6.3.1 – 6.3.4. Figures 6.3.1 – 6.3.4 show the tracking performance.

As in section 6.2.1, SMCI7 achieved the smallest SPS among the four sliding mode controllers. Compared with SMC3, the SPS of SMCI7 is reduced by 36%. The SSE and t_s of SMCI7 are smallest among the four sliding mode controllers. The SSE and t_s of SMCI7 are 10% and 14% smaller than those SMC3. The largest SSE of SMCI7 is within ±0.3 mm and the average SSE for four steps is less than ±0.2 mm. The OS of SMCI7 is reduced by 42% comparing SMC3. Thus, SMCI7 achieves the best tracking performance among the four controllers with ZOH = 5 ms.

Comparing the results without ZOH to those with ZOH = 5 ms, the SPS of SMCI7 was reduced by 32%. The SSE of SMCI7 was not changed with the addition of ZOH. The OS of SMCI7 was increased by 32% due to the ZOH. Because of the increased OS, the t_s of SMCI7 was increased by 11%. For SMC3 and SMC7, the SPS was reduced by 42% and 50%, respectively, due to the ZOH. The values of SSE, t_s and OS were not obviously changed. Thus, ZOH = 5 ms helped to reduce the valve switching frequency without a significant loss of tracking performance.

Table 6.3.1 Comparisons of performance metrics for HFC with SMC controllers with ZOH = 5 ms in experiments.

Controller	RMSE (mm)	SPS	SSE (mm)	t_s (s)	OS (mm)
SMC3	62.00	10.35	0.21	0.44	8.20
SMC7	61.30	7.33	0.31	0.44	9.19
SMCI3	63.34	9.40	0.26	0.38	4.62
SMCI7	63.07	6.60	0.19	0.38	4.79

Table 6.3.2 Comparisons of SSE values (mm) for HFC with SMC controllers with ZOH = 5 ms in experiments.

Controller	SSE_1	SSE_2	SSE_3	SSE_4	SSE
SMC3	0.28	0.15	0.15	0.26	0.21
SMC7	0.29	0.29	0.30	0.36	0.31
SMCI3	0.30	0.35	0.25	0.13	0.26
SMCI7	0.12	0.30	0.15	0.17	0.19

Table 6.3.3 Comparisons of t_s values (s) for HFC with SMC controllers with ZOH = 5 ms in experiments.

Controller	t_{s1}	t_{s2}	t_{s3}	t_{s4}	t_s
SMC3	0.53	0.53	0.42	0.28	0.44
SMC7	0.49	0.55	0.43	0.30	0.44
SMCI3	0.46	0.35	0.35	0.25	0.38
SMCI7	0.36	0.45	0.45	0.25	0.38

Table 6.3.4 Comparisons of OS values (mm) for HFC with SMC controllers with ZOH = 5 ms in experiments.

Controller	OS_1	OS_2	OS_3	OS_4	OS
SMC3	24.51	2.43	3.50	2.37	8.20
SMC7	26.69	2.95	4.68	2.43	9.19
SMCI3	15.02	0.57	0.78	2.10	4.62
SMCI7	14.77	0.05	1.35	2.97	4.79

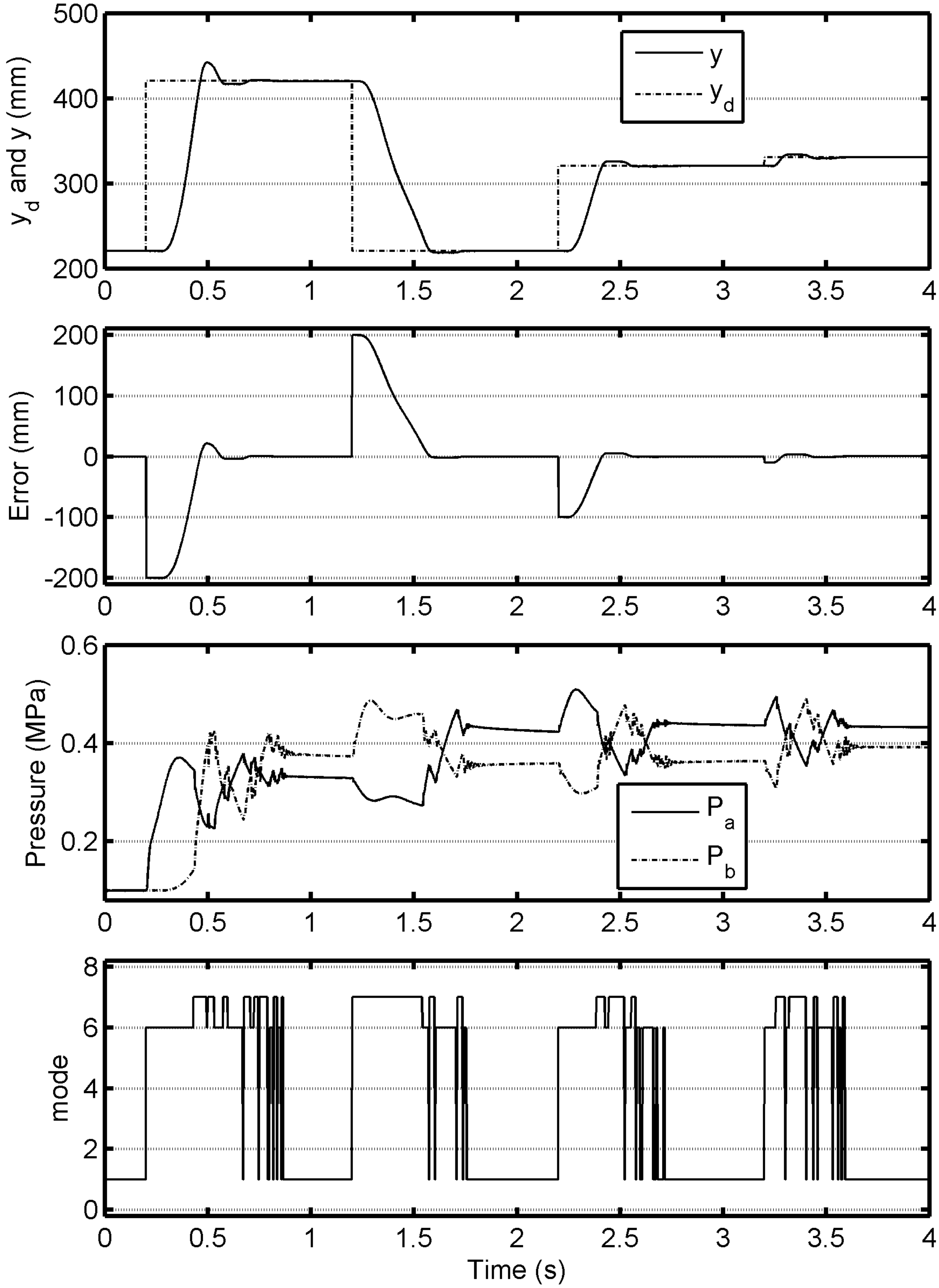

Figure 6.3.1 Experiment on the HFC with SMC3, ZOH=5 ms and M = 2.14 kg

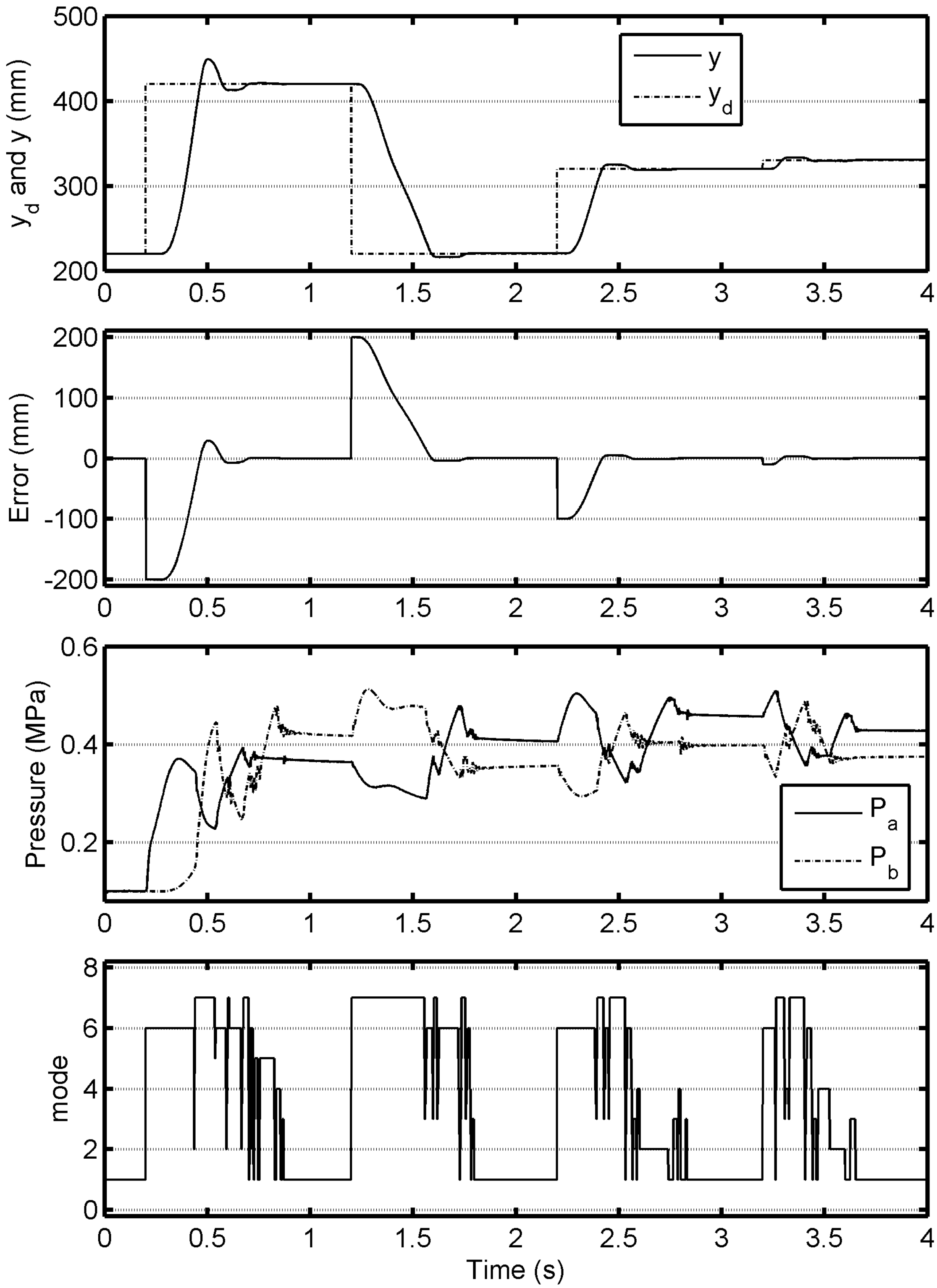

Figure 6.3.2 Experiment on the HFC with SMC7, ZOH=5 ms and M = 2.14 kg

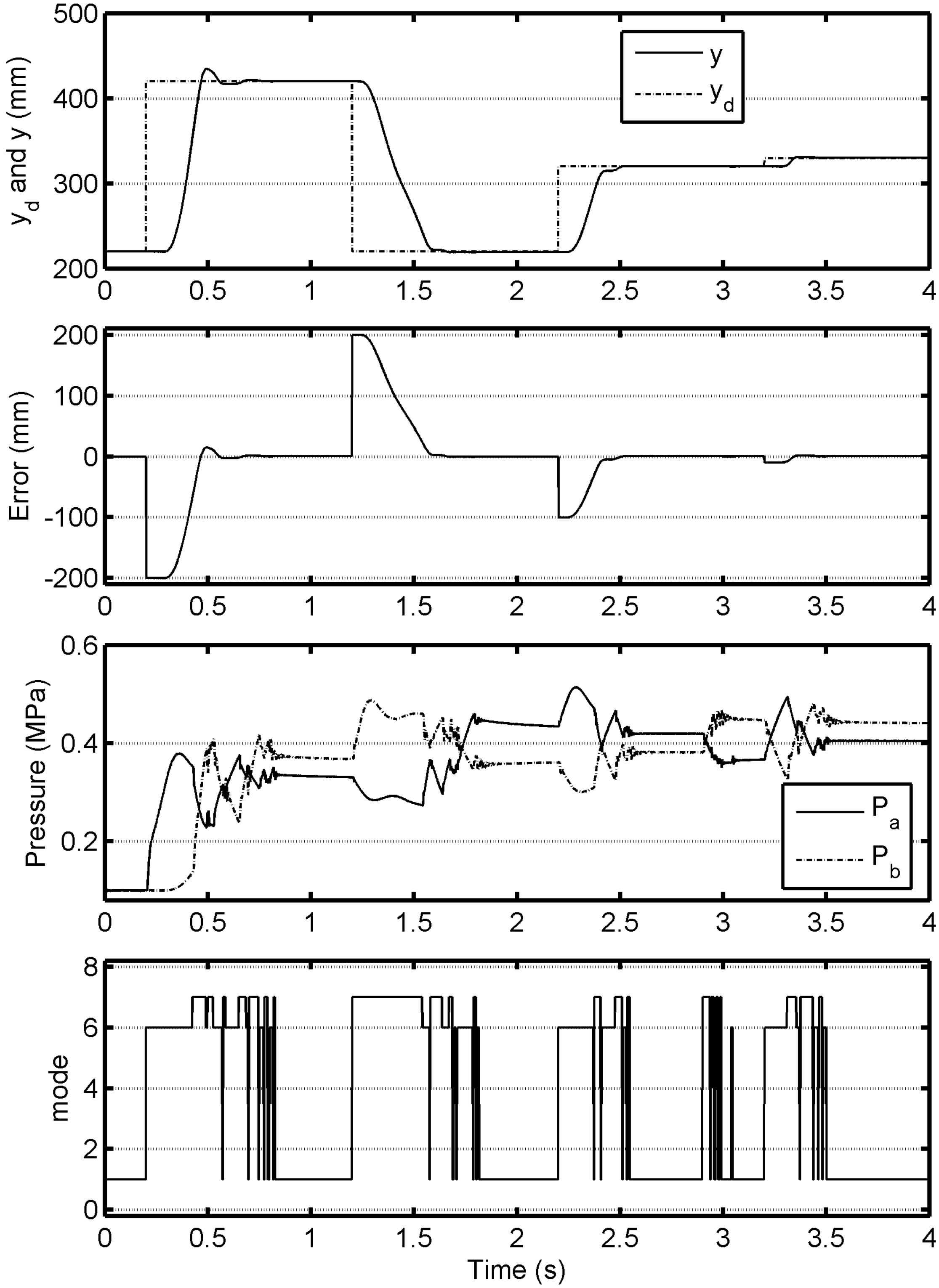

Figure 6.3.3 Experiment on the HFC with SMCI3, ZOH=5 ms and M = 2.14 kg

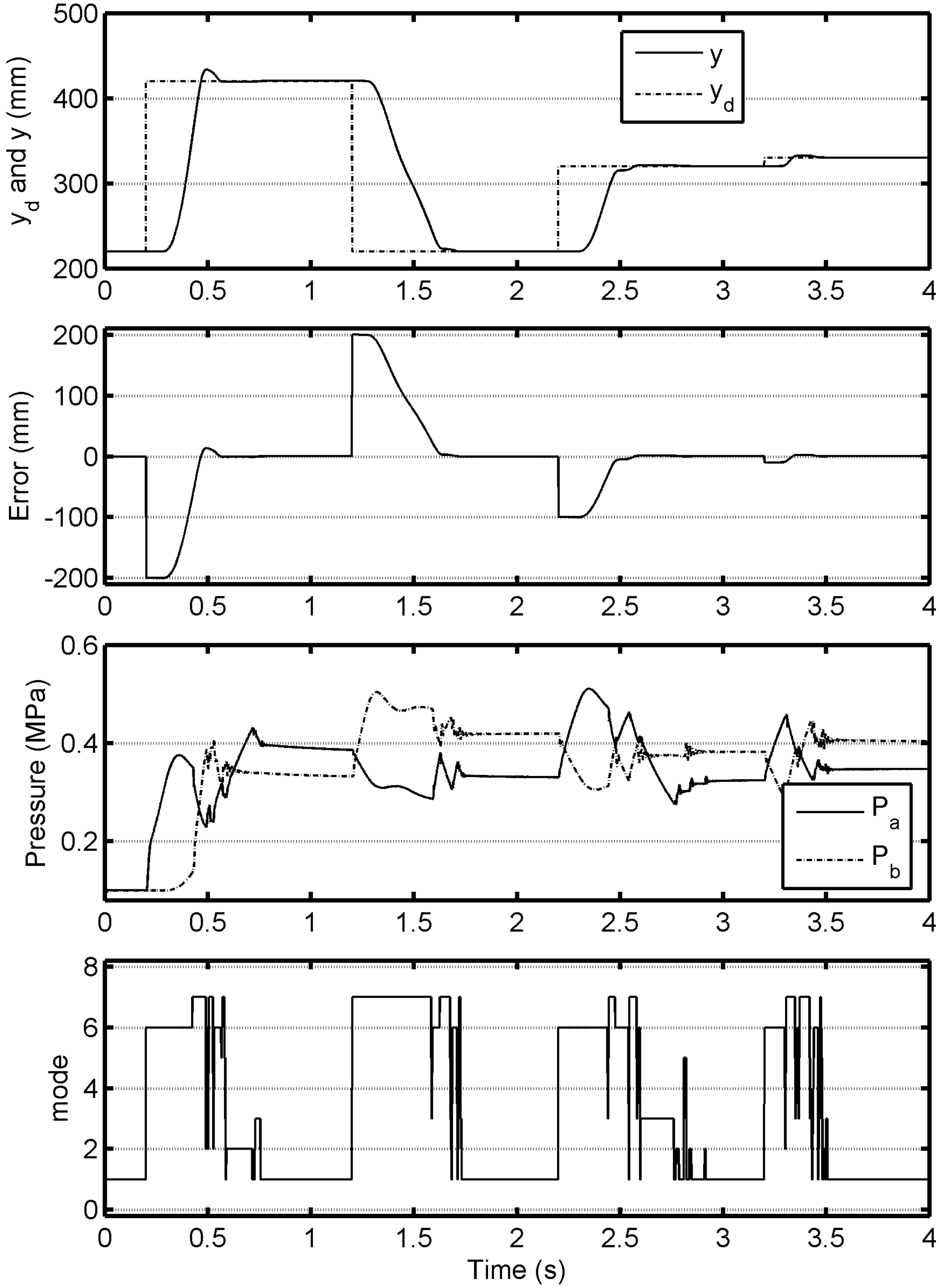

Figure 6.3.4 Experiment on the HFC with SMCI7, ZOH=5 ms and M = 2.14 kg

6.3.2 Sliding mode controllers with payload mismatch

The four sliding mode controllers with ZOH = 5 ms were tuned with the nominal moving mass $M = 2.14\text{kg}$ used in the previous subsection. With the controller gains fixed, tests were performed with the smaller mass $M = 0.95\text{kg}$ and the larger mass $M = 3.24\text{kg}$. Each test was performed five times. The average performance metrics are listed in Tables 6.3.5 – 6.3.8. In the experiments, all the controllers remained stable with the increased payload and decreased payload. SMCI7 produced the best tracking performance in the robustness tests, with small SPS, SSE, t_s and OS.

Table 6.3.5 Comparisons of performance metrics for SMC of the HFC with ZOH = 5 ms and payload mismatch in experiments.

Controller	Mass (kg)	RMSE (mm)	SPS	SSE (mm)	t_s (s)	OS (mm)
SMC3	2.14	62.00	10.35	0.21	0.44	8.20
SMC3	0.95	59.52	9.75	0.21	0.36	2.55
SMC3	3.24	65.57	10.40	0.18	0.52	14.93
SMC7	2.14	61.30	7.33	0.31	0.44	9.19
SMC7	0.95	61.34	7.55	0.24	0.44	2.04
SMC7	3.24	65.85	7.73	0.44	0.54	13.65
SMCI3	2.14	63.34	9.40	0.26	0.38	4.62
SMCI3	0.95	59.71	9.45	0.29	0.32	1.00
SMCI3	3.24	65.76	6.35	0.18	0.39	7.83
SMCI7	2.14	63.07	6.60	0.19	0.38	4.79
SMCI7	0.95	62.34	7.13	0.15	0.34	0.65
SMCI7	3.24	64.66	5.60	0.18	0.40	8.08

Table 6.3.6 Comparisons of SSE values (mm) for SMC of the HFC with ZOH = 5 ms and payload mismatch in experiments.

Controller	Mass (kg)	SSE_1	SSE_2	SSE_3	SSE_4	SSE
SMC3	2.14	0.28	0.15	0.15	0.26	0.21
SMC3	0.95	0.19	0.14	0.24	0.28	0.21
SMC3	3.24	0.16	0.27	0.16	0.13	0.18
SMC7	2.14	0.29	0.29	0.30	0.36	0.31
SMC7	0.95	0.21	0.23	0.29	0.22	0.24
SMC7	3.24	0.48	0.58	0.39	0.29	0.44
SMCI3	2.14	0.30	0.35	0.25	0.13	0.26
SMCI3	0.95	0.31	0.27	0.40	0.16	0.29
SMCI3	3.24	0.23	0.08	0.25	0.15	0.18
SMCI7	2.14	0.12	0.31	0.15	0.17	0.19
SMCI7	0.95	0.08	0.13	0.23	0.16	0.15
SMCI7	3.24	0.31	0.14	0.08	0.20	0.18

Table 6.3.7 Comparisons of t_s values (s) for SMC of the HFC with ZOH = 5 ms and payload mismatch in experiments.

Controller	Mass (kg)	t_{s1}	t_{s2}	t_{s3}	t_{s4}	t_s
SMC3	2.14	0.53	0.53	0.42	0.28	0.44
SMC3	0.95	0.48	0.44	0.35	0.18	0.36
SMC3	3.24	0.64	0.62	0.51	0.30	0.52
SMC7	2.14	0.49	0.55	0.43	0.30	0.44
SMC7	0.95	0.45	0.63	0.46	0.23	0.44
SMC7	3.24	0.65	0.66	0.56	0.28	0.54
SMCI3	2.14	0.46	0.35	0.35	0.25	0.38
SMCI3	0.95	0.35	0.43	0.33	0.19	0.32
SMCI3	3.24	0.51	0.41	0.37	0.25	0.39
SMCI7	2.14	0.36	0.45	0.45	0.25	0.38
SMCI7	0.95	0.37	0.47	0.33	0.21	0.34
SMCI7	3.24	0.53	0.48	0.34	0.24	0.40

Table 6.3.8 Comparisons of OS values (mm) for SMC of the HFC with ZOH = 5 ms and payload mismatch in experiments.

Controller	Mass (kg)	OS_1	OS_2	OS_3	OS_4	OS
SMC3	2.14	24.51	2.43	3.50	2.37	8.20
SMC3	0.95	6.53	1.15	1.59	0.92	2.55
SMC3	3.24	41.96	4.13	9.30	4.32	14.93
SMC7	2.14	26.69	2.95	4.68	2.43	9.19
SMC7	0.95	3.83	1.42	1.67	1.23	2.04
SMC7	3.24	37.06	4.53	9.66	3.36	13.65
SMCI3	2.14	15.02	0.57	0.78	2.10	4.62
SMCI3	0.95	0.77	0.15	0.81	2.26	1.00
SMCI3	3.24	26.20	0.11	1.57	3.43	7.83
SMCI7	2.14	14.77	0.05	1.35	2.97	4.79
SMCI7	0.95	0.02	0.81	0.02	1.74	0.65
SMCI7	3.24	26.73	0.55	0.85	4.20	8.08

6.4 DVMPC

In chapter 5, DVMPC simulation results were presented for the HFC and LFC. In this section, we will discuss the possibility of implementing DVMPC experimentally. The same DVMPC parameters as section 5.5 are used here.

The DVMPC algorithm was implemented as described in section 4.4 using the hardware described in section 3.3. The maximum calculation time and mean calculation time are listed in Table 6.4.1. For ZOH = 5 ms, the max. time was 8 ms and the mean time was 2.75 ms which means the DVMPC would occasionally exceed the ZOH and the controller would fail in an experiment. For ZOH = 10 ms, the max. time was 7 ms so the controller could be used in an experiment. Of course, if we use a faster computer the calculation time can be decreased. These results demonstrate that DVMPC can be implemented experimentally. Unfortunately there was insufficient time to continue this research.

Table 6.4.1 DVMPC calculation times for the HFC.

ZOH (ms)	N_p	Max. DVMPC calc. time (ms)	Max. DVMPC calc. time (ms)
5	15	8	2.75
10	10	7	1.40

6.5 Conclusion

The four sliding mode controllers were experimentally tested. The experiments demonstrated that the tracking performance of the two proposed sliding mode controllers (*i.e.*, SMCI3 and SMCI7) were better than the existing ones. The proposed controllers also reduced the valve switching frequency. Using a 5 ms ZOH the valve switching frequency can be further reduced without significant loss of tracking performance. Regarding robustness, both the SMCI3 and SMCI7 remained stable when subjected to an increase and decrease of the payload relative to its nominal value. The DVMPC calculation times were measured and demonstrated that experimental implementation of DVMPC is possible.

CHAPTER 7 CONCLUSIONS

7.1 Summary

In this research, the modeling and control of a pneumatic actuator based on on/off solenoid valves was presented. Sliding-mode control and model-predictive control algorithms were compared. A mass flow rate model for discrete valve input was derived. A novel friction model based on velocity and pressure was proposed. The system model was validated by comparing simulation and experiment results. Two classes of nonlinear control algorithms, based on sliding-mode control and model-predictive control respectively, were designed, tested and compared. The simulation and experimental results demonstrated the robustness and generality of the control strategies.

7.2 Achievements

The main achievements of this thesis are summarized as follows.

(1) This research compared sliding-mode control and model-predictive control for pneumatic cylinders. It demonstrated the feasibility of model-predictive control for pneumatic actuators to reduce tracking errors and valve switching frequency.

(2) A new friction model was presented to capture the characteristics of pneumatic cylinders. The friction forces were shown to depend on velocity and the difference between chambers' pressure. This friction model was validated by comparing simulation and experimental results. The values of R^2 for the positive and negative directions were increased by 98% and 80%, respectively, compared with the classical friction model.

(3) Two new sliding mode controllers with integral action were proposed. The experiments demonstrated that the tracking performance of the two proposed sliding mode controllers (*i.e.*, SMCI3 and SMCI7) were better than the existing ones. Compared with the SMC3, the valve switching frequency of SMCI7 was reduced by 46%. With the zero-order hold, the switching activity was further reduced by 32%.

(4) A novel DVMPC algorithm was developed. It was able to reduce the valve switching frequency in the comparison of the proposed SMC algorithms without sacrificing the position control performance.

(5) SMC and DVMPC algorithms were compared. All five controllers were simulated on a high friction cylinder and a low friction cylinder to demonstrate their generality. DBMPC had better performance on the low friction cylinder. The parameters of DVMPC can also be tuned to meet different control requirements, such as less SPS or less SSE.

(6) Regarding robustness, both the SMCI3 and SMCI7 remained stable when subjected to an increase and decrease of the payload relative to its nominal value

7.3 Recommendations for future work

(1) The accuracy of the friction model has a big effect on the tracking performance, especially with the high friction cylinder. Comparing simulation and experiment results, it was apparent that the friction forces not only depend on the velocity and chambers' pressures, but also are related to the position. However, the friction model could become very complex if the positions are considered.

(2) The components of cost function in model-predictive control can be changed to meet the control requirements. Adding integral action or acceleration might improve the tracking performance.

(3) Experimental implementation of DVMPC can be performed. The DVMPC calculation times were measured and demonstrated that experimental implementation of DVMPC is possible.

(4) A method for automatically tuning the parameters of SMC and DVMPC should be developed. The values of parameters determine the performance of the closed-loop system. It is difficult to obtain the best combinations by manually tuning.

REFERENCES

Ahn, K. and Yokota, S. (2005). Intelligent switching control of pneumatic actuator using on/off solenoid valves, *Mechatronics*, 15 (6), 683-702.

Armstrong-Hélouvry, B., Dupont, P. and De Wit, C. C. (1994). A survey of models, analysis tools and compensation methods for the control of machines with friction. *Automatica*, *30*(7), 1083-1138.

Aziz, S., and Bone, G. M. (1998). Automatic tuning of pneumatic servo actuators. *Advanced Robotics*, *13*(6), 563-576.

Ballard, R. L. (1974). The dynamic characteristics of pneumatic actuator and valve systems. Ph.D. thesis, University of Bath

Bone, G. M. and Chen, X. (2012). Position control of hybrid pneumatic-electric actuators, *2012 American Control Conference (ACC)*, 1793-99.

Bone, G. M., Xue, M. and Flett, J. (2015). Position control of hybrid pneumatic–electric actuators using discrete-valued model-predictive control. *Mechatronics*, *25*, 1-10.

Bobrow, J. E., and McDonell, B. W. (1998). Modeling, identification, and control of a pneumatically actuated, force controllable robot. *Robotics and Automation*', *IEEE Transactions on*, *14*(5), 732-742.

Carneiro, J. F., and de Almeida, F. G. (2006). Reduced-order thermodynamic models for servo-pneumatic actuator chambers. *Proceedings of the Institution of Mechanical Engineers, Part I: Journal of Systems and Control Engineering*,*220*(4), 301-314.

Carneiro, J. F. and de Almeida, F. G. (2012). A neural network based nonlinear model of a servopneumatic system, *Journal of Dynamic Systems Measurement and Control-Transactions of the ASME,* 134 (2).

Dahl, P. R. (1968). A solid friction model (No. TOR-0158 (3107-18)-1), The Aerospace Corporation, El Segundo, CA.

Daugherty, R. L., & Franzini, J. B. (1975). *Fluid mechanics with engineering applications*. Tata McGraw-Hill Education.

De Wit, C. C., Olsson, H., Astrom, K. J., & Lischinsky, P. (1995). A new model for control of systems with friction. *Automatic Control, IEEE Transactions on*,*40*(3), 419-425.

Geleževičius, V., & Grigaitis, A. (2015). Investigation of dynamic behaviour of nonlinear electropneumatic acting system. *Elektronika ir Elektrotechnika, 68*(4), 35-40.

Grancharova, A., & Johansen, T. (2011). Design and comparison of explicit model predictive controllers for an electropneumatic clutch actuator using on/off valves. *Mechatronics, IEEE/ASME Transactions on, 16*(4), 665-673.

Hodgson, S., Le, M. Q., Tavakoli, M., & Pham, M. T. (2012). Improved tracking and switching performance of an electro-pneumatic positioning system, *Mechatronics*, 22 (1), 1-12.

Hodgson, S., Tavakoli, M., Pham, M. T., and Leleve, A. (2015). Nonlinear Discontinuous Dynamics Averaging and PWM-Based Sliding Control of Solenoid-Valve Pneumatic Actuators. *Mechatronics, IEEE/ASME Transactions on*, *20*(2), 876-888.

Jouppila, V. T., Gadsden, S. A., Bone, G. M., Ellman, A. U. and Habibi, S. R. (2014). Sliding mode control of a pneumatic muscle actuator system with a PWM strategy. *International Journal of Fluid Power*, *15*(1), 19-31.

Langjord, H., & Johansen, T. A. (2010). Dual-mode switched control of an electropneumatic clutch actuator. *Mechatronics, IEEE/ASME Transactions on,15*(6), 969-981.

Linnett, J. A., & Smith, M. C. (1989). An accurate low-friction pneumatic position control system. *Proceedings of the Institution of Mechanical Engineers, Part B: Journal of Engineering Manufacture*, *203*(3), 159-165.

Madi, M. S., Khayati, K., and Bigras, P. (2004, October). Parameter estimation for the LuGre friction model using interval analysis and set inversion. In*Systems, Man and Cybernetics, 2004 IEEE International Conference on* (Vol. 1, pp. 428-433). IEEE.

Messina, A., Giannoccaro, N. I., and Gentile, A. (2005). Experimenting and modelling the dynamics of pneumatic actuators controlled by the pulse width modulation (PWM) technique, *Mechatronics*, 15 (7), 859-81.

Mehmood, A., Laghrouche, S., & El Bagdouri, M. (2011). Modeling identification and simulation of pneumatic actuator for vgt system. *Sensors and Actuators A: Physical*, *165*(2), 367-378.

Moreau, R., Pham, M. T., Tavakoli, M., Le, M. Q., and Redarce, T. (2012). Sliding-mode bilateral teleoperation control design for master–slave pneumatic servo systems. *Control Engineering Practice*, *20*(6), 584-597.

Nguyen, T., Leavitt, J., Jabbari, F., and Bobrow, J. E. (2007). Accurate sliding-mode control of pneumatic systems using low-cost solenoid valves. *Mechatronics, IEEE/ASME Transactions on*, *12*(2), 216-219.

Ning, S. and Bone, G. M. (2002). High steady-state accuracy pneumatic servo positioning system with PVA/PV control and friction compensation, *2002 IEEE International Conference on Robotics and Automation (ICRA)*, Vols I-IV Proceedings, 2824-29.

--- (2005). Experimental comparison of two pneumatic servo position control algorithms, *2005 IEEE International Conference on Mechatronics and Automations, Vols 1-4, Conference Proceedings*, 37-42.

Noritsugu, T. (1987). Development of PWM mode electro-pneumatic servomechanism, PartII: Position control of a pneumatic cylinder. J. of Fluid Control, 67:7-28.

Paul, A. K., Mishra, J. K. and Radke, M. G. (1994). Reduced order sliding mode control for pneumatic actuator. *Control Systems Technology, IEEE Transactions on*, *2*(3), 271-276.

Rao, Z. and Bone, G. M. (2008). Nonlinear modeling and control of servo pneumatic actuators, *IEEE Transactions on Control Systems Technology*, 16 (3), 562-69.

Richard, E., and Scavarda, S. (1996). Comparison between linear and nonlinear control of an electropneumatic servodrive. *Journal of Dynamic Systems, Measurement, and Control*, *118*(2), 245-252.

Schroeder, L. E., Singh, R. (1993). Experimental study of friction in a pneumatic actuator at constant velocity. *Trans ASME Journal of Dynamic Systems, Measurement, and Control*, 115(9): 575–577

Shearer, J. L. (1956). Study of pneumatic processes in the continuous control of motion with compressed Air - i,ii, *Transactions of ASME*, 233-42.

Shen, X., Zhang, J., Barth, E. J., and Goldfarb, M. (2006). Nonlinear model-based control of pulse width modulated pneumatic servo systems, *Journal of Dynamic Systems Measurement and Control-Transactions of the ASME*, 128 (3), 663-69.

Shih, M. C. and Ma, M. A. (1998). Position control of a pneumatic cylinder using fuzzy PWM control method. *Mechatronics*, *8*(3), 241-253.

Smaoui, M., Brun, X., and Thomasset, D. (2006). A study on tracking position control of an electropneumatic system using backstepping design, *Control Engineering Practice,* 14 (8), 923-33.

Utkin, V. (1993). Sliding mode control design principles and applications to electric drives. *Industrial Electronics, IEEE Transactions on*, *40*(1), 23-36.

van Varseveld, R. B. and Bone, G. M. (1997). Accurate position control of a pneumatic actuator using on/off solenoid valves, *IEEE-ASME Transactions on Mechatronics,* 2 (3), 195-204.

Verlet, L. (1967). Computer "experiments" on classical fluids. I. Thermodynamical properties of Lennard-Jones molecules. *Physical review*,*159*(1), 98.

Wang, H., Mo, J. P., and Chen, N. (1998). On the estimation of on-off valve parameters for control of programmable pneumatic actuators, *Transactions of the Institute of Measurement and Control,* 20 (5), 211-20.

Wang, J., Wang, D. J. D., Moore, P. R., and Pu, J. (2001). Modelling study, analysis and robust servocontrol of pneumatic cylinder actuator systems. *IEE Proceedings-Control Theory and Applications*, *148*(1), 35-42.

Ye, N., Scavarda, S., Betemps, M. and Jutard, A. (1992). Models of a pneumatic PWM solenoid valve for engineering applications. *Journal of Dynamic Systems, Measurement, and Control*, *114*(4), 680-88.